Search for Charged Higgs Bosons and Supersymmetric Particles

Search for Charged Higgs Bosons and Supersymmetric Particles

Ph.D. thesis

Gabriella Pásztor

Supervisor: Dezső Horváth

Eötvös University
Budapest, 1999

To my grandparents

Abstract

In this work searches for charged Higgs bosons and supersymmetric particles in electron-positron collisions are described using data collected by the OPAL experiment at the LEP collider at CERN.

Charged Higgs bosons are predicted by various extensions of the Standard Model (SM). The searches for pair-produced charged Higgs bosons are performed in the qqqq and qq$\tau\nu_\tau$ final states at centre-of-mass energies $\sqrt{s} = 130 - 189$ GeV. None of them reveal any significant excess of events over the SM expectations. Upper limits on the production cross-sections are derived. In combination with the analysis of the $\tau\nu_\tau\tau\nu_\tau$ final state, assuming BR($H^\pm \to \tau\nu_\tau$)+BR($H^\pm \to$qq)=1 for the branching ratios, charged Higgs bosons are excluded up to a mass of 68.7 GeV at the 95% confidence level, independent of BR($H^\pm \to \tau\nu_\tau$).

Motivated by an excess of four-jet events with a dijet invariant mass sum around 105 GeV reported by the ALEPH Collaboration at LEP in their $\sqrt{s} = 130 - 136$ GeV data collected in 1995, a search for pair-produced heavy scalar objects is performed in the four-jet final state at $\sqrt{s} = 130 - 184$ GeV. No sign of anomalous four-jet production is found, and upper limits on the production cross-section as a function of the dijet mass sum are derived for dijet mass differences below 30 GeV.

Supersymmetric extensions provide convenient solutions to several unanswered problems of the SM. They predict, however, a large number of new particles, none of which have been observed so far. Searches for pair-produced charginos, neutralinos and scalar fermions with R-parity violating decays are performed at $\sqrt{s} = 183$ GeV. An important consequence of R-parity violation is that the lightest supersymmetric particle (LSP) is unstable. In this study the LSP is assumed to decay promptly through one dominant R-parity violating decay mode. Final states consisting of four jets with or without significant missing energy are studied. No excess of such events over the SM expectation is observed, allowing the derivation of upper limits on the production cross-section. Mass limits in the framework of the Minimal Supersymmetric Standard Model (MSSM) are also placed. In combination with searches in other final states, our results constrain the allowed parameter space of the MSSM.

Preface

Despite the great success of the Standard Model of particle physics in describing all confirmed experimental data, there are theoretical arguments which ask for a more fundamental theory. One of the strongest proofs of physics beyond the Standard Model would be the discovery of non-Standard Model particles. The LEP collider with its clean experimental environment, high energy and luminosity provides an excellent opportunity for physicist to explore the unknown. In this work we study possible manifestations of new physics, the existence of charged Higgs bosons and supersymmetric particles using the data collected by the OPAL Collaboration at LEP.

Chapter 1 gives an outline of the theoretical framework of this study, reviews the virtues and drawbacks of the Standard Model and shows a possible solution to its problems: supersymmetry. Chapter 2 provides a short introduction to the LEP Collider and a description of the OPAL detector, the experimental apparatus used in this work. Chapter 3 overviews the main physics processes occurring in electron-positron interactions and their Monte Carlo simulation, lists and explains the common features and tools of the analyses presented here. The original subject of my Ph.D. research, the search for charged Higgs bosons in the framework of models with two Higgs field doublets is described in Chapter 4. The observation of anomalous four-jet production by the ALEPH Collaboration in 1995 initiated a LEP-wide effort to confirm or exclude this phenomenon. My contribution to this work is summarized in Chapter 5. This observation also spurred theoretical speculations, and supersymmetric models with R-parity violation came into view. Chapter 6 presents a search for pair-produced supersymmetric particles decaying via R-parity violating interactions.

This work would never have come to reality without the help and support of many people.

I would like to thank Dezső Horváth, my supervisor, who was always willing to transmit his invaluable experience to me, and Péter Igó-Kemenes, who introduced me to the experimental data analysis, to the lively and friendly community of the OPAL Collaboration and to the interesting field of new particle searches.

György Vesztergombi oriented my attention in the first place toward the work carried out at CERN and at the KFKI Research Institute for Particle and Nuclear Physics in Budapest, made it possible for me to join this unique scientific community and helped me in many ways. I am also grateful to József Zimányi, David E. Plane and Rolf D. Heuer for their invaluable support.

I can not mention individually here all the people from the OPAL Collaboration who have helped me during my work in one way or in another. During the years I have learned a lot from many of them. I am especially grateful to my present and past immediate colleagues Sylvie Braibant, Klaus Desch, Ivor Fleck, Susan M. Gascon-Shotkin, Paolo Giacomelli, Csaba Hajdu, Ulrich Jost and Satoru Yamashita.

Ákos Csilling and Dezső Horváth have carefully read the preliminary versions of this study and through their comments and suggestions contributed significantly to its improvement.

This work was supported by the Hungarian Scientific Research Fund (OTKA) under the contract numbers F015089, F023259, T016660 and T023793. The Hungarian Fellowship Committee has provided me a six-month Eötvös Fellowship of the Republic of Hungary and together with the Swiss National Science Fund another six-month grant to work on this subject at CERN.

Very special thanks go to my friends and family for their unfailing love, constant support, encouragement and tolerance. I would like to express my love and thank to my husband, Ákos Csilling, for all the years together, for being my colleague, companion, friend and lover.

Thank you!

Contents

List of Figures

List of Tables

Chapter 1

Theoretical Overview

The Standard Model (SM) [1] of strong and electroweak interactions is in agreement with all confirmed experimental data. The only ingredient of the SM that has not been observed so far is the Higgs boson [2], whose search is ongoing at LEP (CERN) and Tevatron (Fermilab) and, if no evidence is found, will continue at LHC (CERN).

However, there are reasons to believe that the SM is not the last chapter in the theory of particle physics. To go beyond the SM we should first have a critical look at it, trying to identify its virtues and open questions [3]. A successful extension of the SM has to answer the latter and should not spoil the former.

1.1 The Standard Model

The Standard Model is an $SU(3)_C \times SU(2)_L \times U(1)_Y$ gauge theory, where the indices stand for colour, left and Y hypercharge. Gauge invariance determines its spin-1 particle content: the gluons $G^A_\mu (A = 1, ..., 8)$, associated with the strong interaction and characterized by the coupling constant g_s; and the bosons $W^I_\mu (I = 1, 2, 3)$ and B_μ, mediating the electroweak interactions with coupling constants g and g', respectively.

The Yang-Mills part of the Lagrangian is also fixed by gauge invariance:

$$\mathcal{L}_{YM} = -\frac{1}{4} G^{\mu\nu\,A} G^A_{\mu\nu} - \frac{1}{4} W^{\mu\nu\,I} W^I_{\mu\nu} - \frac{1}{4} B^{\mu\nu} B_{\mu\nu} \tag{1.1}$$

with

$$G^A_{\mu\nu} = \partial_\mu G^A_\nu - \partial_\nu G^A_\mu + g_s f_{ABC} G^B_\mu G^C_\nu, \tag{1.2}$$

$$W^I_{\mu\nu} = \partial_\mu W^I_\nu - \partial_\nu W^I_\mu + g f_{IJK} W^J_\mu W^K_\nu, \tag{1.3}$$

$$B_{\mu\nu} = \partial_\mu B_\nu - \partial_\nu B_\mu, \tag{1.4}$$

where f_{ABC} and f_{IJK} are the fully antisymmetric $SU(3)$ and $SU(2)$ structure constants, respectively.

The spin-$\frac{1}{2}$ particle content of the SM consists of three generations of quarks and leptons, with transformation properties under $SU(3)_C \times SU(2)_L \times U(1)_Y$ summarized below:

$$\begin{gathered} q_{aL} \equiv \begin{pmatrix} u_{aL} \\ d_{aL} \end{pmatrix} \sim \left(3, 2, +\tfrac{1}{6}\right), \qquad \ell_{aL} \equiv \begin{pmatrix} \nu_{aL} \\ e_{aL} \end{pmatrix} \sim \left(1, 2, -\tfrac{1}{2}\right), \\ u_{aR} \sim \left(3, 1, +\tfrac{2}{3}\right), \qquad d_{aR} \sim \left(3, 1, -\tfrac{1}{3}\right), \qquad e_{aR} \sim (1, 1, -1). \end{gathered} \tag{1.5}$$

Here $a = 1, 2, 3$ is the generation index and the weak hypercharge Y is defined according to $Q = T_{3L} + Y$, where Q is the electric charge and T_{3L} is the third component of the weak isospin. Left- and right-handed chiral projections, defined by $P_{L/R} = \frac{1}{2}(1 \pm \gamma^5)$, are used and the $SU(3)_C$ and $SU(2)_L$ indices have been left implicit. Notice that no right-handed neutrino, ν_{aR}, is introduced. Given the quantum number assignments of Equation 1.5, gauge invariance determines the interactions between fermions and gauge bosons:

$$\mathcal{L}_F = i\bar{\Psi}\gamma^\mu D_\mu \Psi \tag{1.6}$$

with

$$D_\mu = \partial_\mu - i g_s G^A_\mu \lambda^A - i g W^I_\mu \frac{\tau^I}{2} - i g' B_\mu Y. \tag{1.7}$$

All the fermions are denoted by the symbol $\Psi \equiv (q_L, u_R, d_R, \ell_L, e_R)_{a=1,2,3}$ and λ^A, $\frac{1}{2}\tau^I$ and Y stand for the hermitian generators of the $SU(3)_C$, $SU(2)_L$ and $U(1)_Y$ gauge groups in the representation defined by Equation 1.5.

One of the most important properties of the SM is the chirality of its fermion content. Left- and right-handed fermions have different quantum numbers with respect to $SU(2)_L \times$

$U(1)_Y$. In particular, $SU(2)_L \times U(1)_Y$ gauge invariance forbids explicit mass terms of the form $m_f \bar{f}_L f_R + h.c.$

The last component of the SM is a complex spin-0 $SU(2)$ doublet, the Higgs field:

$$\phi \equiv \begin{pmatrix} \varphi^+ \\ \varphi^0 \end{pmatrix} \sim \left(1, 2, +\frac{1}{2}\right), \tag{1.8}$$

which appears not only in the part of the Lagrangian containing the gauge interactions and self-interactions of the spin-0 field:

$$\mathcal{L}_S = (D_\mu \phi)^\dagger (D^\mu \phi) - V, \tag{1.9}$$

with the scalar potential

$$V = \mu^2 \phi^\dagger \phi + \lambda (\phi^\dagger \phi)^2, \tag{1.10}$$

but also in the part containing the Yukawa couplings:

$$\mathcal{L}_{Yuk} = h^U_{ab} \bar{q}_{aL} u_{bR} \tilde{\phi} + h^D_{ab} \bar{q}_{aL} d_{bR} \phi + h^E_{ab} \bar{\ell}_{aL} e_{bR} \phi + h.c. \tag{1.11}$$

with

$$\tilde{\phi} = (i\sigma^2 \phi^*) = (\varphi^{0*} \quad -\varphi^-)^T \sim (1, 2, -\frac{1}{2}). \tag{1.12}$$

Here h^U, h^D and h^E are arbitrary 3×3 complex matrices in generation space corresponding to up- and down-type quarks and charged leptons, respectively.

The last two parts of the Lagrangian, $\mathcal{L}_S$ and $\mathcal{L}_{Yuk}$, are instrumental to describe two crucial physical phenomena: the spontaneous breaking of the local gauge symmetry $SU(2)_L \times U(1)_Y$ down to $U(1)_Q$, with the associated mass generation for the physical $W^\pm$ and Z^0 bosons, and the explicit breaking of the global flavour symmetry.

1.1.1 The Higgs Mechanism and the ρ Parameter

Elementary particles in the SM acquire mass through the Higgs mechanism [4], by means of spontaneous symmetry breaking.

Choosing $\lambda > 0$ and $\mu^2 < 0$ in Equation 1.10, the classical potential has its minimum at

$$\langle \phi \rangle = \frac{1}{\sqrt{2}} \begin{pmatrix} 0 \\ v \end{pmatrix} \tag{1.13}$$

with

$$v = \sqrt{\frac{-\mu^2}{\lambda}} \tag{1.14}$$

It is appropriate to expand ϕ around its minimum value to obtain the physical fields of the theory:

$$\phi \rightarrow \begin{pmatrix} 0 \\ \frac{v+h(x)}{\sqrt{2}} \end{pmatrix}, \tag{1.15}$$

where $h(x)$ is a real field. Substituting it into $\mathcal{L}_S$ one can find that non-vanishing masses are generated for the Z^0 and $\mathrm{W}^{\pm}$ bosons,

$$m^2_{\mathrm{Z}^0} = \frac{(g^2 + g'^2)v^2}{4}, \quad m^2_{\mathrm{W}^{\pm}} = \frac{g^2 v^2}{4}, \tag{1.16}$$

while the photon, γ, remains massless, as required by the residual gauge invariance with respect to $U(1)_Q$. The physical fields corresponding to the photon, the Z^0 and $\mathrm{W}^{\pm}$ bosons are given by linear combinations of W^I_μ and B_μ:

$$A_\mu = \sin\theta_W W^3_\mu + \cos\theta_W B_\mu, \tag{1.17}$$

$$Z_\mu = \cos\theta_W W^3_\mu - \sin\theta_W B_\mu, \tag{1.18}$$

$$W^{\pm}_\mu = \frac{W^1_\mu \pm i W^2_\mu}{\sqrt{2}}, \tag{1.19}$$

where the tangent of the Weinberg angle is

$$\tan\theta_W = \frac{g'}{g}. \tag{1.20}$$

A very important property of the SM, before the inclusion of quantum corrections, can be derived from Equation 1.16 and 1.20:

$$\rho \equiv \frac{m^2_{\mathrm{W}^{\pm}}}{m^2_{\mathrm{Z}^0}\cos^2\theta_W} = 1. \tag{1.21}$$

For the discussion of possible extensions of the SM, it is interesting to note that Equation 1.21 can be understood in general terms as a consequence of the custodial symmetry [5].

1.1.2 Flavour Symmetry Breaking

Flavour symmetry implies that the gauge interactions do not distinguish among the three generations of quarks and leptons. In the real world this symmetry must be broken, since a complicated pattern of masses, mixing angles and phases of the SM fermions is observed.

Without $\mathcal{L}_{Yuk}$, the SM has a $[U(3)]^5$ global symmetry, corresponding to the unitary transformations in generation space for the five irreducible fermionic representations of the gauge group. Since the $U(1)_Y$ subgroup is gauged, the additional symmetry is $[SU(3)]^5 \times [U(1)]^4$, where the $U(1)$ factors correspond to the total baryon number B and the individual lepton numbers (L_e, L_μ, L_τ). The role of $\mathcal{L}_{Yuk}$ is precisely the explicit breaking of the flavour symmetry down to $[U(1)]^4$, corresponding to the accidental global symmetries of the SM (B, L_e, L_μ, L_τ), in agreement with the experimental bounds on the baryon- and lepton-number non-conserving processes.

The explicit breaking of the flavour symmetry is realized in a special way. The breaking is strong, as one can see from the observed pattern of the nine fermion masses, three mixing angles and the CP-violating phase appearing in the Cabbibo-Kobayashi-Maskawa (CKM) matrix. However, the only source of flavour violation in the SM Lagrangian is the CKM matrix, controlling the weak charged current interactions. In the SM, all the tree level flavour changing neutral current (FCNC) couplings are flavour diagonal. FCNC processes are induced only by loop effects, controlled by the CKM matrix, and suppressed enough to guarantee agreement with experimental data on flavour physics.

1.1.3 Anomaly Cancellation and Charge Quantization

The quantum consistency of chiral gauge theories is endangered by the existence of anomalies [6]. A classical symmetry is considered to be anomalous when it is not conserved by the quantum corrections. If a gauge symmetry is anomalous, this spoils gauge invariance and/or renormalizability. It is remarkable that in the SM, with the quantum number assignment of Equation 1.5, there is an automatic cancellation of all possible gauge anomalies.

It is impossible to understand within the SM why the electric charge of the different

quarks and leptons is related by simple fractional coefficients. On the other hand, it can be shown that asking for the cancellation of gauge anomalies goes a long way toward implying the charge assignments of the SM.

1.1.4 The Standard Model as an Effective Theory

Despite the remarkable achievements described in the previous sections, the SM most likely can not be the ultimate theory of particle physics. Among other things, it has around twenty arbitrary parameters, which may seem too many for a fundamental theory, and it leaves several unanswered questions, like the ones concerning unification and flavour. The unification problem is related to the gauge interactions, whose pattern of groups and representations is complicated and arbitrary. The flavour problem is connected to the Yukawa interactions: there is no explanation for the existence of three generations of quarks and leptons, nor for the measured fermion masses, mixing angles and phases.

Moreover, it is quite obvious that the SM must be extended. The two strongest arguments to support this statement are the facts that the SM does not include the description of the gravitational interaction, and some of the SM couplings are not assimptotically free, making it almost surely inconsistent as a formal quantum field theory.

The latter brings along an important implication: the SM should be regarded as an effective theory, valid up to some physical cut-off scale Λ. The question naturally emerges: where this cut-off scale, at which the SM must be replaced by a more fundamental theory, is. Two extreme but plausible answers can be given:

(i) Λ is not much below the reduced Planck scale[1], $M_P = (8\pi G_N)^{-0.5} \approx 2.4 \times 10^{18}$ GeV, as roughly suggested by the measured strength of the fundamental interactions, including gravitation.

(ii) Λ is not much above the Fermi scale[2], $(G_F)^{-0.5} \approx 300$ GeV, as suggested by the idea that new physics must be associated with the electroweak symmetry breaking.

[1] In the definition of the Planck scale G_N is the gravitational constant.

[2] In the definition of the Fermi scale G_F is the Fermi coupling constant.

The first choice is not very popular, since it would require fine-tuning, a conspiracy between low-energy (below the cut-off scale) and high-energy (above the cut-off scale) physics in order to give a strongly suppressed coefficient of order G_F^{-1}/Λ^2 to the quadratically divergent scalar mass operator [7]. Such a possibility can also be tested experimentally in the future via the search for the Higgs boson. Figure 1.1 shows the region in the plane of the top quark and Higgs boson masses allowed for various choices of Λ by the following two requirements [8]:

- The SM effective potential should not develop, besides the minimum corresponding to the experimental value of the electroweak scale, other minima with lower energy and much larger value of the Higgs field. This assumption is usually called as vacuum stability and gives a lower bound on the Higgs boson mass m_{H^0}.
- The SM effective self-coupling should not develop a Landau pole at scales smaller than Λ. This constraint is usually called as triviality and assures that the theory remains perturbative to a given scale Λ. For a given top mass m_{t} this sets an upper bound on m_{H^0}.

Figure 1.1 [9] indicates that the choice of very large cut-off scales can be invalidated by LEP, Tevatron or LHC in two possible ways: either by discovering a SM-like Higgs boson lighter than 130 GeV, or excluding it in the mass range of $130 - 200$ GeV.

Answer (ii) instead gives rise to a well-known conceptual bifurcation:

(a) The elementary Higgs scalar is replaced by some fermion condensate, induced by a new strong interaction near the Fermi scale. This includes both old and new variants of the technicolor models.

(b) The SM is embedded in a model with broken supersymmetry and the supersymmetry breaking mass splitting between the SM particles and their superpartners are of the order of the electroweak scale. This approach will be discussed in the next section.

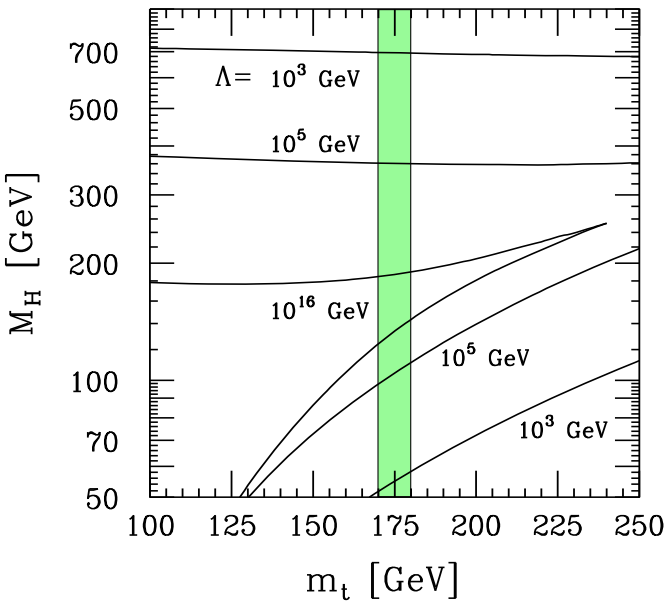

Figure 1.1: *Bounds in the* $[m_{\mathrm{t}}, m_{\mathrm{H}^0}]$ *plane for various choices of the cut-off parameter* Λ *in the SM. The range corresponding to the top quark mass measurements [10] is indicated.*

1.2 Low Energy Supersymmetry

Supersymmetry (SUSY) [11] is a hypothetical symmetry of the basic laws of Nature, a generalization of the space-time symmetries of quantum field theory that transforms fermions into bosons and vice versa. At present, there are no unambiguous experimental results that require the existence of SUSY. However, supersymmetric theories could be successful extensions of the SM, providing a good description of the experimental data and at the same time answering the open questions of the SM.

One of the main motivations for low energy SUSY, where the breaking of the effective scale of SUSY is tied to the electroweak scale, is the hierarchy or naturalness problem of the SM, as already mentioned briefly. The tree level potential of the SM is characterized by a mass parameter μ^2 and by a dimensionless quartic coupling λ. The ratio μ^2/λ is fixed by the measured Fermi coupling constant, defining the scale of the electroweak symmetry breaking. However, the squared mass of the physical Higgs particle $m^2_{\mathrm{H}^0}$, proportional to

μ^2 (or $\lambda\mu^2$), is a free parameter of the SM. Arguments based on perturbative unitarity and triviality suggest that self-consistency of the SM is broken unless $m_{\mathrm{H}^0} < \mathcal{O}(1\ \mathrm{TeV})$. This is hard to fulfill in the effective field theory taking the fact that already at the one-loop level there are quadratically divergent contributions to the Higgs boson mass.

As an example, consider a model with a complex spin-0 field of mass m_B and a two-component fermion of mass m_F, with Yukawa coupling λ_F and quartic scalar coupling λ_B. Then the one-loop correction to the boson mass involves a term:

$$\delta m_B^2 \propto (\lambda_B - \lambda_F^2)\Lambda^2, \tag{1.22}$$

where Λ is the ultraviolet cut-off. Note, that the minus sign comes from the fermion loop and that other less divergent terms are also present.

To make the boson mass naturally small we need a symmetry relating bosons and fermions, forcing the coefficient of Λ^2 to vanish. The only candidate for this is SUSY, not only at one-loop but also at higher orders.

At this point, we should also recall another theoretical motivation for SUSY: it is the most general symmetry of the S-matrix consistent with non-trivial relativistic quantum field theory. At its birth it was not invented to solve any puzzle or explain any observation, but slowly it was realized that it has the potential to solve an astonishing number of major physical problems.

Supersymmetric field theories are based on the SUSY algebra, an extension of the Poincaré algebra obtained from the latter by adding some generators of fermionic character obeying anticommutation relations. Without going into details of the formulation and the construction of supersymmetric theories we refer to some of the many excellent reviews [12] and limit ourselves to the case of simple N=1 SUSY in $d = 4$ space-time dimensions, on which the Minimal Supersymmetric extension of the the Standard Model (MSSM) [13, 14] is based.

The fundamental anticommutation relation of the $N = 1$ SUSY algebra is

$$\{Q_\alpha, Q_\beta\} = -2(\gamma^\mu C)_{\alpha\beta} P_\mu, \tag{1.23}$$

where C is the charge conjugation matrix, Q is a Majorana spinor, commutating both with the generators of P_μ of space-time translations and T^a of possible internal symmetries. This implies that particles sitting in the same irreducible representation of SUSY have spins differing by $\frac{1}{2}$, but the same quantum numbers and, as long as SUSY is unbroken, the same mass.

It is convenient to start from the irreducible representation of SUSY when building the Lagrangian. Let us recall that two types of supermultiplets, chiral and vector supermultiplets, are used in the construction of globally supersymmetric extensions of the SM. Chiral supermultiplets contain a complex spin-0 field φ, a Majorana spinor ψ, carrying the same degrees of freedom as a left-handed Weyl spinor ψ_L, and a complex scalar F, corresponding to an auxiliary non-propagating field. Vector superfields, in the Wess-Zumino gauge, contain a real spin-1 field V_μ, a Majorana spinor λ and a real auxiliary field D.

In the case of a simple gauge group G with hermitian generators T^a and a gauge coupling constant g, with the above superfields, the Lagrangian has the form:

$$\mathcal{L}_{SUSY} = -\frac{1}{4}F^{\mu\nu\,a}F^a_{\mu\nu} + \frac{i}{2}\overline{\lambda}^a\gamma^\mu D_\mu\lambda^a + (D_\mu\phi)^\dagger_i(D^\mu\phi)^i + \frac{i}{2}\overline{\psi}_i\gamma^\mu D_\mu\psi^i + \left[i\sqrt{2}g\overline{\psi}_i\lambda^a(T^a\varphi)^i + h.c.\right] - \frac{1}{2}\left[\frac{\partial^2 w}{\partial\varphi^i\partial\varphi^j}\overline{\psi^c}^i\psi^j + h.c.\right] - V(\varphi,\varphi^\dagger), \tag{1.24}$$

where $F^a_{\mu\nu}$ is the usual Yang-Mills field strength and D_μ is the covariant derivative. The c superscript stands for charge conjugation. The scalar potential reads

$$V = F^*_i F^i + \frac{g^2}{2}D^a D^a = \sum_i \left|\frac{\partial w}{\partial\varphi^i}\right|^2 + \sum_a \frac{g^2}{2}\left[\varphi^*_i(T^a)^i_j\varphi^j\right]^2, \tag{1.25}$$

where the superpotential $w(\phi)$ is a gauge invariant polynomial of degree three in the fields φ^i.

SUSY brings along a unification of couplings. In ordinary theories, like the SM, one may introduce three different types of couplings: gauge, Yukawa and quartic scalar couplings. Supersymmetric theories, however, allow only two types: gauge and superpotential couplings, and the dimensionless couplings appearing in the scalar potential are related to these.

1.2.1 Minimal Supersymmetric Extension of the Standard Model

MSSM is a theory in $d = 4$ space-time dimensions described by the minimal renormalizable Lagrangian with a global $N = 1$ SUSY that extends the SM Lagrangian.

Keeping $SU(3)_C \times SU(2)_L \times U(1)_Y$ as the gauge group of the theory, the spin-1 fields of the SM are replaced by vector superfields. The theory contains new spin-$\frac{1}{2}$ particles, called gauginos: the $SU(3)$ gluinos $\tilde{g}$, the SU(2) winos $\tilde{W}$ and the $U(1)$ bino $\tilde{B}$.

Similarly, the spin-$\frac{1}{2}$ matter fields of the SM are replaced by corresponding chiral superfields, including a new complex spin-0 field for each quark and lepton chirality state: the squarks $\tilde{q}_L \equiv (\tilde{u}_L \tilde{d}_L)^T, \tilde{u}_R, \tilde{d}_R$ and the sleptons $\tilde{\ell}_L \equiv (\tilde{\nu}_L \tilde{e}_L)^T, \tilde{e}_R$ in three generations as their superpartners. Since chiral superfields contain left-handed spinors, we shall introduce for each generation the superfields Q, L, U^c, D^c and E^c, whose fermionic components are $q_L, \ell_L, (u^c)_L, (d^c)_L$ and $(e^c)_L$, respectively.

Finally, we have to introduce additional multiplets containing the spin-0 degrees of freedom necessary for the Higgs mechanism. To give masses to all quarks and leptons, to cancel gauge anomalies and to avoid a massless fermion of charge ± 1, we must introduce at least two Higgs doublet chiral supermultiplets

$$H_1 \equiv \begin{pmatrix} H_1^0 \\ H_1^- \end{pmatrix} \sim \left(1, 2, -\frac{1}{2}\right), \quad H_2 \equiv \begin{pmatrix} H_2^+ \\ H_2^0 \end{pmatrix} \sim \left(1, 2, +\frac{1}{2}\right). \tag{1.26}$$

They contain, in addition to the spin-0 fields (H_1^0, H_1^-) and (H_2^+, H_2^0) denoted with the same symbols as the corresponding supermultiplets, also the associated superfields $(\tilde{H}_1^0, \tilde{H}_1^-)$ and $(\tilde{H}_2^+, \tilde{H}_2^0)$, the higgsinos.

With these chiral superfields introduced, the most general gauge invariant and renormalizable superpotential is

$$\begin{aligned} w &= h^U Q U^c H_2 + h^D Q D^c H_1 + h^E L E^c H_1 + \mu H_1 H_2 \\ &+ \lambda Q D^c L + \lambda' L L E^c + \mu' L H_2 \\ &+ \lambda'' U^c D^c D^c. \end{aligned} \tag{1.27}$$

Here, the generation indices are understood, but we should keep in mind that the couplings

$\mu', (h^U, h^D, h^E)$ and $(\lambda, \lambda', \lambda'')$ are tensors with one, two and three generation indices, respectively. The first line contains only terms which respect total baryon and lepton number conservation, while the terms in the second line violate lepton number conservation and the term in the third line violates baryon number conservation. The existence of such terms may cause phenomenological problems. The most obvious constraint comes from the non-observation of proton decay, since the simultaneous presence of terms with $\lambda^{'}$ coupling in the second and $\lambda^{''}$ coupling in the third line would lead to superfast proton decay mediated by the exchange of a squark.

The usual, somewhat ad-hoc solution for this phenomenological embarrassment is the assumption of a discrete, multiplicative symmetry called R-parity [15], defined as

$$R_p = (-1)^{2S+3B+L}, \tag{1.28}$$

where S, B and L are the spin, the baryon and lepton numbers of the particle, respectively. R-parity discriminates between SM particles and their superpartners, giving $R_p = +1$ for the ordinary particles (quarks, leptons, gauge and Higgs bosons) and $R_p = -1$ for their supersymmetric partners (squarks, sleptons, gauginos and higgsinos).

The choice of the gauge group and the chiral superfield content is enough to specify the form of the globally supersymmetric Lagrangian $\mathcal{L}_{SUSY}$ which extends the SM one. However, we know that SUSY is broken in Nature, since we do not observe supersymmetric partners of the SM particles with the same mass. This non-observation leads to the problem of SUSY breaking. To parametrize the phenomenology at the electroweak scale, a collection of explicit but soft SUSY breaking terms, $\mathcal{L}_{SOFT}$, are added to $\mathcal{L}_{SUSY}$. In general, $\mathcal{L}_{SOFT}$ contains mass terms of scalar fields and gauginos and a restricted set of scalar interaction terms proportional to the corresponding superpotential couplings:

$$\begin{aligned} \mathcal{L}_{SOFT} &= -\sum_i \tilde{m}_i^2 |\phi^i| - \frac{1}{2}\sum_A M_A \bar{\lambda}^A \lambda^A \\ &- (h^U A^U Q U^c H_2 + h^D A^D Q D^c H_1 + h^E A^E L E^c H_1 \\ &\quad + m_3^2 H_1 H_2 + h.c.). \end{aligned} \tag{1.29}$$

Here ϕ^i $(i = H_1, H_2, Q, U^c, D^c, L, E^c)$ denotes the generic spin-0 field with soft SUSY

breaking scalar mass $\tilde{m}_i$, and λ^A $(A = 1, 2, 3)$ is the generic gaugino field with soft SUSY breaking gaugino mass M_A. (A^U, A^D, A^E) stand for the soft SUSY breaking scalar couplings and are matrices in the generation space. m_3^2 describes the soft SUSY breaking Higgs mixing. In the above expression the mass mixing between the three generations has been neglected. Notice, that the general form of $\mathcal{L}_{SOFT}$ introduces a huge number of free parameters.

1.2.2 The MSSM Particle Spectrum

The tree level scalar potential associated with the MSSM Lagrangian

$$\mathcal{L}_{MSSM} = \mathcal{L}_{SUSY} + \mathcal{L}_{SOFT} \tag{1.30}$$

is a function of all the spin-0 fields of the model. In the discussion of the electroweak symmetry breaking it is usually assumed that all squark and slepton fields have vanishing vacuum expectation value. Then we can restrict our attention to the Higgs potential, which is minimized for

$$\langle H_1 \rangle = \begin{pmatrix} v_1 \\ 0 \end{pmatrix} \quad \text{and} \quad \langle H_2 \rangle = \begin{pmatrix} 0 \\ v_2 \end{pmatrix}, \tag{1.31}$$

where v_1 and v_2 are real after redefining the phases of the Higgs superfields.

It is convenient to introduce the variables

$$v^2 \equiv v_1^2 + v_2^2, \quad \tan\beta \equiv \frac{v_2}{v_1} \tag{1.32}$$

to describe the mass spectrum of the MSSM.

The $R_p = +1$ sector of the MSSM contains all the spin-1 and spin-$\frac{1}{2}$ particles of the SM. The only difference from the SM is that the mass terms for gauge bosons and fermions originate from two independent vacuum expectation values. The tree-level expressions for the Z^0 and $\mathrm{W}^\pm$ masses are

$$m_{\mathrm{Z}^0}^2 = \frac{(g^2 + g'^2)v^2}{2}, \quad m_{\mathrm{W}^\pm}^2 = \frac{g^2 v^2}{2}. \tag{1.33}$$

Neglecting the mixing between the fermion generations we get for example for the first generation

$$m_{\mathrm{u}}^2 = h_{\mathrm{u}}^2 v_2, \quad m_{\mathrm{d}}^2 = h_{\mathrm{d}}^2 v_1, \quad m_{\mathrm{e}}^2 = h_{\mathrm{e}}^2 v_1, \tag{1.34}$$

where $(h_{\rm u}, h_{\rm d}, h_{\rm e})$ are dimensionless Yukawa couplings. Note that the tree-level masses of down-type quarks and charged leptons are proportional to v_1 and the masses of up-type quarks are proportional to v_2.

Non-trivial structure arises in the Higgs sector, where we have two complex doublets amounting to eight degrees of freedom. After decoupling the three Goldstone bosons, we are left with five physical degrees of freedom. Two of them correspond to a charged (complex) field H^+ ($\mathrm{H}^- = (\mathrm{H}^+)^*$) with mass $m_{\mathrm{H}^\pm}$. The remaining degrees of freedom give three neutral states. One of them, A^0, is CP-odd with mass m_{A^0}. The other two are CP-even and the corresponding mass eigenstates, h^0 and H^0 in order of increasing mass $m_{\mathrm{h}^0} < m_{\mathrm{H}^0}$, are obtained by diagonalizing their mass matrix. The mixing angle in the CP-even neutral Higgs sector is conventionally described by the angle $-\frac{\pi}{2} \leq \alpha \leq 0$.

It is important to note the tree level mass relations:

$$m^2_{\mathrm{H}^\pm} = m^2_{\mathrm{W}^\pm} + m^2_{\mathrm{A}^0}, \tag{1.35}$$

$$m^2_{\mathrm{h}^0} + m^2_{\mathrm{H}^0} = m^2_{\mathrm{Z}^0} + m^2_{\mathrm{A}^0}, \tag{1.36}$$

and the fact that at tree level all Higgs boson masses and couplings can be expressed in terms of two parameters only, usually chosen to be $(m_{\mathrm{A}^0}, \tan\beta)$, $(m_{\mathrm{h}^0}, \tan\beta)$ or $(m_{\mathrm{A}^0}, m_{\mathrm{h}^0})$.

However, one should keep in mind that the radiative corrections [16] modify these relations considerably and that they depend on the top quark mass and the parameters of the soft SUSY breaking Lagrangian.

The $R_p = -1$ sector of the MSSM contains the superpartners of the ordinary quarks and leptons. Even if we neglect the mixing between the three generations, there is another kind of mixing that has to be considered. Except for the sneutrinos, the spin-0 partners of the left- and right-handed quarks and leptons can in general mix. Therefore, the interaction eigenstates, $\tilde{f}_L$ and $\tilde{f}_R$, are expected to differ from the mass eigenstates, $\tilde{f}_1$ and $\tilde{f}_2$ in order of increasing mass. The amount of the left-right mixing is proportional to the corresponding fermion mass, and is negligible for the first two generations.

Among the spin-$\frac{1}{2}$ superpartners, the strongly interacting gluinos $\tilde{g}$ do not mix with other states and their mass is an independent parameter of $\mathcal{L}_{SOFT}$. The weakly interact-

ing spin-$\frac{1}{2}$ sparticles are two charged and four neutral gaugino-higgsino mixtures, called charginos and neutralinos, respectively. The charginos, $\tilde{\chi}_1^{\pm}$ and $\tilde{\chi}_2^{\pm}$ in order of increasing mass, are superpositions of the $\tilde{W}^{\pm}$ winos and $\tilde{H}_2^+, \tilde{H}_1^-$ higgsinos. Similarly, the neutralinos, $\tilde{\chi}_1^0, \tilde{\chi}_2^0, \tilde{\chi}_3^0$ and $\tilde{\chi}_4^0$, are the superpositions of the $\tilde{B}$ bino, $\tilde{W}_3$ wino and $\tilde{H}_1^0, \tilde{H}_2^0$ higgsino states. The masses and couplings of the charginos and neutralinos are characterized by four parameters, the M_1 and M_2 gaugino masses, the μ superpotential Higgs mass and $\tan\beta$.

1.2.3 Supersymmetric Unification

SUSY has the potential to solve the problems of non-SUSY grand unified theories. More remarkably, it provides a framework for the unification of particle physics and gravity.

The basic idea of grand unification [17] is that the gauge interactions as observed at the presently accessible energies, with the different values of their coupling constants, are just the remnants of a theory with a single gauge coupling constant, spontaneously broken at a very high scale, M_U.

The minimal model of supersymmetric grand unification [18] is based on $SU(5)$ and is constructed in analogy with the MSSM. In the leading logarithmic approximation, the predictions just depend on the MSSM particle content. Assuming for simplicity that all supersymmetric particles have masses of the order of m_{Z^0}, one gets $M_U \approx 2 \times 10^{16}$ GeV. This value does not contradict the present experimental limits on the proton lifetime and gives $\sin^2\theta_W$ in agreement with its measured value.

As we have seen, due to the introduction of the soft SUSY breaking terms in the Lagrangian, the MSSM has more than a hundred free parameters. Moreover, there are some phenomenological problems, like non-conservation of the separate lepton numbers, unsuppressed FCNCs and new sources of CP-violation, that are inconsistent with existing experimental bounds.

These problems can be solved by assuming that MSSM can be extrapolated to a very large scale M and imposing a particular structure on the MSSM parameters at this scale.

Treating the parameters of the MSSM as running parameters, using the renormalization group equations, one can derive the low energy MSSM parameters. The initial conditions for the renormalization group equations depend on the mechanism by which SUSY breaking is manifested.

The terms in $\mathcal{L}_{SOFT}$ parametrize our ignorance of the fundamental mechanism of SUSY breaking. To build a theory with spontaneously broken low-energy SUSY, it is convenient (or even necessary) to define two distinct sectors: a *hidden sector* consisting of particles that are completely neutral with respect to the SM gauge group and a *visible sector* containing the MSSM particles. There are no renormalizable tree level interactions between particles in the hidden and visible sectors. SUSY breaking is assumed to occur in the hidden sector and then transmitted to the MSSM.

Since all particles feel the gravitational force, supergravity models provide a natural mechanism to communicate SUSY breaking to the MSSM. In models of *gravity mediated* SUSY breaking, gravity is the messenger [19, 20].

In the scenario of the minimal supergravity [13, 21] the soft SUSY breaking parameters take a particularly simple form at the Planck scale, in which the squared scalar masses and the trilinear couplings are flavour diagonal and universal [19]:

$$\begin{aligned} \tilde{m}_Q^2(M) = \tilde{m}_{U^c}^2(M) = \tilde{m}_{D^c}^2(M) &= \\ \tilde{m}_L^2(M) = \tilde{m}_{E^c}^2(M) &= \\ m_{H_1}^2(M) = m_{H_2}^2(M) &\equiv m_0^2, \end{aligned} \tag{1.37}$$

$$A^U(M) = A^D(M) = A^E(M) \equiv A_0. \tag{1.38}$$

Considering the more general prediction[3] for the gaugino masses

$$M_1(M) = M_2(M) = M_3(M) \equiv m_{1/2}, \tag{1.39}$$

and counting the supersymmetric Higgs mass

$$\mu(M) \equiv \mu_0 \tag{1.40}$$

[3]This relation is valid in both grand unified supergravity and gauge mediated SUSY breaking models, where SUSY breaking is transmitted to the MSSM via gauge forces.

and the SUSY breaking Higgs mixing term

$$m_3^2(M) \equiv (m_3^2)_0, \tag{1.41}$$

we have only five more parameters in addition to the already measured parameters of the SM.

The unification of the gauge coupling constants implies relations between the gaugino mass parameters at the electroweak scale:

$$M_1 = \frac{5g'^2}{3g^2} M_2, \qquad M_3 = \frac{g_s^2}{g^2} M_2. \tag{1.42}$$

Using renormalization group equations one can show that the low energy values of squark and slepton masses depend primarily on m_0^2 and $m_{1/2}^2$. A number of approximate analytic equations for the superpartner masses can be found in [22].

The parameter $(m_3^2)_0$ and μ_0 can be related to the vacuum expectation values of the Higgs fields v_1 and v_2, allowing to use $\tan\beta$ as a model parameter.

1.3 Two-Higgs-Doublet Models

As we have seen, the MSSM Higgs sector contains two complex Higgs field doublets. However, MSSM is not the only model of interest with two Higgs doublets. In general, two-Higgs-doublet models (2HDM) are the minimal extensions of the SM with the fewest new arbitrary parameters, which add new phenomena (for example physical charged Higgs bosons) and satisfy the constraint of $\rho \approx 1$ and the absence of tree level FCNCs, if the Higgs-fermion couplings are appropriately chosen.

The most general Higgs potential which spontaneously breaks $SU(2)_L \times U(1)_Y$ down to $U(1)_Q$ contains six real λ_i parameters and a phase ξ. In a wide range of these parameters, for example if all λ_i are non-negative, the potential has its minimum at

$$\langle \Phi_1 \rangle = \begin{pmatrix} 0 \\ v_1 \end{pmatrix}, \qquad \langle \Phi_2 \rangle = \begin{pmatrix} 0 \\ v_2 e^{\mathrm{i}\xi} \end{pmatrix}, \tag{1.43}$$

which breaks down the electroweak symmetry as desired. The ξ phase can be transformed out if two from the six real λ_i parameters are equal. However, if it can not be eliminated, there is CP violation in the Higgs sector.

As we have already seen in the case of MSSM, these models possess five physical Higgs bosons after the spontaneous symmetry breaking. The ratio of the vacuum expectation values of the two Higgs field doublets, $\tan\beta$, is a key parameter of the model, while $v_1^2 + v_2^2$ is fixed by the $W^{\pm}$ mass. As opposed to the MSSM where only two parameters are needed to describe the Higgs sector before radiative corrections are included, in a general 2HDM we have six free parameters: the four Higgs boson masses, the mixing angle α in the CP-even neutral Higgs sector and $\tan\beta$. No relation can be obtained between the Higgs boson masses.

It is critically important to examine the couplings of the Higgs bosons to the vector bosons and fermions, since they control the production and the decay of the Higgs bosons. Even if one forbids the presence of tree level FCNCs, numerous choices still remain for how to couple the quarks and leptons to the two Higgs doublets. Two choices are studied widely:

Model I All quarks and leptons couple to one Higgs field doublet (H_2), but not to the other one (H_1).

Model II Up-type quarks and neutrinos couple to one Higgs doublet (H_2), while down-type quarks and charged leptons couple to the other one (H_1). This structure is realized in supersymmetric models.

We do not recall the phenomenology of these models here, it is widely discussed in the literature [2].

Chapter 2

The OPAL Experiment

2.1 The LEP Collider

The European Laboratory for Particle Physics, CERN, located near Geneva on both sides of the border between Switzerland and France, operates the Large Electron-Positron Collider (LEP) the largest e^+e^- collider in the world.

The LEP ring is 26.66 km in circumference and consists of eight arcs connected by eight 500 m long straight sections. The four interaction points situated at the middle of every other straight region are equipped with large detectors (ALEPH, DELPHI, L3 and OPAL) to observe the e^+e^- collisions.

The energy loss of the circulating beams through synchrotron radiation is compensated by a 352.2 MHz radio-frequency (RF) system of 272 superconducting and 48 copper accelerating cavities placed in two straight sections of the ring.[1] The beams are bent by dipole magnets installed in the arcs and focused with quadrupole and sextupole magnets. Before crossing each other, the electron and positron bunches are squeezed by superconducting quadrupoles placed on both sides 4 m away from the interaction regions. The beam spot dimensions are $\sigma_x = 200$ μm, $\sigma_y = 8$ μm. Four electron and positron bunches of 1 cm length, containing 4×10^{11} particles per bunch, circulate simultaneously, colliding

[1] All numbers in this section are given for the LEP operation in 1998.

every 22 μs at the interaction points. The maximum beam current exceeds 6 mA and the maximum instantaneous delivered luminosity has reached 10^{32} cm^{-2}s^{-1}. The beam energy uncertainty is 30 MeV at maximum beam energy.

The typical mode of LEP operation (LEP fill) starts with an injection period, when the electrons and the positrons, arriving to the machine with 22 GeV energy from the SPS, are accelerated by the RF system to full energy and the beam parameters are set by squeezing the bunches and optimizing the orbits to yield maximum luminosity. The beams are then kept in collision for about 10 hours.

LEP began operation in the summer of 1989 and for six years the collision energy was tuned to the Z^0 mass (LEP1 phase). Since the autumn of 1995, the beam energy has been increased to more than double its earlier value (LEP2 phase), reaching 94.5 GeV in 1998. It is expected to cross 100 GeV by the end of 1999.

2.2 The OPAL Detector

The **O**mni-**P**urpose **A**pparatus for **L**EP (OPAL) is a large, multi-purpose particle detector designed to reconstruct efficiently and identify with no ambiguity all types of events occurring in electron-positron interactions.

The incoming electrons and positrons approach from opposite directions and collide at the centre of the detector along the beam pipe, an evacuated straight cylinder. The components of the detector are arranged in a layered structure. The three main layers, each of which is further subdivided, are the following:

- The tracking detectors are low density devices placed in a magnetic field. Particles usually loose only a tiny part of their energy in them. However, electrically charged particles cause ionization in the tracking detector materials, which is detected. By measuring its position the path of the charged particles can be reconstructed and their momentum measured from the curvature of their path in the magnetic field.
- The calorimeters are made of high density material in order to stop most of the particles.

When electrons, photons or hadrons interact with the material of the calorimeters, they give rise to showers. The energy of the incoming particle is measured from the properties of these showers.

- On the outside of the detector lies the muon system, which detects the passage of charged particles similarly to the central tracking detectors. Muons are very penetrating particles, and are the only ones which normally reach the muon chambers.

Full details of the OPAL detector, shown in Figure 2.1, can be found in [23] and only a brief review is given below.

2.2.1 OPAL Coordinate System and Track Parameters

The OPAL master reference system is a 3D Cartesian coordinate system whose origin is at the nominal interaction point. The z axis is along the nominal electron beam direction, the x axis is horizontal, directed towards the centre of LEP, and the y axis is normal to the $z-x$ plane. Since the z axis is inclined by 1.39% with respect to the horizontal plane, it follows that the y axis will be similarly inclined with respect to the vertical direction. The θ polar angle is measured from the z axis and the ϕ azimuthal angle from the x axis around the z axis. The r cylindrical coordinate measures the distance from the z axis, while s is the track path-integral in the $r-\phi$ plane.

The OPAL central detector track parameters $(\kappa,\ \phi_0,\ d_0,\ \tan\lambda,\ z_0)$ are defined in the following way:

- κ is the curvature of the track produced by the magnetic field in the detector, with

$$|\kappa| = \frac{1}{2\rho}$$

  where ρ is the radius of curvature of the track and κ is signed so that positive κ means that ϕ increases along the track. Note that for an axial magnetic field with B_z along the positive z axis, positive κ corresponds to a particle with negative physical charge.
- ϕ_0 is the azimuthal angle of the track tangent at the point of closest approach to the origin (p.c.a.)

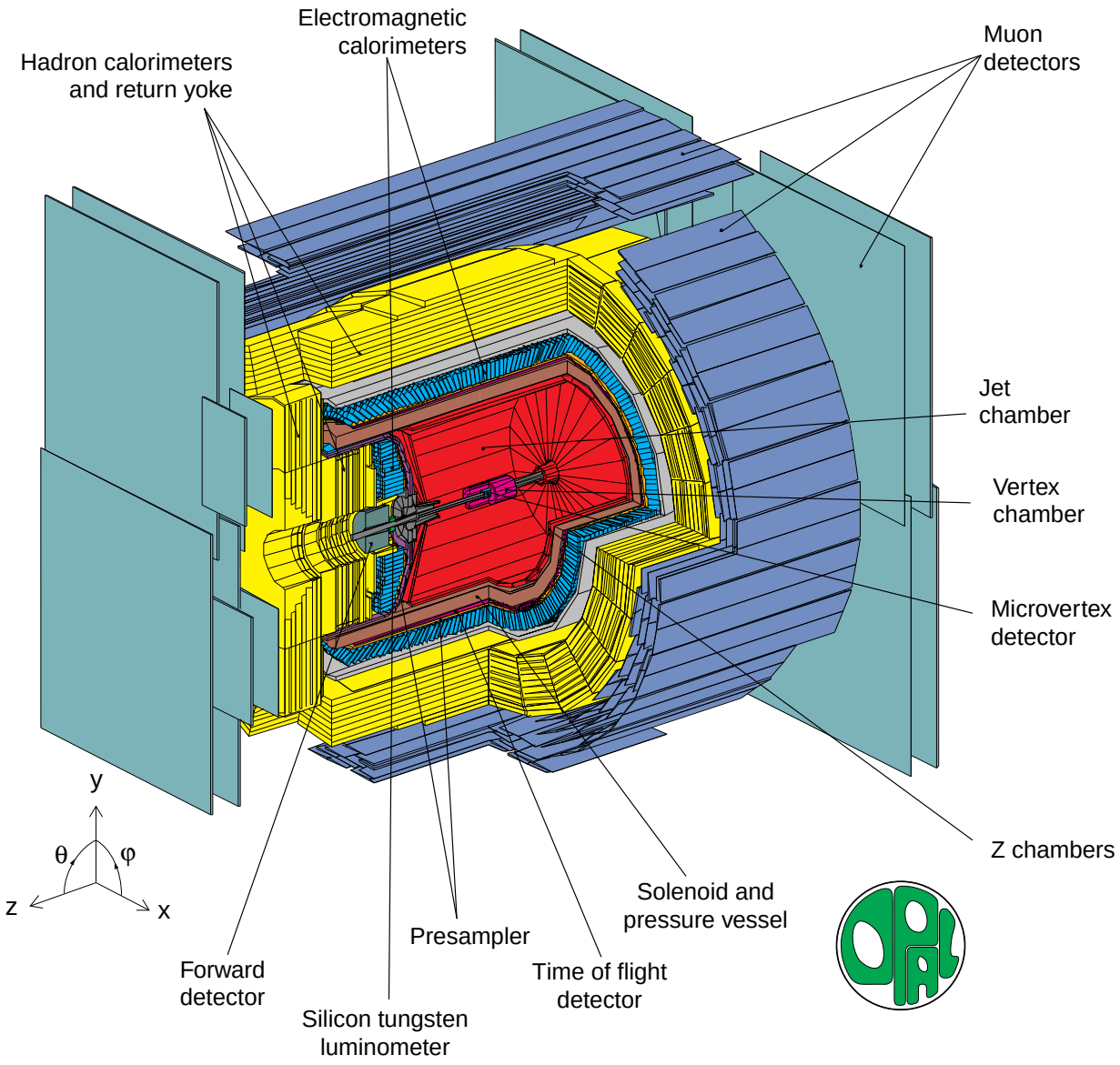

Figure 2.1: *The OPAL detector.*

- d_0 is the impact parameter, i.e. $|d_0|$ is the distance from the origin to the p.c.a. Defining $\vec{d}$ as the vector from the origin to the p.c.a., $\hat{\phi}$ as the unit track vector at the p.c.a. and $\hat{z}$ as the unit vector along the z axis, then formally:

$$d_0 = \hat{\phi} \times \vec{d} \cdot \hat{z}$$

- $\tan\lambda = \cot\theta$, where θ is the track polar angle measured from the positive z axis.
- z_0 is the z co-ordinate when the track is at the p.c.a. The $s-z$ projection of the helix is then:

$$z = z_0 + s\tan\lambda$$

  where s is the $r-\phi$ path integral from the p.c.a.

The impact parameter d_0 is defined with respect to the origin of the coordinate system and not with respect to the actual beam interaction point. The corrected impact parameter, calculated with respect to a point (x_v, y_v), usually chosen to be the primary event vertex or the average beam position, is defined as

$$d_{0\ \mathrm{corr}} = d_0 + x_v \sin\phi_0 - y_v \cos\phi_0$$

2.2.2 Central Detector

The central detector, providing high precision tracking of charged particles in the central region, consists of a silicon microvertex detector [24] and three drift chamber devices: the vertex detector, the jet chamber and the surrounding Z-chambers. It is situated inside a pressure vessel holding a pressure of 4 bar and a solenoid supplying a uniform axial magnetic field of 0.435 T. Originally the inner wall of the pressure vessel, a 0.13 cm thick carbon fibre with a 100μm aluminium inner lining at 7.8 cm radius, formed the beam pipe. In 1991 a second beam pipe of 0.11 cm thick beryllium at a radius of 5.35 cm was added and the silicon microvertex detector inserted between them.

Silicon Microvertex Detector

The silicon microvertex detector has been upgraded several times between 1993 and 1996. Now it consists of two barrels of single sided silicon microstrip detectors at radii of 6.0 and 7.5 cm with a polar angle coverage of $|\cos\theta| < 0.9$. The inner layer consists of 12 ladders and the outer of 15 ladders tilted to close ϕ gaps. Each ladder is 18 cm long and consists of three $r-\phi$ and two $r-z$ silicon wafers daisy chained together. The $r-\phi$ and $r-z$ wafers are glued back to back. There are 629 strips per detector at 25μm pitch and every other strip is read out at 50μm pitch.

The installation of the silicon microvertex detector allows precise vertex reconstruction and significantly improves the impact parameter rms. resolutions both in the $r-\phi$ and $s-z$ plane: $\sigma_{r-\phi} = 18$ μm, $\sigma_{s-z} = 24$ μm for tracks emerging normal to the beam direction.

Vertex Detector

The vertex detector is a high precision cylindrical drift chamber of 100 cm length with a radius of 23.5 cm. It consists of two layers of 36 sectors each. The inner layer contains the axial sectors, each with 12 sense wires parallel to the beam direction, ranging radially from 10.3 to 16.2 cm. The outer layer contains the stereo sectors each with 6 sense wires inclined at a stereo angle of $\sim 4^\circ$, lying between the radii 18.8 and 21.3 cm.

A precise measurement of the drift time on to the axial sector sense wires allows the $r-\phi$ position to be calculated with 55μm resolution. Measuring the time difference between signals at either end of the sense wires allows a fast but relatively coarse z coordinate that is used by the OPAL track trigger and in pattern recognition. A more precise z measurement is then made by combining axial and stereo drift time information off-line resulting in 700μm resolution. Multiple hits on a wire can be recorded.

Jet Chamber

The jet chamber is a cylindrical drift chamber of length 400 cm with an outer radius of 185 cm and an inner one of 25 cm. The chamber consists of 24 identical sectors each containing 159 sense wires strung parallel to the beam direction.

The coordinates of wire hits in the $r-\phi$ plane are determined from a measurement of the drift time with 135 μm resolution. The z coordinate is measured using a charge division technique resulting in a resolution of 6 cm. Summing the charges received at each end of a wire allows the energy loss, $\mathrm{d}E/\mathrm{d}x$, to be calculated and used for charged particle identification.

Z-Chambers

The Z-chambers provide a precise measurement of the z coordinate of tracks with 100 to 350 μm resolution as they leave the jet chamber. They consist of a layer of 24 drift chambers 400 cm long, 50 cm wide and 5.9 cm thick covering 94% of the azimuthal angle and the polar angle range $|\cos\theta|< 0.72$. Each chamber is divided in z into 8 cells of 50 cm$\times$50 cm, with every cell containing 6 sense wires spaced at 0.4 cm.

2.2.3 Electromagnetic Calorimeter

The electromagnetic calorimeter is built to detect and identify electrons and photons. It consists of a lead glass total absorption calorimeter split into a barrel and two endcap arrays. This arrangement together with the two lead scintillator calorimeters of the forward detector makes the OPAL acceptance for electron and photon detection almost 99% of the solid angle.

The presence of $\sim$2 radiation lengths of material in front of the calorimeter, mostly due to the solenoid and pressure vessel, results in most electromagnetic showers initiating before reaching the lead glass. Presampling devices are therefore installed in front of the lead glass to measure the position and energy of showers to improve overall spatial and energy resolution and give additional γ/π^0 and electron/hadron discrimination.

Time-of-Flight Counters

The barrel time-of-flight system, in front of the barrel presampler, provides charged particle identification in the range 0.6 to 2.5 GeV, fast triggering information and an effective

rejection of cosmic rays. It consists of 160 scintillation counters forming a barrel layer 684 cm long at a mean radius of 236 cm surrounding the magnet coil covering the polar angle range $|\cos\theta| < 0.82$.

In 1996 the tile endcap system [25] was added to enhance the triggering information available from the forward region. It consists of a 10 mm thick scintillator layer, between the endcap presampler and the endcap electromagnetic calorimeter covering the polar angle range $0.82 < |\cos\theta| < 0.95$. It is divided into 120 tiles in each endcap and read out using embedded wavelength-shifting fibres.

Electromagnetic Presampler

The barrel electromagnetic presampler consists of 16 chambers forming a cylinder of radius 239 cm and length 662 cm covering the polar angle range $|\cos\theta| < 0.81$. Each chamber consists of two layers of drift tubes with the anode wires running parallel to the beam direction. Each layer of tubes contains 1 cm wide cathode strips on both sides at $\pm 45^\circ$ to the wire direction. Spatial positions can then be determined by reading out the strips in conjunction with a measurement of the charge collected at each end of the wires to give a z coordinate by charge division. The hit multiplicity is approximately proportional to the energy deposited in the material in front of the presampler allowing the calorimeter shower energy to be corrected.

The endcap presamplers are multiwire proportional counters located in the region between the pressure bell and the endcap lead glass detector on both sides. They consist of 32 chambers arranged in 16 sectors covering the polar angle range $0.83 < |\cos\theta| < 0.95$.

Lead Glass Calorimeters

The barrel lead glass calorimeter consists of a cylindrical array of 9440 lead glass blocks at a radius of 246 cm covering the polar angle range $|\cos\theta| < 0.81$. Each block is 24.6 radiation lengths, 37 cm in depth and $\sim 10 \times 10$ cm^2 cross-section. In order to maximize detection efficiency, the longitudinal axis of each block is angled to point at the interaction

region. The focus of this pointing geometry is slightly offset from the e^+e^- collision point in order to reduce particle losses in the gaps between blocks. Čerenkov light from the passage of relativistic charged particles through the lead glass is detected by 3 inch diameter phototubes at the base of each block.

The endcap electromagnetic calorimeter consists of two dome-shaped arrays of 1132 lead glass blocks located in the region between the pressure bell and the poletip hadron calorimeter. It has an acceptance coverage of $0.81 < |\cos\theta| < 0.98$. As opposed to the barrel calorimeter, the endcap lead glass blocks follow a non-pointing geometry being mounted coaxial with the beam line. The lead glass blocks provide typically 22 radiation lengths of material and come in three lengths (38, 42 and 52 cm) to form the domed structure following the external contours of the pressure bell. The blocks are read out by special vacuum photo triodes operating in the full OPAL magnetic field.

The energy resolution is $0.2\% + 6.3\%/\sqrt{E}$ in the barrel and around $5\%/\sqrt{E}$ for low energy in the endcap region. The overall spatial resolution using also the presampler devices for electromagnetic showers is $2 - 5$ mm.

2.2.4 Hadron Calorimeter

The hadron calorimeter is built in three sections: the barrel, the endcaps and the pole-tips. By positioning detectors between the layers of the magnet return yoke a sampling calorimeter is formed covering a solid angle of 97% of 4π and offering at least 4 interaction lengths of iron absorber to particles emerging from the electromagnetic calorimeter. Essentially all hadrons are absorbed at this stage leaving only muons to pass on into the surrounding muon chambers.

The hadron calorimeter information must be used in combination with that from the preceding electromagnetic calorimeter due to the likelihood of hadronic interactions occurring in the 2.2 interaction lengths of material before the hadron calorimeter.

The barrel region contains 9 layers of chambers interlaced with 8 layers of 10 cm thick iron. The barrel ends are then closed off by toroidal endcap regions which consist of 8

layers of chambers with 7 slabs of iron.

The chambers themselves are limited streamer tube devices strung with anode wires 1 cm apart. The signals from the wires are used only for monitoring purposes. The chamber signals result from induced charge collected on pads and strips located on the outer and inner surfaces of the chambers, respectively.

The layers of pads are grouped together to form towers that divide up the detector volume into 48 bins in ϕ and 21 bins in θ. The analogue signals from the 8 pads in each chamber are then summed up to produce an estimate of the energy in hadronic showers.

The strips consist of 0.4 cm wide aluminium that run the full length of the chamber, centred above the anode wire positions. They hence run parallel to the beam line in the barrel region and in a plane perpendicular to this in the endcaps. Strip hits thus provide muon tracking information with positional accuracy limited by the 1 cm wire spacing.

Complementing the barrel and endcap regions, the pole-tip extends the coverage of hadron calorimetry from $|\cos\theta| = 0.91$ down to 0.99. The number of layers in this region is increased to 10. The detectors themselves are 0.7 cm thick multiwire proportional chambers with anode wires at a spacing of 0.2 cm. Again, the chambers have pads on one side (of typical area 500 cm^2) and strips on the other. Corresponding pads from the 10 layers then form towers analogous to the treatment in the rest of the calorimeter.

2.2.5 Muon Detector

The muon detector aims to identify muons in an unambiguous way from a potential hadron background. Particles incident on the detector have traversed the equivalent of 1.3 m of iron so reducing the probability of a pion not interacting to be less than 0.001, making the background manageable.

The barrel region consists of 110 drift chambers that cover the acceptance $|\cos\theta| < 0.68$ with four layers and $|\cos\theta| < 0.72$ with one or more layers. The chambers range in length between 10.4 m and 6 m in order to fit between the magnet support legs and all have the same cross sectional area of 120 cm$\times$9 cm.

The barrel chambers are split into two adjoining cells, each containing an anode signal wire running the full length of the cell, parallel to the beam line. The inner surfaces of the cells have 0.75 cm cathode strips etched in them to define the drift field, and in the regions directly opposite the anode wires are diamond shaped cathode pads.

Spatial position in the ϕ plane is derived using the drift time onto the anode and can be reconstructed to an accuracy of better than 0.15 cm. A rough estimate of the z coordinate is also achieved by using the difference in time and pulse height of the signals arriving at both ends of the anode wire. A much better measurement of the z coordinate is given by using induced signals on two sets of cathode pads whose diamond shape repeats every 17.1 cm and 171 cm respectively. This results in a z coordinate accurate to 0.2 cm modulo 17.1 cm or accurate to 3 cm modulo 171 cm.

Each endcap muon detector consists of two layers of four quadrant chambers (6 m×6 m) and two layers of two patch chambers (3 m×2.5 m), for an angular coverage of $0.67 < |\cos\theta| < 0.985$. Each chamber is an arrangement of two layers of limited streamer tubes in the plane perpendicular to the beam line, where one layer has its wires horizontal and the other vertical.

The basic streamer tube used has a cross section of 0.9 cm×0.9 cm with the inner walls coated with a carbon-suspension cathode. Each plane of tubes is open on one side and closed on the other. The strips on the open side run perpendicular to the tube anode wires and typically have charge induced over five or so strips. By finding a weighted average using the recorded pulse heights, the streamer is located to better than 0.1 cm. The strips on the closed side run parallel to the tube wires and so can only give that coordinate to the nearest wire or $0.9/\sqrt{12}$ cm.

2.2.6 Forward Detector

The forward detector consists of an array of devices, listed below, whose primary objective is to detect low angle Bhabha scattering events as a way of determining the LEP luminosity. It enjoys a relatively clean acceptance for particles between 47 and 120 mrad from the

interaction point, with the only obstructions being the beam pipe and 2 mm of aluminium from the central detector pressure vessel.

Calorimeter

The forward calorimeter consists of 35 sampling layers of lead-scintillator sandwich divided into a presampler of 4 radiation lengths and the main calorimeter of 20 radiation lengths.

Tube Chambers

There are three layers of proportional tube chambers positioned between the presampler and main sections of the calorimeter. The positioning is known to ± 0.05 cm and they can give the position of a shower centroid to ± 0.3 cm.

Gamma Catcher

The gamma catcher is a ring of lead scintillator sandwich sections of 7 radiation lengths thickness. They plug the hole in acceptance between the inner edge of the endcap electromagnetic calorimeter and the start of the forward calorimeter.

Far Forward Monitor

The far forward monitor counters are small lead-scintillator calorimeter modules, 20 radiation lengths thick, mounted on either side of the beampipe at 7.85 m from the intersection region. They detect electrons scattered in the range 5 to 10 mrad that are deflected outwards by the action of LEP quadrupoles.

2.2.7 Silicon Tungsten Luminometer

The silicon tungsten luminometer [26] is a sampling calorimeter designed to detect low angle Bhabha scattering events in order to measure the luminosity. There are two calorimeters at ± 238.94 cm in z from the interaction point with an angular acceptance of 25 mrad to 59 mrad. Each calorimeter consists of 19 layers of silicon detectors and 18 layers of

tungsten. At the front of each calorimeter is a bare layer of silicon to detect preshowering, the next 14 silicon layers are each behind 1 radiation length (3.8 mm) of tungsten and the final 4 layers are behind 2 radiation lengths of tungsten.

Each silicon layer consists of 16 wedge shaped silicon detectors with an inner radius at 6.2 cm and an outer one at 14.2 cm. The wedges are subdivided into 64 pads (32 in r and 2 in ϕ) giving a total of 38912 channels which are read out individually. The wedges are positioned in such a way that there is no gap in the active area of the silicon.

2.2.8 MIP Plug

In 1997 a system of scintillating tiles [25] was added to the forward region covering the polar angle range 43 mrad $< \theta <$ 200 mrad. It consists of two 10 mm thick scintillator layers placed before and after the silicon tungsten luminometer and divided into 32 tiles in both sides of the detector. Like the tile endcap system it is read out using embedded wavelength-shifting fibres.

2.2.9 Trigger

Events are only recorded by the data acquisition system if they satisfy certain trigger and pretrigger conditions. The trigger logic [27] is based on information from most of the detectors, comprising a track trigger, a time-of-flight trigger, electromagnetic and hadron calorimeter triggers as well as muon detector and forward detector triggers. A high level of redundancy and fine detector segmentation at the trigger level lead to a high efficiency for all considered physics reactions while the trigger rates are kept low to minimize the deadtime needed to read out triggered events.

The subdetector trigger signals are divided into two categories, stand-alone direct signals such as multiplicity counts or energy sums generated by the individual subdetectors and low threshold signals from a coarse segmentation in solid angle, typically 6×24 bins in θ/ϕ, possibly taking into account correlations between subdetectors. The central trigger processor performs a programmable logical combination of these signals to derive the over-

all trigger decision. A positive decision initiates digitization and readout of the event data, coordinated on the subdetector level by the local trigger units, while a negative decision resets the electronics of all detector components and prepares them for the next bunch crossing.

The pretrigger system [28] was designed to derive a decision without deadtime even in 8+8 bunch mode operation of LEP, with 11.1 μs bunch-crossing interval. This system was implemented complementing the original trigger system, which needed only minor modifications. The combined trigger system is shown in Figure 2.2.

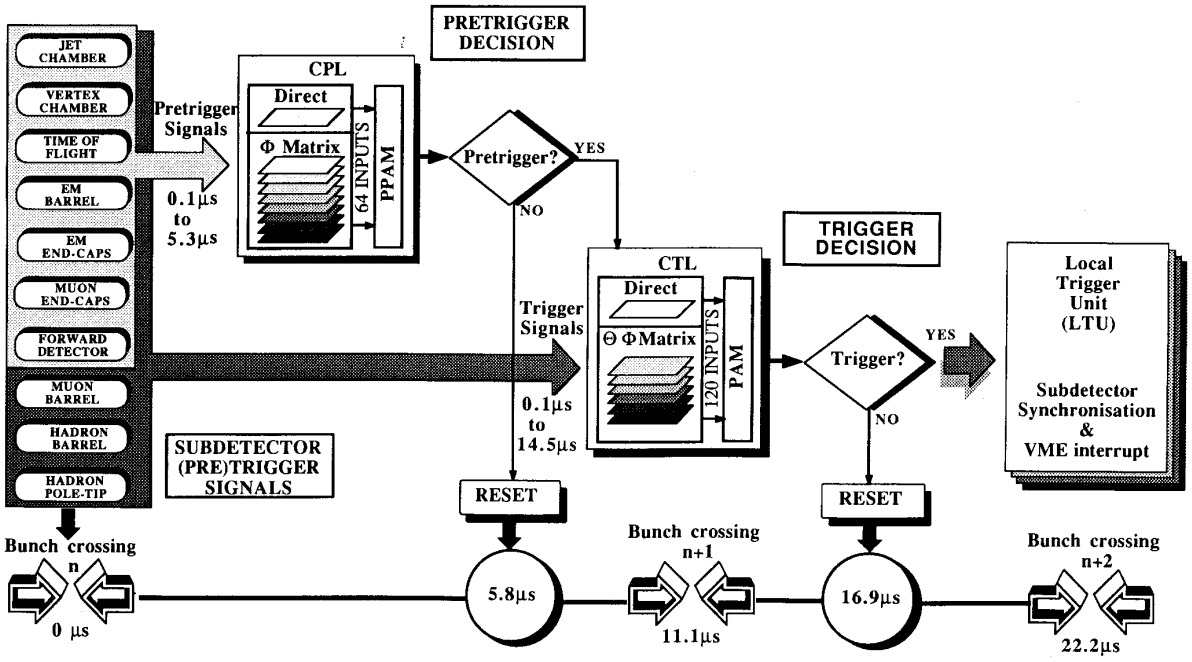

Figure 2.2: *Overview of event triggering.*

Similar to trigger signals, pretrigger signals are divided into direct signals and low threshold signals, consisting of 12 overlapping sectors in ϕ. Eight subdetectors generate low-threshold signals: the vertex chamber, the jet chamber, the time-of-flight counter, the electromagnetic barrel and endcap calorimeters and the muon endcap calorimeters. The hadron calorimeters do not contribute and the muon barrel chambers are excluded because the drift time is too long. A direct signal from the forward detector completes the angular coverage.

Several of the eight subdetector signals are fully or partially sensitive to each type of particle. Multiplicity counting and spatial correlations both within and between subdetectors, together with direct signals, provide a large number of independently formed pretrigger conditions in both the barrel and endcap regions, which are combined into the final decision by programmable logic circuits.

The simplicity and flexibility of the trigger design, combined with high redundancy of trigger signals in all physics channels enable the detector to trigger with high efficiency and low rate at varying luminosity and background conditions.

2.2.10 Online Dataflow

When a beam crossing is selected by the trigger as containing a potentially interesting event, the subdetectors are read out. Each one of the subdetectors is read out separately by its own special front-end electronics into its local system crate(s) (LSC). Data reduction, such as pedestal subtraction, zero-suppression and pulse-shape analysis is performed. The subevent structures from the different LSCs (including the trigger and track trigger) are assembled by the event builder (EVB).

When the complete events have been assembled by the EVB, they are passed in sequence to the filter [29], where they are checked, analysed, monitored and compressed before being written to disk. Some obvious background events, such as cosmic rays, typically 15-35 % of all triggers, are rejected. The events are then written in data files. Several other files are stored, for example the one containing calibration information.

Data copied from the filter are written to optical disk as a permanent storage, and reconstructed by the OPAL event reconstruction software ROPE when the required calibration constants are available. Events passing a loose physics selection are stripped off and copied over the network onto permanent disk storage and also backed up on cartridge. Fully reconstructed events are available for analysis when moved to this permanent storage area, usually within a few hours of the end of a run.

Chapter 3

The Analysis Flow

In experimental high energy physics Monte Carlo simulation is the practical implementation of theoretical results, it provides a way for the theory to enter the analysis and the interpretation of the experimental data. It is not our aim to describe the current state of art of Monte Carlo simulation, in the next section we merely list the programs used to model the different physics processes and refer to the literature for more information.

In search analyses we compare our data to the model expectations and look for a theoretically predicted signal above the SM background. The analysis of the data is optimized using the properties of the signal events, which are generated assuming the underlying new physics we are looking for. The same analysis flow is applied to the experimental data and the Monte Carlo events.

Only experimental events that have been triggered and recorded are considered. They have to pass certain loose requirements applied on-line and designed to have nearly 100% efficiency for the given class of events, using fast information. A more sophisticated, but still general, off-line selection is applied to both the data and the Monte Carlo samples before they enter our analysis optimized for the search of a given new particle.

The first step is to select charged particle tracks and energy deposits in the calorimeters to be used in the event reconstruction by means of quality cuts. Their energy is corrected for detector effects to improve the energy and momentum resolution.

We then look for characteristic physical objects in the event, *identify leptons* and *reconstruct jets* originating from the hadronization of quarks. To take into account certain physical constraints, for example energy and momentum conservation, these objects (leptons and jets) are subject to *kinematic fits*.

We continue with the selection of the interesting events using simple *cuts* on experimental variables or using more sophisticated methods such as a *likelihood selection*. The latter combines the information of several experimental variables in order to determine the probability that an event belongs to a given class of physics processes.

In this chapter, we explain these analysis steps in detail. Most of the methods have been improved during the years, and the descriptions given here correspond to their current state. Where it is important we also give the modifications applied.

Our searches have not revealed any statistically consistent difference between the experimental data and the SM expectation. No excess of events over the SM predictions has been observed. In the last section we review the statistical methods used to derive the 95% confidence level (CL) limits on the production cross-sections of new physics processes.

3.1 Monte Carlo Simulation

SM processes occurring in e^+e^- collisions at LEP appear as experimental backgrounds in new particle searches. Therefore, the understanding and the best possible simulation of these processes are crucial points in any analysis looking for new phenomena beyond the SM.

3.1.1 Two-Fermion Processes

Quark and lepton pair production (Figure 3.1) in Z^0 decays has been tested very precisely at LEP1. At higher energies, as one moves away from the Z^0 peak, the cross-section falls rapidly and the photon exchange becomes important. This process, however, still remains dominant as shown in Figure 3.2 [30].

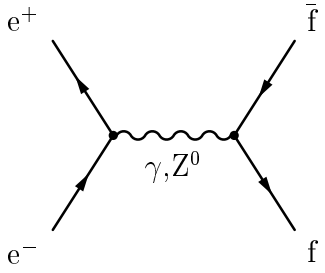

Figure 3.1: *Feynman diagram for fermion pair production.*

Initial state radiation plays a very important role. The fast decrease of the cross-section favours the radiation of hard photons (Figure 3.3) that boost the effective two-fermion centre-of-mass energy back to the Z^0 mass in a process called radiative return.

Lepton-pair processes are simulated using the generators BHWIDE [31] for $e^+e^-(\gamma)$ and KORALZ [32] for $\mu^+\mu^-(\gamma)$ and $\tau^+\tau^-(\gamma)$ events.

For hadronic final states one has also to consider final state gluon radiation. Quark pair events with hard gluon emission (Figure 3.4) give a severe background for multijet final states.

Hadronic events are simulated with the parton-shower approach using PYTHIA [33]. Here, perturbative QCD and QED are applied to evolve the initial $q\bar{q}$ pair into a more complex state, usually involving additional quarks, gluons and photons, determining the overall topology of the event. The initial quarks can emit a gluon, and the new quarks and gluons produced are allowed an arbitrary number of successive branchings, such as $q \to qg$, $\bar{q} \to \bar{q}g$, $g \to gg$ and $g \to q\bar{q}$, resulting in the parton shower. During the shower final state photons can also be emitted. For systematic studies Monte Carlo samples are also generated by the HERWIG [34] package.

3.1.2 Four-Fermion Processes

Four-fermion processes, especially above the W^+W^- production threshold at 161 GeV, have a major role. These are not only due to real W^+W^- and Z^0Z^0 production, but arise

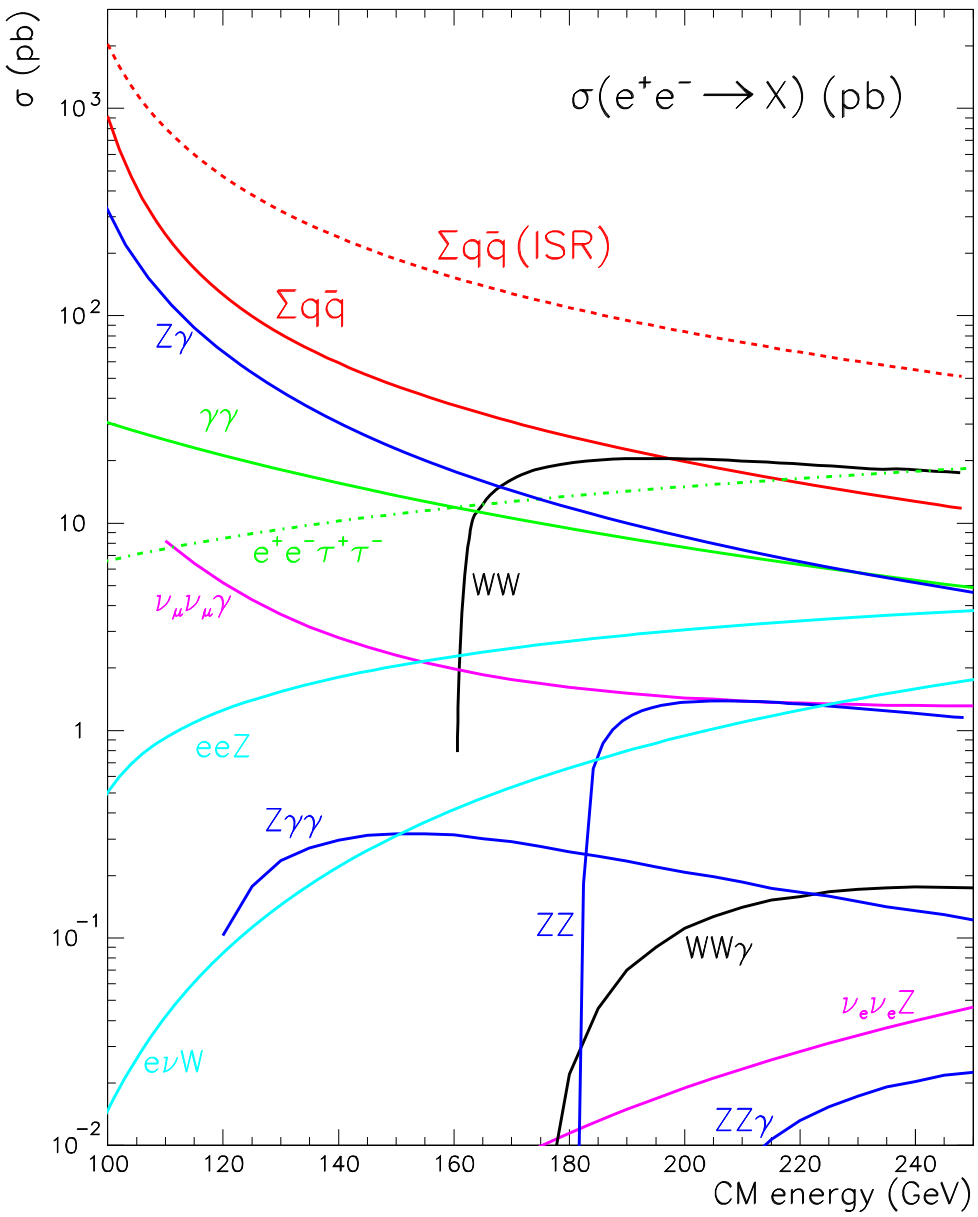

Figure 3.2: *Cross-sections of some typical SM processes. For* $e^+e^-Z^0$, $\nu_e\bar{\nu}_eZ^0$ *and* $e^\pm\nu_eW^\mp$ *only the dominant t-channel contribution is shown. In* $Z^0\gamma$ *and* $\gamma\gamma$ *the photons are such that* $|\cos\alpha_{e\gamma}| < 0.9$. *For* $\nu_\mu\bar{\nu}_\mu\gamma$ *there is an additional cut* $E_\gamma > 10$ *GeV. In* $Z^0Z^0\gamma$, $Z^0\gamma\gamma$ *and* $W^+W^-\gamma$ *the photons have* $p_T^\gamma > 10$ *GeV and all particles are separated with opening angles* $\alpha_{eV} > 15°$ *and* $\alpha_{VV'} > 10°$ *with* $V, V' = W^\pm, Z^0$ *or* γ.

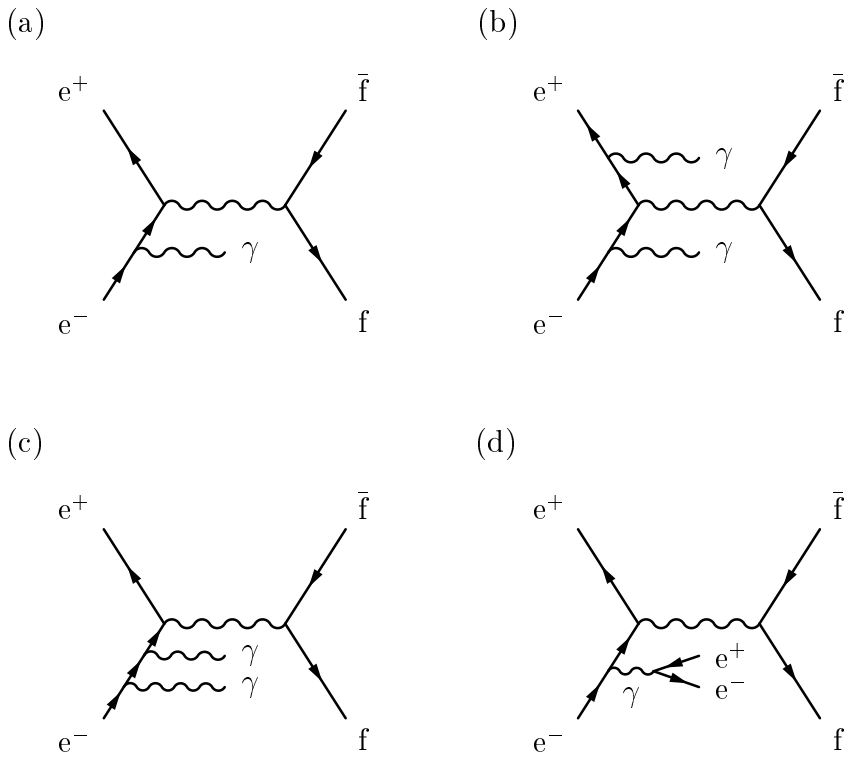

Figure 3.3: *Feynman diagrams for fermion pair production with initial state radiation: processes with (a) single photon radiation, (b-c) double photon radiation and (d) photon conversion into an* e^+e^- *pair.*

from several production mechanisms. In Figure 3.5 all the possible classes of four-fermion production diagrams are shown, except the ones involving Higgs bosons. The largest total cross-section arises from multipheripheral diagrams, where two quasi-real photons are exchanged in the t-channel, giving rise to usually undetected forward electrons and positrons plus a fermion pair with a non-resonant structure. These are called two-photon processes. For our work the most important background comes from W^+W^- production, for which the available high statistics MC samples describe well the experimental observations [35].

One should proceed with caution when simulating four-fermion events, since several diagrams may contribute to any given final state. Moreover, in final states containing electrons, it is usually necessary to place generator level cuts, such as cuts on the polar

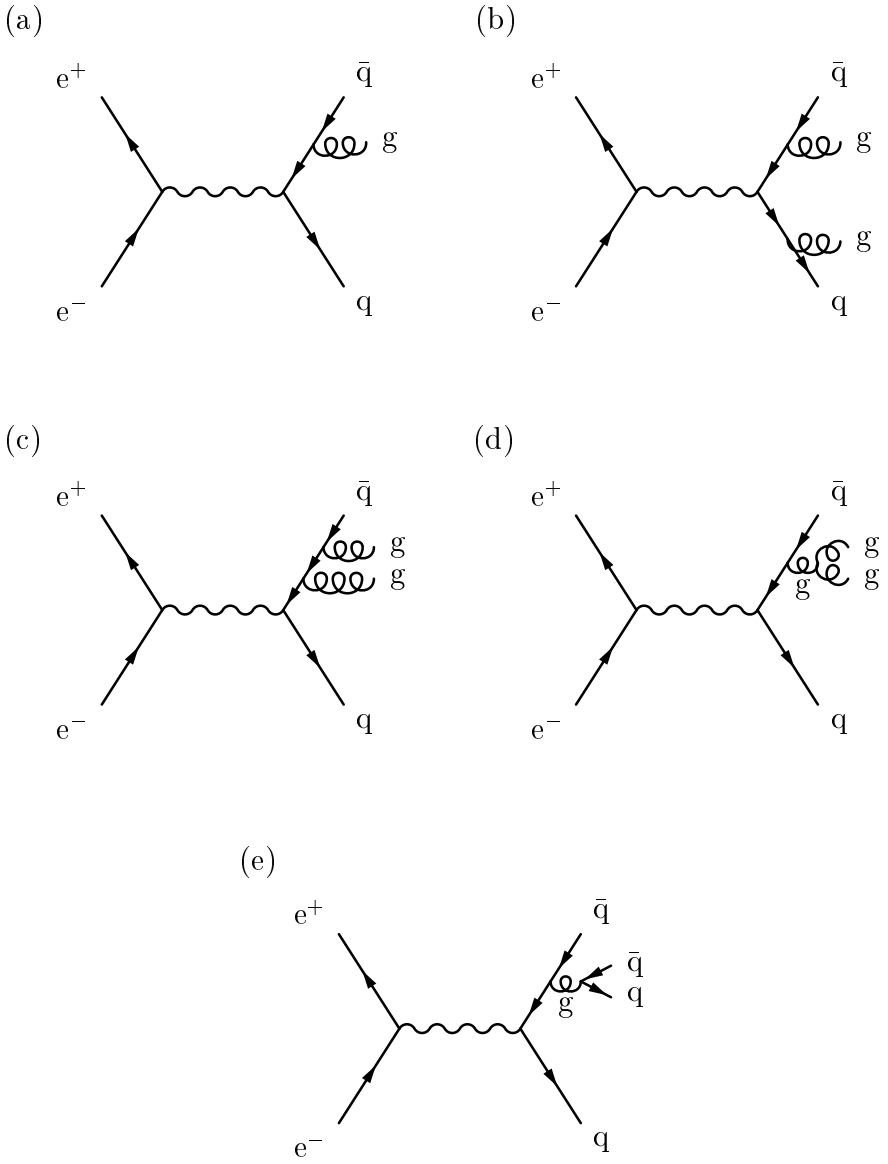

Figure 3.4: *Feynman diagrams for quark pair production with hard gluon emission: processes with (a) single gluon radiation, (b-c) double gluon radiation, (d) non-Abelian gluon radiation and (e) gluon conversion into a quark pair.*

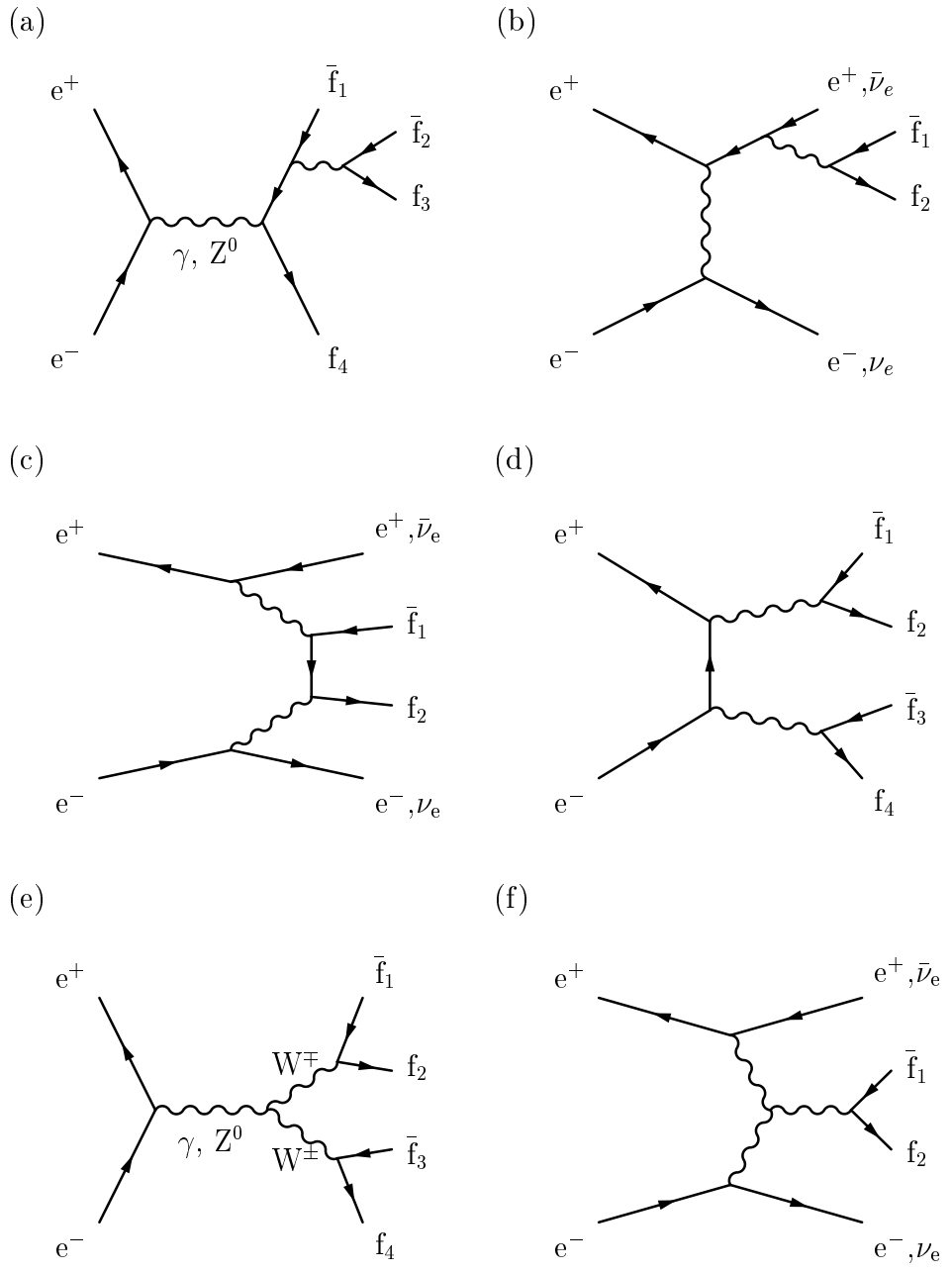

Figure 3.5: *Feynman diagrams for four-fermion production: (a) Abelian annihilation, (b) bremsstrahlung, (c) multipheripheral, (d) conversion, (e) non-Abelian annihilation and (f) fusion processes. The inner vector boson lines may correspond to* γ, Z^0 *or* $W^{\pm}$ *exchange, unless otherwise indicated.*

angle and the momentum transverse to the beam direction of the outgoing particles, or on the invariant mass of the fermion-pair in the case of two-photon processes.

For four-fermion processes a wide range of Monte Carlo generators are available of which we have used `grc4f` [36] and for systematic studies EXCALIBUR [37] and PYTHIA. The $W^{\pm}$ boson mass is taken to be 80.33 GeV. The two-photon processes are treated separately and simulated by PHOJET [38], HERWIG and PYTHIA in $e^+e^-q\bar{q}$ final states and by Vermaseren [39] in $e^+e^-\ell^+\ell^-$ final states.

3.1.3 Higgs Boson and Supersymmetric Particle Production

The production and decay of Higgs bosons are simulated using HZHA [40], except charged Higgs bosons at centre-of-mass energies of 161 and 172 GeV for which PYTHIA is used. R-parity violating decays of supersymmetric particles are modelled by SUSYGEN [41].

As a general rule, the generated masses of the particles have been chosen to cover the range between the masses already excluded and the kinematic or sensitivity limit at the given center-of-mass energy.

3.1.4 Common Features

In all generators both initial and final state electromagnetic radiations are taken into account.

The generated partons are hadronized using the JETSET [33] package[1] with parameters tuned to OPAL event shape measurements as described in [42]. The hadronization process, the confinement of quarks and gluons into experimentally observable hadrons, can not be calculated using perturbation theory, it is the subject of fragmentation models. The quark fragmentation into hadrons is modelled using the string fragmentation approach. The energy and momentum fractions of the parton shower quark carried away by the newly formed hadron are specified as a probability function $f(z)$ of the variable $z = \frac{(E+p_{\mathrm{L}})_{\mathrm{hadron}}}{(E+p_{\mathrm{L}})_{\mathrm{quark}}}$,

[1] The only exceptions are the events generated by HERWIG, which also handles hadronization. The JETSET decay tables are used even for these events.

where E is the energy and p_L is the longitudinal momentum with respect to the direction of flight of the quark. Heavy flavour hadrons have a hard fragmentation, on average they carry a larger fraction of momentum than lighter hadrons do. The best description of data can be achieved using Symmetric LUND fragmentation [43] for light quarks and Peterson fragmentation [44] for charm and bottom quarks.

The states produced in the fragmentation process are allowed to decay into stable (long lived) particles.

To include the detector response, all generated events are processed by the OPAL detector simulation program GOPAL [45] based on the GEANT package [46], and then dpassed through the ROPE event reconstruction program, just like the experimental data.

3.2 Analysis Tools

3.2.1 Standard Event Selections

Events before entering our analysis should pass general on-line and off-line [47, 48] selection criteria described below.

On-Line High Multiplicity Selection

This on-line selection using fast information has almost 100% efficiency for hadronic Z^0 decays. An event is selected if it satisfies any of the two sets of requirements:

(A) There are at least five tracks having all of the following properties:

- the momentum transverse to the beam direction $p_T \geq 100$ MeV;
- the polar angle $|\cos\theta| \leq 0.966$;
- the impact parameter in the $r-\phi$ projection $|d_0| \leq 2.5$ cm;
- the impact parameter in the $s-z$ projection $|z_0| \leq 50.0$ cm;
- the number of hits in the jet chamber $N_{\text{CJ hits}} \geq 20$ and $N_{\text{CJ hits}} \geq 50\%$ of the maximum possible number of hits at the polar angle of the track.

(B) The following properties are fulfilled:

- the number of electromagnetic calorimeter clusters[2] with an initiating block of at least 100 (200) MeV with a nearest neighbour of at least 50 (100) MeV in the barrel (endcap) region, $N_{\text{clusters}} \geq 6$;
- the sum of the energy of the clusters satisfying the above criteria $\sum E_{\text{cluster}} > 8$ GeV;
- the sum of the energy of the clusters in the hemisphere opposite to the highest energy cluster $\sum E_{\text{cluster}} > 2$ GeV;
- the number of hits in the time-of-flight counter $N_{\text{TOF}} \geq 3$, if in the barrel region $\sum E_{\text{cluster}} > 2$ GeV and $N_{\text{clusters}} \geq 2$.

Off-Line Multihadron Selection

An event is selected if it satisfies all of the following requirements:

(A) There should be at least five well-measured tracks originating from the electron-positron interaction, namely having

- the number of hits in the three central drift chambers $N_{\text{CD hits}} \geq 20$;
- the impact parameter in the $r-\phi$ projection $|d_0| \leq 2.0$ cm;
- the impact parameter in the $s-z$ projection $|z_0| \leq 40.0$ cm;
- the radius of the first hit along the track $R_{\text{1st hit}} \leq 60.0$ cm;
- the momentum transverse to the beam direction $p_{\text{T}} \geq 50$ MeV;
- the polar angle $|\cos\theta| \leq 0.995$;
- the χ^2 per degree of freedom of the track fit in the $r-\phi$ projection $\chi^2_{r-\phi} \leq 999$;
- the χ^2 per degree of freedom of the track fit in the $s-z$ projection $\chi^2_{s-z} \leq 999$.

(B) There should be at least seven well-measured electromagnetic calorimeter clusters having

[2]The sets of neighbouring blocks in the calorimeters, in which an energy deposit is observed, are called *clusters*.

- the uncorrected energy $E_{\rm raw} \geq 100$ (200) MeV in the barrel (endcap) region;
- the number of blocks $N_{\rm blocks} \geq 1$ (2) in the barrel (endcap) region.

(C) Two ratios are defined:

$$R_{\rm shw} = \frac{E_{\rm shw}}{2 \times E_{\rm beam}} \quad \text{and} \quad R_{\rm bal} = \frac{E_{\rm bal}}{E_{\rm shw}},$$

with $E_{\rm shw} = \sum E_{\rm raw}$ and $E_{\rm bal} = \sum E_{\rm raw} \cos\theta$. Here θ is the polar angle of the cluster and the sums are over the $N_{\rm shw}$ clusters passing the requirements listed above. Events are selected if they have

- $R_{\rm shw} \geq 0.10$;
- $|R_{\rm bal}| \leq 0.65$.

For centre-of-mass energies above 172 GeV the selection criteria for $R_{\rm shw}$ and $R_{\rm bal}$ have been modified to:

- $R_{\rm shw} \geq 0.14$;
- $|R_{\rm bal}| \leq 0.75$.

3.2.2 Track and Cluster Quality Cuts

Events passing both the on-line and off-line multihadron selections are studied. In the following analysis chain only charged tracks and calorimeter clusters are considered which satisfy certain quality cuts.

(A) Good Tracks are defined as having all the following properties:

- the number of hits in the jet chamber $N_{\rm CJ\ hits} \geq 20$ and $N_{\rm CJ\ hits} \geq 50\%$ of the maximum possible number of hits at the track polar angle;
- the impact parameter in the $r - \phi$ projection $|d_0| \leq 2.0$ cm;
- the impact parameter in the $s - z$ projection, calculated by constraining the track to the primary vertex in z, $|z_0| \leq 40.0$ cm;
- the momentum transverse to the beam direction $p_{\rm T} \geq 120$ MeV;
- the polar angle $|\cos\theta| \leq 0.9622$;

- the momentum $p < E_{beam} \cdot (1 + 0.03 \cdot \sqrt{16 + 0.09 \cdot E_{beam}^2})$, where E_{beam} is the beam energy.

(B) Good electromagnetic calorimeter clusters are defined as having

- the uncorrected energy of the cluster $E_{\rm raw} \geq 100$ (250) MeV in the barrel (endcap) region;
- the number of blocks in the cluster $N_{\rm blocks} \geq 1$ (2) in the barrel (endcap) region.

(C) Good hadron calorimeter clusters are defined as having the energy measured by the towers $E_{\rm tower} \geq 0.6$ GeV in the barrel and endcap, $E_{\rm tower} \geq 2.0$ GeV in the poletip region.

(D) Good clusters in the forward region are defined as having the energy of the cluster

- $E_{\rm FD} \geq 1.5$ GeV in the forward calorimeter;
- $E_{\rm GC} \geq 5.0$ GeV in the gamma catcher;
- $E_{\rm SW} \geq 0.5$ GeV in the silicon tungsten luminometer.

3.2.3 Energy Correction

The energy flow is calculated using an energy correction algorithm [49] based on geometrical matching of charged particle tracks and electromagnetic (ECAL) and hadronic calorimeter (HCAL) clusters.

This method was invented to prevent *double counting* of the energy of charged particles detected by both the tracking devices and the calorimeters. It also compensates the calorimeter energies for *detector effects*, necessary due to the different energy responses of ECAL and HCAL for hadrons. Hadrons sometimes penetrate ECAL without significant interaction, depositing their full energy in HCAL. However, due to the more than one radiation length material of ECAL, we frequently observe large energy deposited in ECAL not only by electrons and photons but also by hadrons. The lead glass produces an amount of light corresponding to the energy carried by the π^0-s in the hadronic shower produced in ECAL, which is much smaller than the original hadron energy. However, if we add

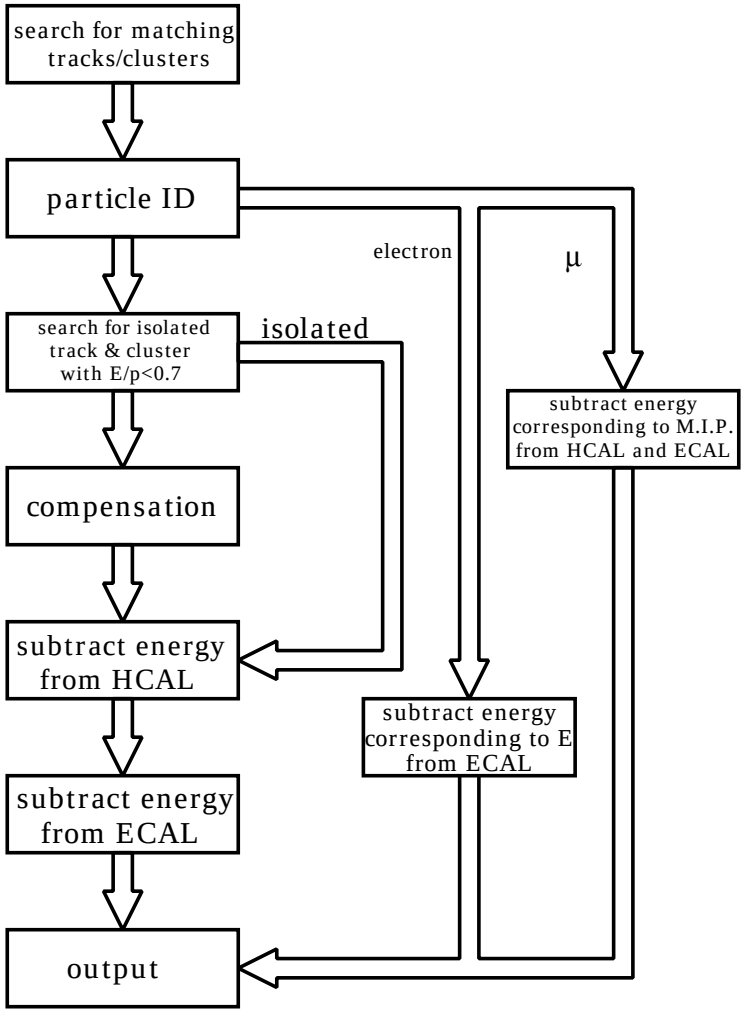

Figure 3.6: *Schematic diagram of the matching algorithm to measure energy flow.*

the observed ECAL and HCAL energies for hadrons, we have a bad resolution due to the different first interaction points of the hadrons. After compensating the ECAL and HCAL energies, an improved energy resolution and correct energy scales are achieved.

In Figure 3.6 the algorithm flow is shown schematically. The method first identifies ECAL and HCAL clusters matching charged tracks, and charged tracks matching ECAL and HCAL clusters, by extrapolating the tracks into the calorimeters. After that electron [50] and muon [47] identification information is used. If the ECAL cluster is identified as deposited by an electron, its energy will not be compensated. If a track is identified as a path of a muon, only the amount corresponding to the deposit by a minimum ionizing

particle is subtracted from the calorimeter energy.

The next step is to look for isolated ECAL clusters with one or two associated tracks and an ECAL energy greater than 70% of the momentum of the associated track(s). If there is an associated HCAL cluster then its energy should be less than 5% of the track momentum. This happens if a photon is converted into an electron-positron pair before reaching ECAL or when an isolated pion interacts with the lead glass and deposits a large amount of its energy before reaching the HCAL. In this case the cluster energies will not be compensated, since for photon conversion the ECAL cluster should be treated as an electromagnetic shower cluster, and for pion interaction the energy should be calculated from the track momenta.

At this stage the algorithm introduces energy compensation for each unidentified cluster with factors depending on the uncorrected energy of the cluster for ECAL, and the energy measured by the towers for HCAL. The compensation factors, ranging between 1.2 and 2.0 for ECAL and between 0.7 and 1.0 for HCAL, are tuned for the case of single pions with various energies incident to the detector.

After this procedure the momentum of the associated track is subtracted from the ECAL and HCAL cluster energy. First, the HCAL tower energy is decreased, and if it is smaller than the track momentum, the ECAL energy is also decreased. The remaining energy of ECAL and HCAL should come from photons or neutral hadrons. The ECAL energy is then corrected using the hypothesis that it was deposited by a photon. At the end, we have three types of quantities: the measured charged particle momenta and the calculated *neutral* ECAL and HCAL cluster energies.

Using this energy correction procedure the visible energy resolution in the barrel region for multihadron events is about 8.6 GeV for the Z^0 data.

3.2.4 Jet Finding

To reconstruct the energy and momentum of quarks, gluons and hadronically decaying tau leptons produced in the main processes of interest, the final state particles observed in the

detector have to be grouped into jets. There are several methods to accomplish this goal, and each method has its definite advantages and disadvantages for any particular purpose. For the reconstruction of quark jets we use the Durham algorithm, which assigns every final state particle to one of the jets, while for hadronic tau decays the cone algorithm is found to be better, which allows for particles not contained in any jet.

Durham Algorithm

To form hadronic jets a transverse momentum minimization algorithm, often referred to as Durham scheme [51], is used. For every pair of final-state objects (k, l) the algorithm first calculates the scaled transverse momentum of the less energetic particle with respect to the more energetic one, defined as

$$y_{kl} = 2\ (1 - \cos\theta_{kl})\ \min(E_k^2, E_l^2)\ /\ E_{\rm vis}^2, \tag{3.1}$$

where E_k and E_l are the energies of the two particles, θ_{kl} is the angle between their momentum vectors and $E_{\rm vis}$ is the total energy of all final-state particles. The two particles (i, j) with the smallest value of y_{ij} are combined together and replaced by a *pseudo-particle* with four-momentum $p_{(ij)} = p_i + p_j$, if their y_{ij} is smaller than a given resolution parameter $y_{\rm cut}$. This procedure is repeated until all pairs of objects (particles and pseudo-particles) have $y_{kl} > y_{\rm cut}$. All objects remaining at this stage are called *jets*.

When a final state is forced into n jets, the value of $y_{\rm cut}$ is gradually decreased from an initial value to get the required number of jets at the end of the procedure. The $y_{\rm cut}$ value at which the number of jets changes from n to $n{+}1$ is usually denoted by the symbol $y_{n\,n+1}$.

Cone Algorithm

While the Durham algorithm described previously works well for hadronic jets, a different method is used to identify τ-jets, since these tend to be narrower. This algorithm [52] corresponds closely to the Snowmass proposal [53].

A *jet* is defined as a set of particles whose momentum vectors lie within a cone of half-angle R. The axis of the cone is the momentum sum of the particles it contains. The total energy of the particles is required to be above some cutoff ϵ. In case of overlaps a special treatment is needed.

First the momentum vector of each particle in the event is taken as the axis of a cone of half-angle R. If the sum of the momenta of all particles within the cone does not coincide with the jet axis, the momentum sum is taken to define a new cone axis, and the process is iterated until a stable solution is found and all the non-identical jets have been found. To allow for narrow jets with small separation to be combined into one, the bisectrix of the angle between each pair of jets is also used as a possible initial cone axis, and the previous iteration is repeated. Jets with energy less than ϵ are rejected.

To resolve overlaps so that each particle is contained no more than one jet, the ratio f of the total energy of the common particles to the smaller jet energy is computed. If $f > 0.75$ the particles in common are assigned to the higher energy jet, and the other is eliminated, while if $f < 0.75$ each overlapping particle is assigned to the jet closest in angle. In case of reassignments the cone axis is not recalculated, but the energy cut is reapplied.

3.2.5 Tau Identification

Charged leptons leave a characteristic signature in the detector. Electrons are stable and muons are sufficiently long-lived particles not to decay in the detector. Both of them can be identified with high efficiency combining tracking and associated calorimeter information [54].

However, tau leptons have short life-time and decay in the detector into final states containing one, three or more charged particles. The number of charged particles in tau decays are counted as *prongs*. The relative weights of the different tau decay modes are listed in Table 3.1.

Two methods are used in this work to identify tau leptons to be described below.

τ^- decay mode	Fraction (%)
1-prong decays	
$e^- \bar{\nu}_e \nu_\tau$	17.8
$\mu^- \bar{\nu}_e \nu_\tau$	17.4
$h^- \nu_\tau X$	49.5
3-prong decays	15.2
5- or more prong decays	0.1

Table 3.1: *Branching ratios of the tau lepton decay modes. In one-prong hadronic decays the symbol* h^- *stands for a charged hadron and* X *for zero or more neutral hadrons.*

Algorithm Based on Electron and Muon Identification and Cone Jet Finding

This method considers separately tau decay modes with charged leptons (electrons or muons) and hadrons in the final state. It is based on electron and muon identification, and seeks for narrow low multiplicity jets isolated from the rest of the event.

The tau candidates have to satisfy one of the following requirements designed to address the different tau decay modes:

- $\boldsymbol{\tau^- \to e^- \bar{\nu}_e \nu_\tau}$: There should be an electron identified by a neural network algorithm [50], but not identified as stemming from a photon conversion [54, 55], with a polar angle $|\cos\theta_e| < 0.97$ and at least 2 GeV momentum. The number of electromagnetic clusters within a cone of 26° half-angle around the electron track has to be less than six, and there should be no hadronic calorimeter cluster with energy greater than 0.6 GeV geometrically associated with the electron track.
- $\boldsymbol{\tau^- \to \mu^- \bar{\nu}_e \nu_\tau}$: There should be a muon, as defined in [47], with polar angle $|\cos\theta_\mu| < 0.97$ and at least 3 GeV momentum. The number of electromagnetic clusters within a cone of 26° half-angle around the muon track has to be less than five.
- $\boldsymbol{\tau^- \to}$ **hadron(s)** $\boldsymbol{\nu_\tau}$: There should be a *tau-jet* with polar angle $|\cos\theta_\tau| < 0.92$ containing one or three tracks, which sum up to unit charge, and have an invariant mass smaller than 3.5 GeV. Tau-jets are defined by the following procedure. First, jets with

at least 3 GeV energy are reconstructed using the cone algorithm with a half-angle of 23°. Within such a jet, the highest energy sub-jet with a half-angle of 11° is considered as the tau-jet.

To define isolation criteria, a 30° half-angle cone is opened around the tau candidate, which is referred as *isolation cone*. The tau candidate has to satisfy the following requirements:

- the ratio of the track momenta within the 11° tau cone to that within the 30° isolation cone should be larger than 0.95;
- the ratio of the electromagnetic cluster energy within the 11° tau cone to that within the 30° isolation cone should be larger than 0.95;
- the cosine of the angle between the tau candidate and the nearest track should be smaller than 0.94.

Track Based Artificial Neural Network Algorithm

The presence of jets degrades tau-tagging performance of conventional algorithms for two reasons. Tau leptons lying near jets may not meet the nominal isolation criterion, thus escaping identification, and fake taus may arise from low multiplicity jets. A tau identification algorithm [56, 57] based on an artificial neural network (ANN) was designed to address these issues. The algorithm is track-based, it seeks to distinguish real tau decay tracks from those arising from the hadronic system, without using information on electron and muon identification. It is intended to exploit the higher momenta and relative isolation from the hadronic system of the real taus as compared to fakes.

The tracks of the event in decreasing order of momentum are classified into three categories:

One-prong candidates Tracks with momentum greater than 2 GeV and no other track within 10°.

Three-prong candidates Tracks with exactly two other tracks within 10°. The sum of the momenta of the *leading* track and its two *sisters* should exceed 2 GeV and the total charge must be ±1.

Non-candidates Tracks which do not fulfil any of the above criteria.

In this classification, tracks consistent with having originated from a photon conversion are excluded [54, 55]. A final requirement is placed on the tau candidates to prevent double- and triple counting of three-prong candidates: none of the tracks used to form the candidate may belong to another candidate found previously in the event. This prefers higher momentum tracks as leading particles.

Two cones are defined around the (leading) track: the *tau cone* has a 10° half-angle, whereas the *isolation cone* has a 30° half-angle and excludes the tau cone.

The one- and three-prong candidates found in an event are passed to separate ANNs (called one-prong and three-prong ANNs) with slightly different input variables:

(A) The inputs of the one-prong ANN are the following:

- the invariant mass of particles (charged tracks and neutral clusters) in the tau cone;
- the total energy of all particles in the tau cone;
- the ratio of the total energy in the isolation cone to the total energy in the tau cone;
- the number of particles with energy greater than 750 MeV in the isolation cone;
- the total energy of all charged tracks in the isolation cone.

(B) The inputs to the three-prong ANN are the following:

- the invariant mass of particles (charged tracks and neutral clusters) in the tau cone;
- the ratio of the total energy in the isolation cone to the total energy in the tau cone;
- the number of particles with energy greater than 750 MeV in the isolation cone;
- the angle between the leading track and the furthest sister track.

Combining the information of these variables the ANN assigns one number from zero to one to each tau candidate. This is expected to be close to one for real tau leptons, while small values indicate fakes.

One of the practical advantages of this method is that the best tau candidate can be easily selected using the value of the ANN output, if there is more than one in the event.

3.2.6 Kinematic Fits

Having identified our final state objects, jets and leptons, we can calculate their energy and momentum as described in Section 3.2.3. These quantities, however, do not contain all available information. A way to include requirements prescribed by physics considerations, like conservation laws, is the application of kinematic fits. Kinematic fits can also help decide whether a hypothesis, like the production of equal mass particles, is favoured by our experimental data or not.

The parameters are estimated using constrained least-squares fitting, based on the method of [58]. To assess the goodness of the fit one can construct a quantity depending on the χ^2 of the fit and the degrees of freedom, usually called χ^2 *probability*, which is expected to have a uniform distribution between zero and one for events satisfying the prescribed physics hypothesis.

In this work the input variables are usually $\log|p|, \theta$ and ϕ, where p is the momentum, θ is the polar and ϕ is the azimuthal angle of the jets. They are considered to be uncorrelated and their errors have been parametrized [59] as

$$\delta(\log|p|) = \alpha^{0.5}\left(\frac{1}{\sin^2\theta}\right)\cdot\beta\left(\frac{1}{|p|}\right), \tag{3.2}$$

$$\delta(\theta) = \alpha^{0.5}\left(\frac{1}{\sin^2\theta}\right)\cdot\gamma\left(\left(\frac{M_j}{E_j^{1.2}}\right)^2\right), \tag{3.3}$$

$$\delta(\theta) = \alpha^{0.5}\left(\frac{1}{\sin^2\theta}\right)\cdot\gamma'\left(\left(\frac{M_j}{E_j^{1.2}}\right)^2\right), \tag{3.4}$$

where M_j is the mass and E_j is the energy of the jet. The functions α, β, γ and γ' are linear functions of their arguments, with parameters determined from Monte Carlo studies.

The errors are larger for forward jets, where the tracking information is less accurate and particles may escape detection. The dependence on the jet momentum is small but non-negligible. The resolution of the direction measurement depends on the broadness of the jet, which can be approximated by the jet mass.

3.2.7 Event Variables

To describe the complicated geometries encountered in multihadronic events, a number of variables have been introduced. They intend to provide a global view of the properties of a given event, condensing the relevant information into a few numbers. After defining the effective centre-of-mass energy related to the radiative nature of multihadron events in e^+e^- collisions above the Z^0 peak, we list some of these event shape variables used in this work.

Effective Centre-of-mass Energy

The effective centre-of-mass energy, $\sqrt{s'}$, of the e^+e^- collision after initial state photon radiation, is estimated for each event by finding a possible initial state photon in two ways.

First, an initial state photon is searched for directly in the electromagnetic calorimeter. It is identified by requiring it to conform to the expected transverse shower shape and to be isolated by observing no more than 1 GeV energy in a cone of 400 mrad half-angle around it. A veto against hadron calorimeter cluster with energy greater than 4 GeV associated to the electromagnetic calorimeter cluster of the photon is applied in the polar angle range of $|\cos\theta| < 0.955$.

Then, the Durham jet finding scheme is used to force the particles into two jets. The energy of a possible undetected initial state photon is estimated by performing a kinematic fit to the system of jets and an unmeasured photon along the beam direction using the measured energy and momentum and imposing the constraints of energy and momentum conservation.

The photon energy, E_γ, is the larger of the one derived from the kinematic fit and the one found in the calorimeter. We compute

$$s' = s - 2E_\gamma\sqrt{s}. \tag{3.5}$$

The typical resolution on $\sqrt{s'}$ is ~ 3 GeV.

Thrust

The thrust value T is used to select or reject two-jet events. It is defined by

$$T = \max_{|\vec{n}|=1} \frac{\sum_i |\vec{n} \cdot \vec{p}_i|}{\sum_i |\vec{p}_i|}, \tag{3.6}$$

where the sum goes over all the particles and $\vec{p}_i$ denotes the three-momentum of the particles. The thrust axis is given by the $\vec{n}$ vector for which the maximum is attained. The allowed range is $0.5 \leq T \leq 1$, with $T \approx 1$ for two-jet events and $T \approx 0.5$ for isotropic events.

Sometimes it is useful to calculate thrust for only a part of the event, for example for individual jets. In this case it is called *jet thrust*.

Aplanarity

The aplanarity [60] measures the transverse momentum component out of the event plane and is used to identify planar events. It is defined as

$$A = \frac{3}{2}\lambda_3, \tag{3.7}$$

where λ_3 is the smallest eigenvalue, with $\lambda_1 + \lambda_2 + \lambda_3 = 1$, of the sphericity tensor

$$S^{\alpha\beta} = \frac{\sum_i p_i^\alpha p_i^\beta}{\sum_i |\vec{p}_i|^2}, \tag{3.8}$$

where $\alpha, \beta = 1, 2, 3$ corresponds to the x, y, z components. The aplanarity is constrained to the range $0 \leq A \leq 0.5$, having $A \sim 0$ for planar and $A \sim 0.5$ for isotropic events.

C and *D* Parameters

The sphericity tensor is quadratic in particle momenta and not an infrared safe quantity in perturbation theory. A useful generalization of the sphericity tensor is

$$S^{(1)\alpha\beta} = \frac{\sum_i \frac{p_i^\alpha p_i^\beta}{|\vec{p}_i|}}{\sum_i |\vec{p}_i|}. \tag{3.9}$$

The parameters C and D [60] are used to measure the three- or four-jet like topology of the event and are defined as

$$C = 3(\lambda_1\lambda_2 + \lambda_1\lambda_3 + \lambda_2\lambda_3), \quad (3.10)$$

$$D = 27\lambda_1\lambda_2\lambda_3, \quad (3.11)$$

where λ_i $(i = 1, 2, 3)$ are the eigenvalues of the generalized sphericity tensor $S^{(1)\alpha\beta}$, with $\lambda_1 + \lambda_2 + \lambda_3 = 1$. Both parameters are constrained in the range between zero and one. C is vanishing for a perfect two-jet event and D is vanishing for a planar event.

3.2.8 Likelihood Method for Event Selection

Extracting a specific process (signal) from a data sample which also contains a large fraction of events coming from other processes (background) is a standard task in high energy physics. Traditionally, a set of variables which discriminate sufficiently between signal and background is selected and a cut is applied on each of these variables, enhancing the fraction of signal events. In this simple solution, not all the available information is taken into account. We always make a yes-or-no decision taking the variables one by one, without considering how close these variables are to the cut values. To take advantage of the information we can get by considering more than one variable at the same time, several methods have been developed[3]. One of them is the likelihood method, which is used as a final selection in several analyses described in the next chapters. This accounts for the probabilistic nature of the observed distributions of event properties in a plausible way.

Let us consider N_{class} different classes of events corresponding to different physics processes and N_{var} experimental variables for each event. Each variable i for each class j is distributed according to a characteristic probability density function $f_i^j(x_i)$, where x_i is the measured value of variable i in an individual event.

[3]The choice of artificial neural networks to combine information of several (usually correlated) variables has become also popular. We also apply such networks when using, for example, lepton identification information.

If each event belongs to exactly one of the $N_{\rm class}$ classes, for a single variable the probability that an event belongs to class j is given by

$$p_i^j(x_i) = \frac{f_i^j(x_i)}{\sum_{j=1}^{N_{\rm class}} f_i^j(x_i)} \tag{3.12}$$

To combine the information from several variables one forms for each class the likelihood function as the normalized product of $p_i^j(x_i)$

$$\mathcal{L}^j(\vec{x}) = \frac{\prod_{i=1}^{N_{\rm var}} p_i^j(x_i)}{\sum_{j=1}^{N_{\rm class}} \prod_{i=1}^{N_{\rm var}} p_i^j(x_i)}, \tag{3.13}$$

where $\vec{x}$ denotes the event vector, consisting of all measured x_i. $\mathcal{L}^j(\vec{x})$ takes on values between zero and one, and it can be used to classify an event to belong to class j by requiring that its likelihood $\mathcal{L}^j(\vec{x})$ is larger than some cut value $P^j_{\rm cut}$. Varying $P^j_{\rm cut}$ one can optimize the efficiency vs. purity for the selected sample of class j.

Technically, the probability density functions are sampled by fully simulated Monte Carlo events for the different event classes and stored in histograms, which are called reference histograms. Three different event classes are defined reflecting the fact that we are looking for a new physics process (signal) with an experimental background composed of SM two- and four-fermion processes, as explained in Section 3.1:

(1) signal;

(2) two-fermion processes;

(3) four-fermion processes.

Although in principle it would be sufficient to discriminate only between two classes (signal and background), it is sensible to accommodate for the different properties of two- and four-fermion events by separating them into different classes.

3.2.9 Statistical Methods for Limit Calculation

Searches for new particles are intended to distinguish between two hypotheses: the production and detection of signal along with SM background processes and the presence of only SM background. In the absence of discovery, it means setting upper limits on signal event rates.

Deriving Upper Limits

Traditionally the confidence level for the presence of signal and background together is the probability that the search would have missed the signal by as much or more than the actual outcome of the search. To define this mathematically one should introduce an estimator X, a function of the observed event counts and the expected signal and background rates, to separate signal-like and background-like events. Then the probability of the presence of both signal and background is

$$CL_{\mathrm{s+b}} = \mathcal{P}_{\mathrm{s+b}}(X \leq X_{\mathrm{obs}}) \tag{3.14}$$

and the probability of the presence of only background is

$$CL_{\mathrm{b}} = \mathcal{P}_{\mathrm{b}}(X \leq X_{\mathrm{obs}}), \tag{3.15}$$

where X_{obs} is the value of the estimator calculated using the measured event count. The ratio of these probabilities

$$CL = 1 - CL_{\mathrm{s}} = 1 - \frac{CL_{\mathrm{s+b}}}{CL_{\mathrm{b}}}. \tag{3.16}$$

is commonly used to set limits and gives the basis of the confidence level formula found in [61]:

$$CL = 1 - \frac{e^{-(B+N)} \sum_{n=0}^{n_0} \frac{(\mu_B+N)^n}{n!}}{e^{-B} \sum_{n=0}^{n_0} \frac{B^n}{n!}}. \tag{3.17}$$

Here a Poisson process with an unknown mean of the signal s is considered, in the presence of a known background with mean B. n_0 is the total number of signal and background events observed. N is the value of s, for which any random repeat of the current experiment with $s = N$ and the same B would observe more than n_0 events in total and have $n_B \leq n_0$ actual number of background events, all with a probability of CL.

This is further complicated by taking into account the systematic error on the experimental sensitivity, as described by [62]. Let N_{CL} be the upper limit on s at a given confidence level. Including the relative systematic uncertainty σ on the sensitivity in the lowest order one gets

$$\Delta N_{CL} = \frac{N_{CL} + B - n_0}{N_{CL} + B} \cdot \frac{N_{CL}^2 \cdot \sigma^2}{2}. \tag{3.18}$$

The incorporation of the error on the background estimate has to be done numerically using an iterative algorithm, due to the complex dependence of Equation 3.17 on B.

Statistical Combination of Individual Search Channels

If searches for new particles are performed in different decay channels and/or at various centre-of-mass energies and none of them reveals any significant signal, the negative result of the individual search channels can be statistically combined to increase the sensitivity. A statistical method [63], based on *fractional event counting*, is used for that purpose.

The method assigns a weight to each candidate event for a given hypothetical mass m (test mass). The sum of the weights for all candidates is related to the probability to be consistent with the hypothesis of the presence of signal and background together and the hypothesis of the presence of only background in an analytical manner. The probabilities for the signal-plus-background and background-only hypotheses are related in turn to a confidence level as defined in Equation 3.16.

The weight, $w_{ij}(m)$, for each candidate j of each search channel i at the test mass m is determined by the product of two variables described below. One of them is a channel scaling factor, $c_i(m)$, and the other is a factor, $f_i(m, m_{ij})$, corresponding to the expected experimental mass distribution of a particle with mass m, evaluated at the candidate mass, m_{ij}.

The channel scaling factors c_i are determined by the signal-to-background ratio:

$$c_i(m) = \left(\delta + \frac{B_i(m) \cdot s(m)}{S_i^{\max}(m) \cdot s_i(m)} \right)^{-1} . \tag{3.19}$$

Here, the expected number of signal events in channel i, $s_i(m)$, is calculated using the model prediction for the cross-section and branching ratio, the integrated luminosity of the data set to which the search is applied[4], and the signal selection efficiency. The total expected signal rate is $s(m) = \sum_i s_i(m)$. $S_i^{\max}(m)$ is the maximum of the signal probability density, $S_i(m, m_{ij})$, for any possible m_{ij}. The function $B_i(m)$ is the expected differential background rate per GeV for test mass m. For channels where the mass is reconstructed,

[4]Identical search channels using different data sets are considered as individual channels.

$S_i^{\max}(m)$ is inversely proportional to the mass resolution. For channels without mass reconstruction, the ratio $B_i(m)/S_i^{\max}(m)$ is replaced by the total background rate. This implies that the c_i are larger for channels where the mass is reconstructed. δ is a free parameter. It can be adjusted to a specific physical situation with Monte Carlo studies by minimizing the average confidence levels arising entirely from background with the signal simulation switched off.

The factor $f_i(m, m_{ij})$ is given by the ratio

$$f_i(m, m_{ij}) = \frac{S_i(m, m_{ij})}{S_i^{\max}(m)}. \tag{3.20}$$

The overall event weight for each candidate is thus given by:

$$w_{ij}(m) = K \cdot c_i(m) \cdot f_i(m, m_{ij}). \tag{3.21}$$

The factor K is a normalization constant that fixes the largest value of $w_{ij}(m)$ to unity.

The sum of all candidate weights over all channels $w(m) = \sum_{i,j} w_{ij}(m)$ is converted to a confidence level $CL(m)$ [63] for this sum to be more likely due to signal-plus-background than due to background-only.

This method is used to combine the search channels and derive limits for charged Higgs boson production in Section 4.5. The observed events are considered as signal plus background, and to take into account the error on the background estimate a conservative, but simple and fast approach is chosen: the background is reduced by its systematic error. In calculating c_i the best estimate of the background is always taken. The uncertainty on the signal selection efficiency is accounted for using Equation 3.18.

Chapter 4

Search for Charged Higgs bosons

4.1 Introduction

Charged Higgs bosons are predicted by various extensions of the SM. Their discovery would be a clear indication of a non-minimal Higgs sector. Several collaborations have conducted direct or indirect searches for charged Higgs bosons, but no evidence of their presence has been reported so far.

The OPAL Collaboration has performed a direct search in the LEP1 data and published a lower limit on the charged Higgs boson mass of $m_{\mathrm{H}^{\pm}} > 44.1$ GeV at the 95% CL [64] in the framework of two-Higgs-doublet models (2HDM). The other LEP collaborations have also searched for charged Higgs bosons and established bounds on their mass [65, 66, 67, 68].

From a measurement of the Michel parameters in leptonic tau decays OPAL has obtained a lower limit of $m_{\mathrm{H}^{\pm}} > 0.97$ GeV $\times \tan\beta$, where $\tan\beta$ is the ratio of the vacuum expectation values of the two Higgs field doublets, at the 95% CL in 2HDMs assuming only left-handed neutrinos with vanishing mass [69]. The ALEPH, CLEO, CDF and D0 Collaborations have also set limits on the mass of the charged Higgs bosons as a function of $\tan\beta$ with certain model assumptions [70, 71, 72, 73].

In $\mathrm{e}^{+}\mathrm{e}^{-}$ collisions at LEP charged Higgs bosons can be pair-produced in s-channel γ and Z^{0} exchange processes as shown in Figure 4.1. In 2HDMs the production cross-section

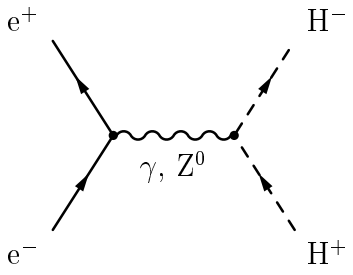

Figure 4.1: *Feynman diagram for charged Higgs boson pair-production.*

depends only on the charged Higgs boson mass and known parameters [74]:

$$\sigma_{\mathrm{H^+H^-}} = \frac{2G_F^2 m_{\mathrm{W}^\pm}^4 \sin^4\theta_W}{3\pi s}\left[1 - \frac{2\hat{v}_e\hat{v}_H}{1-\frac{m_{\mathrm{Z}^0}^2}{s}} + \frac{(\hat{a}_e^2+\hat{v}_e^2)\hat{v}_H^2}{\left(1-\frac{m_{\mathrm{Z}^0}^2}{s}\right)^2}\right]\beta_H^3 \tag{4.1}$$

with

$$\hat{a}_e = \frac{-1}{4\cos\theta_W\sin\theta_W}, \quad \hat{v}_e = \frac{-1+4\sin^2\theta_W}{4\cos\theta_W\sin\theta_W}, \quad \hat{v}_H = \frac{-1+2\sin^2\theta_W}{2\cos\theta_W\sin\theta_W}, \tag{4.2}$$

where m_{Z^0} is the Z^0 boson mass, $m_{\mathrm{W}^\pm}$ is the $\mathrm{W}^\pm$ boson mass, θ_W is the Weinberg angle, G_F is the Fermi coupling constant and $\sqrt{s}$ is the centre-of-mass energy. The velocity of the Higgs boson with mass $m_{\mathrm{H}^\pm}$ is

$$\beta_H = \left(1 - \frac{4m_{\mathrm{H}^\pm}^2}{s}\right)^{0.5}. \tag{4.3}$$

The angular distribution follows the $\sin^2\theta$ law

$$\frac{1}{\sigma}\cdot\frac{\mathrm{d}\sigma}{\mathrm{d}\cos\theta} = \frac{3}{4}\sin^2\theta, \tag{4.4}$$

typical for spin-0 particle production. Here θ is the angle between the incident electron and the produced Higgs boson.

The decay of charged Higgs bosons (Figure 4.2) is model dependent [74, 75]. At LEP energies H^+ decays into fermion pairs, dominantly $\mathrm{c\bar{s}}$, $\mathrm{c\bar{b}}$ and $\tau^+\nu_\tau$, or into $\mathrm{A}^0\mathrm{W}^{+*}$ and $\mathrm{h}^0\mathrm{W}^{+*}$, if the neutral Higgs bosons are sufficiently light. In this work we consider only

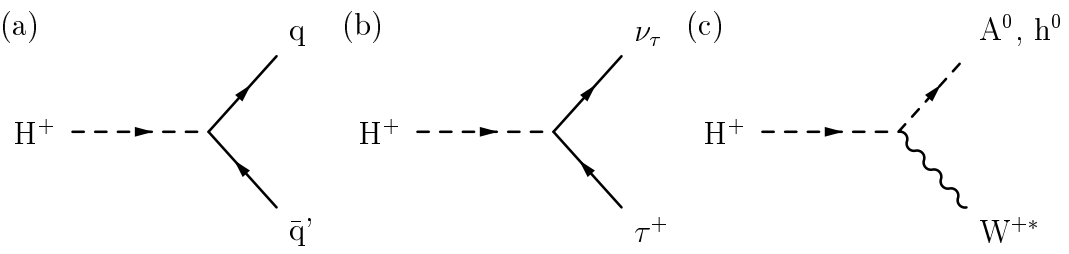

Figure 4.2: *Feynman diagrams for charged Higgs boson decays into (a) a quark pair, (b) a $\tau^+\nu_\tau$ pair and (c) a neutral Higgs boson together with a $W^\pm$ boson.*

charged Higgs boson decays into fermion pairs, $H^+ \to q\bar{q}'$ and $H^+ \to \tau^+\nu_\tau$, assuming that the decays into non-SM particles are suppressed.

With this assumption three final states with highly different event topologies should be considered:

leptonic $H^+H^- \to \tau^+\nu_\tau\tau^-\bar{\nu}_\tau$,
semi-leptonic $H^+H^- \to \tau^+\nu_\tau q\bar{q}'$ or the charged conjugate,
hadronic $H^+H^- \to q\bar{q}'q''\bar{q}'''$.

In the following we present the analyses [57, 76, 77] of the hadronic final state containing four well-separated hadronic jets, and the semi-leptonic final state consisting of two hadronic jets, a tau lepton and sizable missing energy and momentum. Our results are combined with the result of the analysis of the leptonic channel [78] and used to derive 95% CL lower limits on the mass of the charged Higgs bosons, assuming $BR(H^+ \to \tau^+\nu_\tau) + BR(H^+ \to q\bar{q}) = 1$ for the branching ratios and including the information from our LEP1 data [64], as well.

4.2 Data and Monte Carlo Simulation

Data collected by the OPAL detector between 1995 and 1998 at centre-of-mass energies of $130 - 189$ GeV, summarized in Table 4.1, are used to search for charged Higgs boson production.

$\sqrt{s}$ (GeV)	Year	$\int \mathcal{L}$ (pb^{-1})
130.3	1995	2.3
136.2	1995	2.6
161.3	1996	10.0
172.1	1996	10.4
182.7	1997	56.2
188.6	1998	179.1

Table 4.1: *Charged Higgs boson search: Summary of data samples. Luminosity weighted averages of centre-of-mass energies, years of collection and integrated luminosities.*

The main background for all selections described here comes from quark pair events with or without initial state photon radiation and from four-fermion production processes, predominantly W^+W^- production. We have used the Standard Model Monte Carlo samples described in Section 3.1.

Signal selection efficiencies are estimated using the PYTHIA generator at $\sqrt{s} = 161 - 172$ GeV and the HZHA generator at $\sqrt{s} = 130 - 136$ and $183 - 189$ GeV to simulate the production of charged Higgs bosons, $e^+e^- \to H^+H^-$, followed by the decays $H^+ \to c\bar{s}$ or $\tau^+\nu_\tau$. Samples with Higgs boson masses from 40 to 60 GeV at $\sqrt{s} = 130$ and 136 GeV, from 40 to 70 at $\sqrt{s} = 161$ GeV, from 40 to 75 at $\sqrt{s} = 172$ GeV and from 50 to 90 at $\sqrt{s} = 183$ and 189 GeV are generated in 5 GeV steps. Samples with the decay $H^+ \to c\bar{b}$ are also generated at $\sqrt{s} = 161$ GeV with a mass of 55 GeV, at $\sqrt{s} = 172$ GeV with masses of 50 and 55 GeV and at $\sqrt{s} = 189$ GeV with masses of 65 and 75 GeV, to check for flavour dependence.

4.3 Semi-Leptonic Final State

The semi-leptonic channel $H^+H^- \to \tau^+\nu_\tau q\bar{q}'$ is characterized by an isolated tau lepton, a pair of jets and sizable missing energy and momentum. The main background comes from the $W^+W^- \to \ell^+\nu_\ell q\bar{q}'$ process with a significant contribution from $q\bar{q}(\gamma)$ processes at lower

centre-of-mass energies.

The search has two key points: the rejection of the two-fermion and two-photon events, where the missing energy usually points into the beam direction and there is no real isolated tau lepton in the event; and the separation of the W^+W^- background from the signal. The latter is the more difficult task, considering that W^+W^- events have similar topology to the signal, particularly if the charged Higgs boson mass is close to the $W^\pm$ mass.

Tau identification plays a crucial role in recognizing the signal topology. The analyses at $\sqrt{s} = 130 - 172$ GeV and $\sqrt{s} = 183 - 189$ GeV use different algorithms, which also imply different philosophies for technical reasons. At lower energies a tight tau identification is applied at the very beginning of the analysis flow, while at $\sqrt{s} = 183 - 189$ GeV only a loose tau selection is necessary, just before the final stage, where the information on the tau candidate is combined with other variables using a likelihood technique.

4.3.1 Analysis of Data Collected at $\sqrt{s} = 130 - 172$ GeV

(1) The event must pass the off-line multihadron selection described in Section 3.2.1.

(2) There must be at least one isolated tau lepton identified using an algorithm based on electron and muon identification and cone jet finding as described in the first part of Section 3.2.5. The flight direction of the tau lepton is approximated by the direction of the momentum vector of its visible decay products. If there is more than one tau lepton in the event and only one decays leptonically, that one is kept, otherwise the one with the largest $R^{11/30}$ is retained, where $R^{11/30}$ stands for the ratio of the sum of the track momenta within an 11° half-angle cone relative to that within a 30° half-angle cone around the direction of the tau lepton.

(3) Most of the two-photon and radiative two-fermion events are eliminated by requiring that the polar angle of the missing momentum satisfies $|\cos\theta_{\rm miss}| < 0.9$.

(4) To further suppress two-fermion background with initial state radiation, events with an energetic photon, identified as an electromagnetic cluster with energy greater than 15 GeV that has no track within a 30° half-angle cone around the cluster axis, are

rejected.

Two-fermion background with no sizable missing momentum and energy is reduced by the following requirements:

(5) The visible invariant mass of the event, $M_{\rm vis} = \sqrt{E_{\rm vis}^2 - \vec{P}_{\rm vis}^2}$ has to be smaller than $0.8\,\sqrt{s}$.

The total missing momentum transverse to the beam direction should be larger than $0.13\,\sqrt{s}$.

The aplanarity must exceed 0.005.

At centre-of-mass energies of $161 - 172$ GeV the rejection of four-fermion background, mainly from $\mathrm{W^+W^-}$ production with one $\mathrm{W^\pm}$ decaying leptonically, is explicitly addressed:

(6) There should be no track in the event with momentum larger than $0.25\sqrt{s}$.

The cosine of the jet-jet angle in the hadronic system must exceed -0.65 and -0.55 at $\sqrt{s} = 161$ and 172 GeV, respectively. The two jets of the hadronic system are defined using the Durham jet-finding algorithm after removing the decay products of the tau lepton.

Table 4.2 shows the number of selected data events, the total expected background and the signal efficiency for $m_{\rm H^\pm} = 50$ GeV after each cut at all four centre-of-mass energies. The agreement between data and background simulation is good. After all requirements no event is selected in the data sample, while 2.7 ± 0.2 (statistical error) events are expected from SM processes. Of these, the four-fermion processes account for $13.3\pm3.0\%$, $65.8\pm7.0\%$ and $90.5\pm5.4\%$ at $\sqrt{s} = 130 - 136$, 161 and 172 GeV, respectively. The efficiencies are listed in Table 4.3 for several Higgs boson masses. The drop in efficiency at high masses is due to cut (6).

The Higgs boson mass can be reconstructed from the hadronic system with $2 - 3$ GeV resolution scaling the dijet invariant mass by the ratio of the beam energy to the total energy of the two jets. This simple correction improves the mass resolution by almost a factor of two and at the same time shifts the mass of the $\mathrm{W^\pm}$ bosons towards its nominal

	130 GeV			136 GeV		
Cut	Data	Background	Efficiency (%)	Data	Background	Efficiency (%)
(1)	736	728.8±3.2	99.0±0.4	688	689.0±3.2	97.8±0.7
(2)	53	51.3±1.3	61.0±2.2	56	47.2±1.3	57.2±2.2
(3)	28	25.0±0.8	57.8±2.2	25	22.4±0.7	54.8±2.2
(4)	26	21.5±0.7	57.4±2.2	24	19.0±0.7	54.8±2.2
(5)	0	0.5±0.1	40.4±2.2	0	0.2±0.1	42.4±2.2
	161 GeV			172 GeV		
Cut	Data	Background	Efficiency (%)	Data	Background	Efficiency (%)
(1)	1509	1464.5±3.1	98.6±0.5	1394	1294.6±2.2	98.2±0.6
(2)	126	110.6±1.4	67.4±2.1	131	116.3±1.1	67.6±2.1
(3)	46	48.8±0.7	65.2±2.1	63	64.4±0.7	65.8±2.1
(4)	41	42.9±0.7	64.8±2.1	58	59.8±0.6	64.8±2.1
(5)	2	4.1±0.1	50.2±2.2	12	15.4±0.2	44.8±2.2
(6)	0	0.7±0.1	48.2±2.2	0	1.3±0.1	44.2±2.2

Table 4.2: H^+H^- *search, semi-leptonic channel at* $\sqrt{s} = 130 - 172$ *GeV: Numbers of selected data and expected background events together with the selection efficiencies for a simulated signal of 50 GeV mass after each cut. Errors are statistical only.*

$\sqrt{s}$	Signal selection efficiencies (%) for $m_{H^\pm}$							
(GeV)	40 GeV	45 GeV	50 GeV	55 GeV	60 GeV	65 GeV	70 GeV	75 GeV
130	37.0±2.2	42.4±2.2	40.4±2.2	35.0±2.1	27.6±2.0	—	—	—
136	37.0±2.2	45.6±2.2	42.4±2.2	38.6±2.2	35.0±2.1	—	—	—
161	42.6±2.2	46.0±2.2	48.2±2.2	43.0±2.2	35.0±2.1	31.0±2.1	26.8±2.0	—
172	41.8±2.2	43.2±2.2	44.2±2.2	42.2±2.2	37.0±2.2	35.8±2.1	29.8±2.0	12.2±1.5

Table 4.3: H^+H^- *search, semi-leptonic channel at* $\sqrt{s} = 130 - 172$ *GeV: Signal selection efficiencies for various charged Higgs boson masses. Errors are statistical only. Dashes indicate masses which are not simulated.*

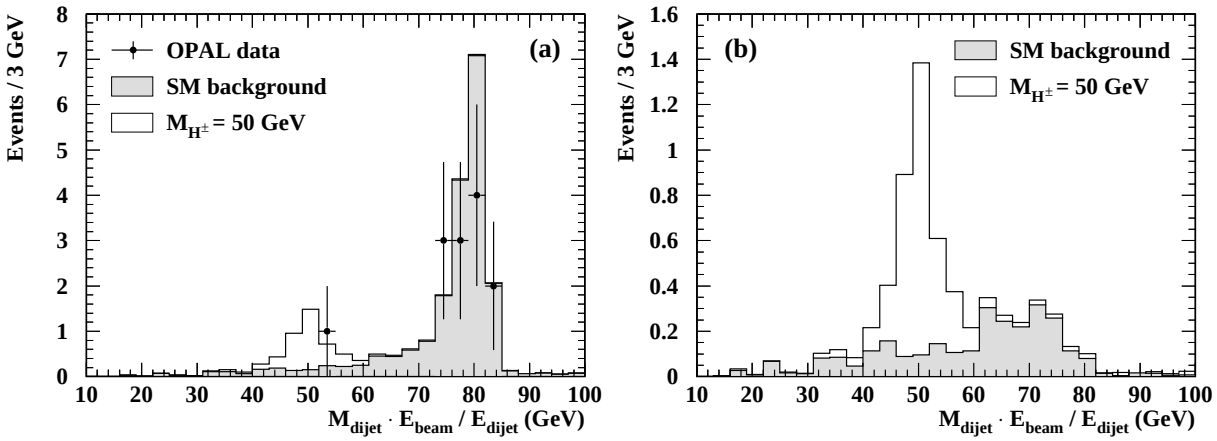

Figure 4.3: H^+H^- *search, semi-leptonic channel at* $\sqrt{s} = 130 - 172$ *GeV: Scaled invariant mass distribution (a) before and (b) after cut (6). Selected data events are shown as dots with error bars, the SM background estimates as shaded histograms and a simulated signal of 50 GeV mass as open histograms on top of the SM background. All Monte Carlo samples are normalized to the integrated luminosity of the data. For the signal* $\mathrm{BR}(H^+ \to \tau^+\nu_\tau) = 0.5$ *is assumed.*

value, thereby decreasing the expected background in the mass range below 65 GeV. The mass distributions are shown in Figure 4.3 before and after cut (6) for the selected events and the expected background together with a signal of $m_{H^\pm} = 50$ GeV.

4.3.2 Analysis of Data Collected at $\sqrt{s} = 183 - 189$ GeV

At $\sqrt{s} = 183 - 189$ GeV several new methods have been introduced: a tau identification algorithm using artificial neural networks, a multidimensional method to exploit the fine differences between the signal and the severe W^+W^- background, and a constrained kinematic fit for better mass reconstruction.

The analysis proceeds in two steps. Events consistent with the final state topology are preselected and then categorized by combining the information of several variables using the likelihood method.

(1) The event must pass the off-line multihadron selection described in Section 3.2.1

(2) Significant missing energy, $E_{\mathrm{vis}}/\sqrt{s} < 0.85$, should be present to account for the unde-

tected neutrinos.

Radiative two-fermion and two-photon backgrounds are suppressed by the following requirements:

(3) The total missing momentum transverse to the beam direction has to be larger than 10 GeV.

The polar angle of the missing momentum is required to satisfy $|\cos\theta_{\rm miss}| < 0.9$.

The sum of the energies in the forward detector, the gamma catcher[1] and silicon-tungsten luminometer is required to be less than 20 GeV.

Two additional conditions are prescribed to select events with the final state signal topology:

(4) There must be at least one tau lepton identified by the track-based ANN algorithm described in the second part of Section 3.2.5, with output larger than 0.5. If there is more than one tau lepton candidate in the event, the one with the largest ANN output is retained.

(5) The hadronic system, defined as the remainder of the event after removing the decay products of the tau lepton, is forced into two jets by the Durham algorithm. Both hadronic jets should contain at least one charged track.

Some of the cut variables are shown in Figure 4.4 at $\sqrt{s} = 183$ GeV. In the early stages of the selection an excess of events is observed due to a shift of the visible energy in the data toward lower values.

All surviving events enter the likelihood selection, which uses 12 input variables. Three event classes are defined: two-fermion events, four-fermion events and $H^+H^- \to \tau^+\nu_\tau q\bar{q}'$. The signal reference histograms are produced adding charged Higgs boson samples with masses of $50 - 90$ GeV at $\sqrt{s} = 183$ GeV and $60 - 80$ GeV at $\sqrt{s} = 189$ GeV. The input variables are:

- the total missing momentum transverse to the beam direction;

[1] Due to hardware problems the gamma catcher is not used at $\sqrt{s} = 189$ GeV.

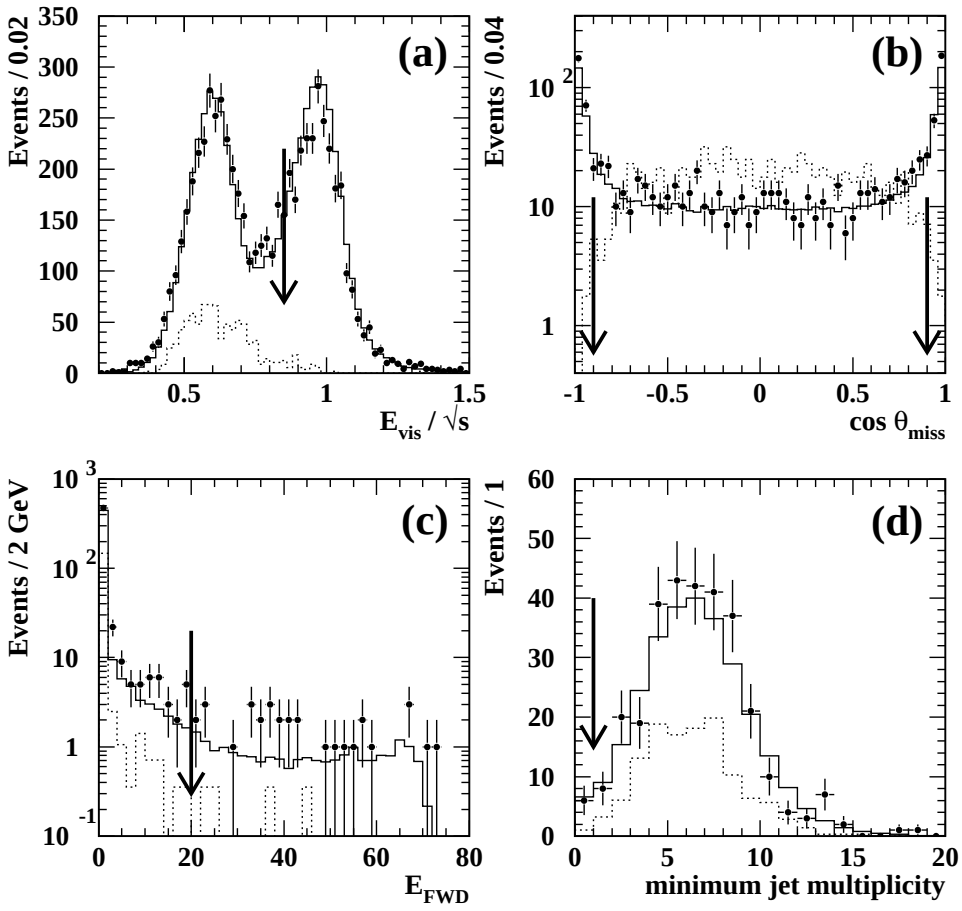

Figure 4.4: H^+H^- *search, semi-leptonic channel at* $\sqrt{s} = 183$ *GeV: Distributions of preselection variables: (a) visible energy, (b) cosine of the polar angle of the missing momentum, (c) total energy measured in the forward detector, gamma catcher and silicon tungsten calorimeter and (d) smallest number of charged tracks in the hadronic jets. Selected data events are shown as dots with error bars, the SM background estimates as solid histograms and a simulated signal of 65 GeV mass as dotted histograms. All Monte Carlo samples are normalized to the integrated luminosity of the data. For the signal* $BR(H^+ \to \tau^+\nu_\tau) = 0.5$ *is assumed and the distributions are scaled up by a factor of 100 (a,b) and 20 (c, d) for better visibility. The arrows indicate the cut positions.*

- the scalar sum of the charged track momenta;
- the number of charged tracks in a 30° cone around the tau direction, excluding the tracks within the 10° tau cone;
- the cosine of the angle between the tau and the nearest jet, $\cos\theta_{\rm nearest}$;
- the tau lepton ANN output;
- the number of charged tracks within the 10° tau cone;
- the highest track momentum, $p_{\rm max}$;
- the highest electromagnetic cluster energy;
- the polar angle of the hadronic system multiplied by the sign opposite to the tau lepton charge, $-Q_\tau \cos\theta_{\rm hadr}$;
- the polar angle of the tau lepton in the rest-frame of the hadronic system multiplied by the sign of the tau lepton charge, $Q_\tau \cos\theta^*_\tau$;
- the C event shape parameter;
- the Durham scheme jet resolution parameter $y_{12}^{\rm hadr}$ of the hadronic system.

(8) As a final selection, events are selected if their likelihood output is greater than 0.85.

Figure 4.5 shows the distributions of six likelihood input variables at $\sqrt{s}$ = 189 GeV. The resulting likelihood distribution is shown in Figure 4.6. Table 4.4 shows the number of selected data events, the expected background and the signal efficiency for $m_{\rm H^\pm}$ = 60 GeV and 65 GeV at $\sqrt{s}$ = 183 and 189 GeV, respectively, after each cut. After all requirements, 71 events are selected in the data sample, while 75.4 ± 2.5 (statistical error) events are expected from SM processes. The four-fermion processes account for 98% and 99% at $\sqrt{s}$ = 183 and 189 GeV, respectively. The signal selection efficiencies are listed in Table 4.5. The efficiency decreases with increasing Higgs boson mass, since the signal and the $\rm W^+W^-$ background become increasingly similar.

The Higgs boson mass is reconstructed with 2.0 − 2.5 GeV resolution using a kinematic fit that requires energy and momentum conservation and the decay of two equal mass objects. Before entering the kinematic fit it is assumed that the tau lepton direction is given by the direction of the visible decay products associated with the tau lepton and

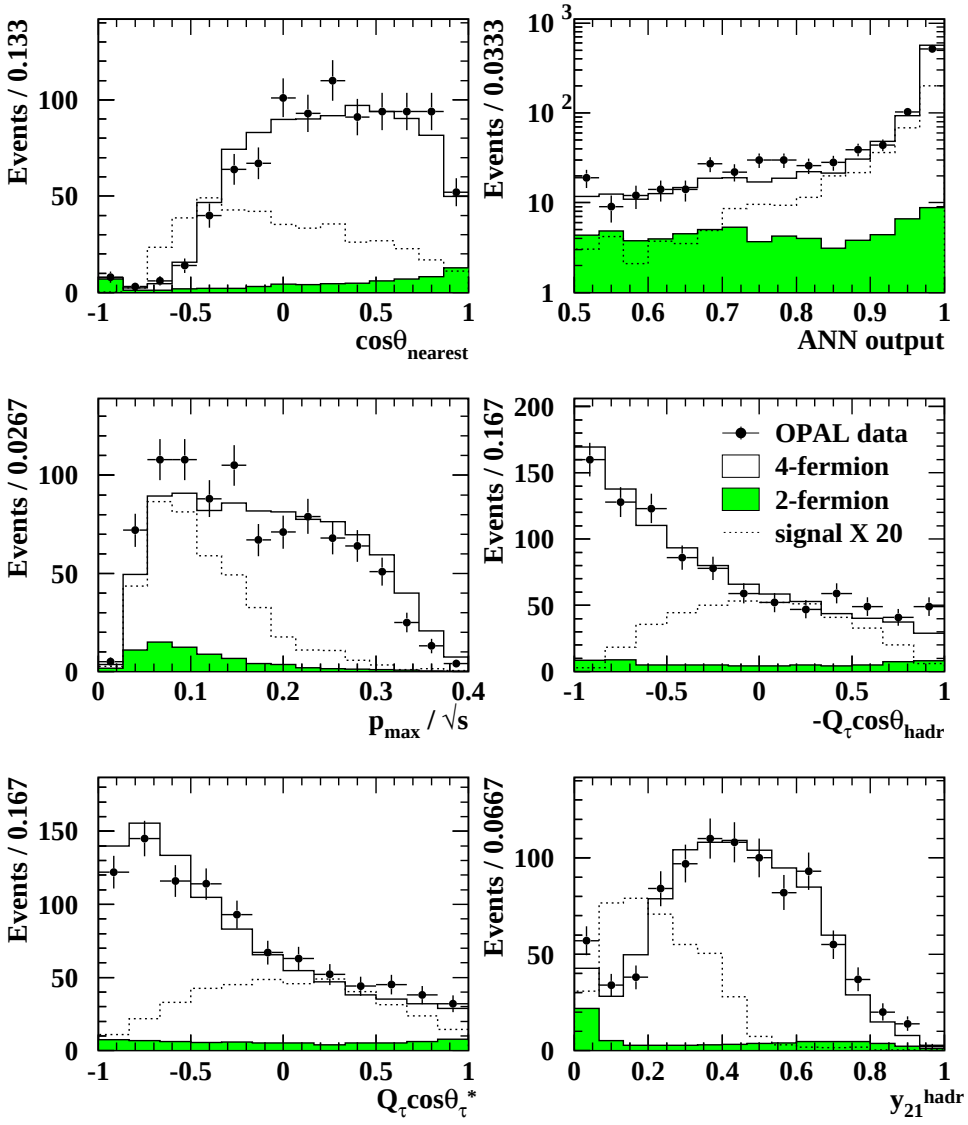

Figure 4.5: H^+H^- *search, semi-leptonic channel at* $\sqrt{s} = 189$ *GeV: Distributions of likelihood input variables (see text for explanation). Selected data events are shown as dots with error bars, the SM two- and four-fermion background estimates as shaded and open histograms, respectively, and a simulated signal of 65 GeV mass as dotted histograms. All Monte Carlo samples are normalized to the integrated luminosity of the data. For the signal* $\mathrm{BR}(H^+ \to \tau^+\nu_\tau) = 0.5$ *is assumed and the distributions are scaled up by a factor of 20 for better visibility.*

183 GeV						
Cut	Data	Background	$f\bar{f}(\gamma)$	4f	$\gamma\gamma$	Efficiency (%)
(1)	6333	6405	5304	987	114	94.4
(2)	3642	3466	2889	502	75.1	89.8
(3)	536	478	158	320	0.8	85.2
(4)	304	285	29.2	256	0.8	71.0
(5)	298	279	24.8	253	0.8	69.6
(6)	16	15.3±0.7	0.3±0.1	15.0±0.4	0.0±0.6	48.6±2.2
189 GeV						
Cut	Data	Background	$f\bar{f}(\gamma)$	4f	$\gamma\gamma$	Efficiency (%)
(1)	19499	19133.	15350.	3335.	448.	94.6
(2)	11156	10374.	8390.	1682.	302.	90.0
(3)	1658	1562.	473.	1086.	3.2	85.2
(4)	955	940.	83.5	855.	1.0	68.6
(5)	931	919.	70.4	848.	0.8	68.4
(6)	65	60.1±2.4	0.5±0.1	59.6±1.5	0.0±1.9	46.4±2.2

Table 4.4: H^+H^- *search, semi-leptonic channel at* $\sqrt{s} = 183 - 189$ *GeV: Numbers of selected data and expected background events together with the selection efficiencies for simulated signals of 60 and 65 GeV masses at* $\sqrt{s} = 183$ *and 189 GeV, respectively, after each cut. The contributions to the SM expectation from two-fermion, four-fermion and two-photon processes are also given separately. Errors are statistical only.*

$\sqrt{s}$	Signal selection efficiencies (%) for $m_{H^\pm}$								
(GeV)	50 GeV	55 GeV	60 GeV	65 GeV	70 GeV	75 GeV	80 GeV	85 GeV	90 GeV
183	47.8±2.2	50.4±2.2	48.6±2.2	46.4±2.2	35.0±2.1	30.6±2.1	17.4±1.7	7.0±1.1	3.2±0.8
189	44.0±2.2	45.4±2.2	46.8±2.2	46.4±2.2	40.0±2.2	33.4±2.1	23.4±1.9	12.4±1.5	4.0±0.9

Table 4.5: H^+H^- *search, semi-leptonic channel at* $\sqrt{s} = 183 - 189$ *GeV: Signal selection efficiencies for various charged Higgs boson masses. Errors are statistical only.*

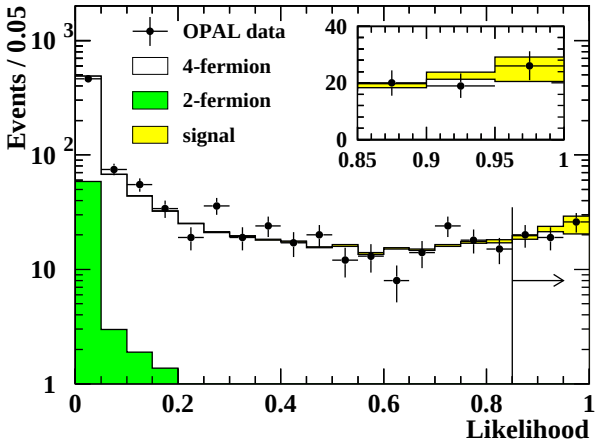

Figure 4.6: H^+H^- *search, semi-leptonic channel at* $\sqrt{s}$ *= 189 GeV: Likelihood output distribution. Selected data events are shown as dots with error bars, the SM two- and four-fermion background estimates as dark grey and open histograms, respectively, and a simulated signal of 65 GeV mass as a light grey histogram on top of the background. All Monte Carlo samples are normalized to the integrated luminosity of the data. For the signal* $BR(H^+ \to \tau^+\nu_\tau) = 0.5$ *is assumed. The arrow indicates the cut position. The insert shows the same distribution for the selected events.*

its total energy is estimated using energy and momentum constraints. Since the three-momentum of the neutrino is not known, this results in a one-constraint fit. If the fit has a χ^2 probability less than 10^{-5}, the mass is calculated instead from the measured jet four-momenta using angular information and scaling the total energy of the hadronic system to the beam energy. The resulting mass distributions, shown in Figure 4.7, are used when setting limits on the production cross-section.

4.3.3 Systematic Effects

None of the searches have revealed an excess of events above the SM expectation. Both the signal and the background estimates are subject to systematic uncertainties which have to be studied before deriving limits.

In addition to the statistical error, typically 5%, due to the limited number of Monte

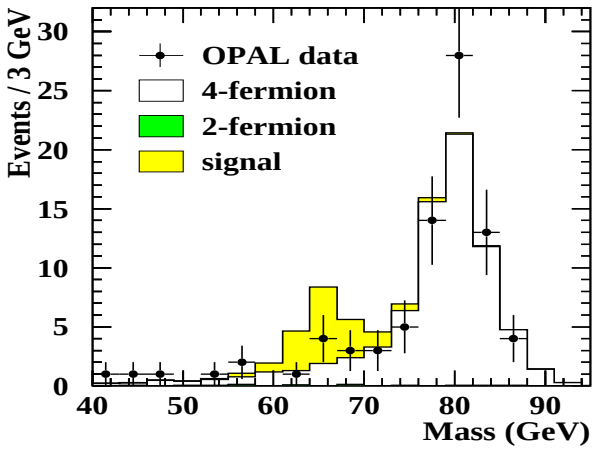

Figure 4.7: H^+H^- *search, semi-leptonic channel at* $\sqrt{s} = 183 - 189$ *GeV: Invariant mass distribution using a one-constraint kinematic fit. Selected data events are shown as dots with error bars, the SM two- and four-fermion background estimates as grey and open histograms, respectively, and a simulated signal of 65 GeV mass as a light grey histogram on top of the background. All Monte Carlo samples are normalized to the integrated luminosity of the data. For the signal* $\mathrm{BR}(H^+ \to \tau^+\nu_\tau) = 0.5$ *is assumed.*

Carlo events, the signal selection efficiencies are affected by the following:

- uncertainties on the tau lepton identification, 3.0%;
- imperfect modelling of the selection variables, 6.0% at $\sqrt{s} = 136 - 172$ GeV, 4.8% at $\sqrt{s} = 183$ GeV and 4.9% at $\sqrt{s} = 189$ GeV;
- dependence on the final state quark flavours, 2.4% at $\sqrt{s} = 130 - 172$ GeV and 6.1% at $\sqrt{s} = 183 - 189$ GeV;
- dependence on the tau polarization, 3.0%.

The flavour dependence of the selection is tested using Monte Carlo samples of $H^+H^- \to \tau^+\nu_\tau s\bar{c}$ and $H^+H^- \to \tau^+\nu_\tau b\bar{c}$. The observed differences at $\sqrt{s} = 130 - 172$ GeV are within the statistical error, but conservatively they are incorporated into the systematic error.

The background estimate is subject to the following effects:

- imperfect modelling of the hadronization and the four-fermion production processes,

9.0% at $\sqrt{s} = 130 - 172$ GeV, 8.0% at $\sqrt{s} = 183$ GeV and 1.8% at $\sqrt{s} = 189$ GeV;

- uncertainties related to the tau lepton identification, 5.0% at $\sqrt{s} = 130 - 172$ GeV and 3.0% at $\sqrt{s} = 183 - 189$ GeV;
- imperfect modelling of the selection variables, 5.0% at $\sqrt{s} = 130 - 172$ GeV, 9.0% at $\sqrt{s} = 183$ GeV and 10.3% at $\sqrt{s} = 189$ GeV.

The additional statistical error varies between $4 - 30\%$ depending on the centre-of-mass energy.

The uncertainties on the hadronization and on the modelling of four-fermion final states are estimated by comparing the predictions of PYTHIA and HERWIG for $q\bar{q}(\gamma)$, `grc4f` and EXCALIBUR for four-fermion processes.

The uncertainties in modelling the kinematic variables are estimated by scaling their values by the ratio of the RMS and by shifting them according to the difference of the means of the data and background Monte Carlo distributions.

The uncertainties on the tau lepton identification at $\sqrt{s} = 130 - 172$ GeV include the errors on electron and muon identification, as well.

The error on the integrated luminosity measured by the Silicon Tungsten luminometer is 1.4% at $\sqrt{s} = 130 - 136$ GeV, 0.6% at $\sqrt{s} = 161 - 172$ GeV, 0.5% at $\sqrt{s} = 183$ GeV and 0.3% at $\sqrt{s} = 189$ GeV.

The possible correlations between the systematic uncertainties conservatively are not taken into account. All components of the statistical and systematic errors are added in quadrature.

The net systematic error ranges between $7.8 - 8.9\%$ for the signal rate and $10.9 - 12.4\%$ for the background expectation depending on the centre-of-mass energy.

In the limit calculation, the efficiencies and background estimates have been reduced by 1.8% and 0.72% (relative) at $\sqrt{s} = 183$ and 189 GeV, respectively, in order to account for accidental vetoes due to accelerator-related backgrounds in the forward detectors.

4.4 Hadronic Final State

The hadronic channel, $H^+H^- \to q\bar{q}'q''\bar{q}''$, is characterized by an event topology with four well-separated hadronic jets and large visible energy.

Since the size and the composition of the background changes considerably with the centre-of-mass energy, the analysis flow was modified several times during the years. However, the first stage of the analysis, the selection of non-radiative four-jet events with large missing energy, remained practically the same, as outlined below:

(P1) The event must pass the off-line multihadron selection described in Section 3.2.1.

(P2) Events with a radiative photon or large missing energy are eliminated by requiring the effective centre-of-mass energy, $\sqrt{s'}$, to be at least $0.87\sqrt{s}$ and $0.82\sqrt{s}$ at centre-of-mass energies of $130 - 172$ GeV and $183 - 189$ GeV, respectively.

The visible energy in the event has to be at least $0.7\sqrt{s}$.

(P3) The events are reconstructed into four jets using the Durham algorithm. The jet resolution parameter, y_{34}, at which the number of jets changes from three to four, has to be larger than 0.01 at $\sqrt{s} = 130 - 136$ GeV, larger than 0.005 at $\sqrt{s} = 161 - 172$ GeV and larger than 0.0025 at $\sqrt{s} = 183 - 189$ GeV. The tighter cut at lower energies is necessary due to the higher level of the $q\bar{q}(\gamma)$ background. Each jet must contain at least one charged track.

(P4) At $\sqrt{s} = 161 - 172$ GeV the remaining radiative two-fermion events are further suppressed by vetoing on jets with properties compatible with those of a radiative photon, namely exactly one electromagnetic cluster, not more than two charged tracks and jet energy above $\sqrt{s} - 121$ GeV.

The variables used in the preselection are shown in Figure 4.8, comparing data and SM background prediction at $\sqrt{s} = 183$ GeV. A signal with $m_{H^\pm} = 60$ GeV is also plotted.

At this point of the selection one should exploit the differences between the signal and the SM four-jet background. At lower energies, where the background comes mainly from $q\bar{q}(\gamma)$ processes with hard gluon radiation, a simple cut based method is applied to

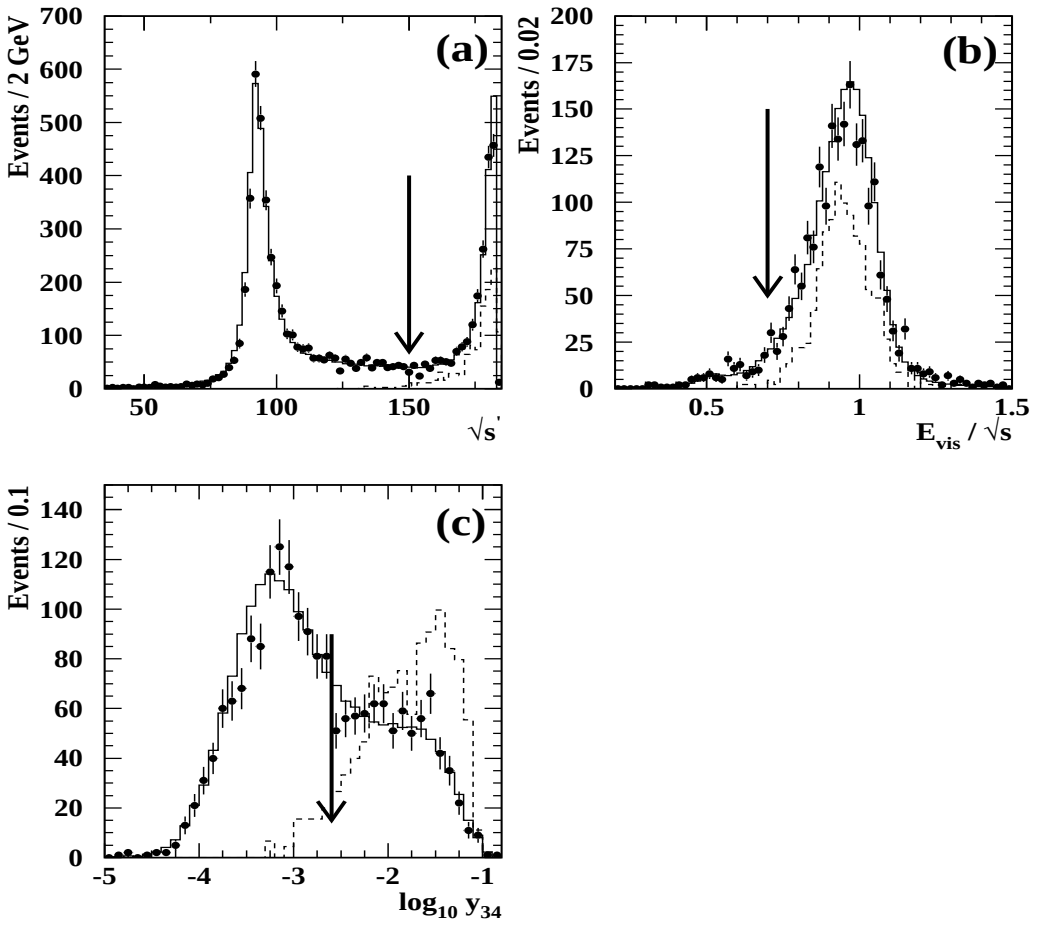

Figure 4.8: H^+H^- *search, hadronic channel at* $\sqrt{s} = 183$ *GeV: Distributions of preselection variables: (a) effective centre-of-mass energy, (b) visible energy scaled by the centre-of-mass energy and (c) logarithm of the jet resolution parameter. Selected data events are shown as dots with error bars the SM background estimates as solid histograms and a simulated signal of 60 GeV mass as dashed histograms. All Monte Carlo samples are normalized to the integrated luminosity of the data. For the signal* $\mathrm{BR}(H^+ \to \tau^+\nu_\tau) = 0$ *is assumed and the distributions are scaled up by a factor of 50 for better visibility. The arrows indicate the cut positions.*

accomplish this task. At $\sqrt{s} = 183 - 189$ GeV a multidimensional likelihood analysis is used to fight the overwhelming and partly irreducible background from W^+W^- production.

4.4.1 Analysis of Data Collected at $\sqrt{s} = 130 - 172$ GeV

After the selection of four-jet events the following requirements are imposed to further reduce the $q\bar{q}(\gamma)$ background:

(L1) The polar angle of the thrust axis has to satisfy $|\cos\theta_{\rm thr}| < 0.8$.

The event shape parameter, C, has to be larger than 0.6 at $\sqrt{s} = 130 - 136$ GeV and larger than 0.45 at $\sqrt{s} = 161 - 172$ GeV.

The cosine of the angle between any pair of jets must be smaller than 0.62 at $\sqrt{s} = 130 - 136$ GeV and 0.66 at higher centre-of-mass energies.

(L2) To test the compatibility of the event with the decay of two equal mass objects a four-constraint kinematic fit requiring energy and momentum conservation is performed and the mass difference between the two dijet systems is calculated for all three possible jet pair combinations. The event is discarded if the χ^2 probability of the fit is below 0.01 or if the smallest mass difference is larger than 6 GeV at $\sqrt{s} = 130 - 136$ GeV and 8 GeV at higher centre-of-mass energies.

For all events passing this cut a five-constraint kinematic fit is performed for all three jet pair combinations imposing energy and momentum conservation and equal dijet invariant masses and the event is rejected if the largest χ^2 probability is below 0.01.

At centre-of-mass energies of 161 GeV and above a veto is applied against W^+W^- events using the dijet masses calculated after the four-constraint kinematic fit:

(L3) At $\sqrt{s} = 161$ GeV, since the $W^\pm$ bosons are produced practically at rest, the two jets having the largest measured opening angle are assigned to one of the $W^\pm$ bosons and the two remaining jets to the other. An event is rejected if both jet pairs have an invariant mass greater than 70 GeV.

At $\sqrt{s} = 172$ GeV the event is rejected if any of the three possible jet pair combinations

	130 GeV			136 GeV		
Cut	Data	Background	Efficiency (%)	Data	Background	Efficiency (%)
(P1)	744	733.8±3.2	99.8±0.2	676	679.7±3.1	99.8±0.2
(P2)	173	201.7±2.1	94.2±1.0	184	180.2±1.9	93.0±1.1
(P3)	11	11.5±0.6	62.8±2.2	14	11.6±0.6	59.4±2.2
(L1)	4	3.7±0.3	49.2±2.2	4	3.9±0.3	50.4±2.2
(L2)	2	1.2±0.2	33.4±2.1	2	1.6±0.2	34.4±2.1
	161 GeV			172 GeV		
Cut	Data	Background	Efficiency (%)	Data	Background	Efficiency (%)
(P1)	1497	1453.5±3.1	100.0±0.2	1393	1310.8±3.4	100.0±0.2
(P2)	392	374.5±1.4	93.6±1.1	359	368.9±1.3	94.6±1.0
(P3)	62	53.2±0.5	75.6±1.9	88	82.5±0.5	72.2±2.0
(P4)	59	50.8±0.5	75.6±1.9	87	80.2±0.5	72.2±2.0
(L1)	21	19.2±0.3	67.2±2.1	36	38.1±0.3	59.4±2.2
(L2)	8	8.9±0.2	52.4±2.2	14	18.6±0.3	48.8±2.2
(L3)	3	5.0±0.2	45.4±2.2	5	7.5±0.2	42.2±2.2

Table 4.6: H^+H^- *search, hadronic channel at* $\sqrt{s} = 130 - 172$ *GeV: Numbers of selected data and expected background events together with the selection efficiencies for a simulated signal of 50 GeV mass after each cut. Errors are statistical only.*

yields invariant masses greater than 74 GeV for both of the two dijet systems.

Table 4.6 shows the number of selected events, the estimated background and the fraction of signal events retained for $m_{H^\pm} = 50$ GeV at all centre-of-mass energies after each cut. Data are in agreement with the expected background. In total, twelve events are selected in the data, while 15.3±0.4 (statistical error) are expected from SM processes. The four-fermion processes account for 10.1±1.2%, 32.3±1.7% and 64.8±3.5% of the expected background at $\sqrt{s} = 130 - 136$, 161 and 172 GeV, respectively. The signal selection efficiencies for various Higgs boson masses are listed in Table 4.7. The decrease of efficiency for high masses is due to the W^+W^- veto.

$\sqrt{s}$	Signal selection efficiencies (%) for $m_{\mathrm{H}^\pm}$							
(GeV)	40 GeV	45 GeV	50 GeV	55 GeV	60 GeV	65 GeV	70 GeV	75 GeV
130	32.4±2.1	32.4±2.1	33.4±2.1	29.6±2.0	22.2±1.9	—	—	—
136	29.8±2.0	36.6±2.2	34.6±2.1	26.0±2.0	26.8±2.0	—	—	—
161	36.0±2.1	41.4±2.2	45.4±2.2	41.4±2.2	36.4±2.2	31.4±2.1	28.0±2.0	—
172	24.6±1.9	40.4±2.2	42.2±2.2	39.6±2.2	39.0±2.2	29.4±2.0	31.2±2.1	20.0±1.8

Table 4.7: $\mathrm{H}^+\mathrm{H}^-$ *search, hadronic channel at* $\sqrt{s} = 130 - 172$ *GeV: Signal selection efficiencies for various charged Higgs boson masses. Errors are statistical only. Dashes indicate masses which are not simulated.*

For the remaining events, the jet pair association giving the highest χ^2 probability in the five-constraint kinematic fit is retained. In Figure 4.9 the resulting invariant mass distribution is shown for the selected data events together with the SM background expectation and a signal of $m_{\mathrm{H}^\pm} = 50$ GeV. The mass resolution is $0.6 - 1.2$ GeV, depending on the centre-of-mass energy and the Higgs boson mass.

4.4.2 Analysis of Data Collected at $\sqrt{s} = 183 - 189$ GeV

At higher energies the suppression of the $\mathrm{W}^+\mathrm{W}^-$ background is the hardest challenge, especially if the mass of the $\mathrm{W}^\pm$ boson and the mass of the charged Higgs boson are close to each other. To exploit fine differences between the signal and the background, like the expected angular distributions, a set of variables are combined using a likelihood technique.

Before entering the likelihood selection the event should pass two more requirements to suppress the $\mathrm{q\bar{q}}$ background to almost negligible level and to ensure that the variables based on kinematic fits are well-defined.

(H1) A four-constraint kinematic fit requiring energy and momentum conservation should converge and yield a χ^2 probability larger than 10^{-5}.

A five-constraint kinematic fit requiring in addition equal dijet invariant masses should converge and yield a χ^2 probability larger than 10^{-5} for at least one of the three jet

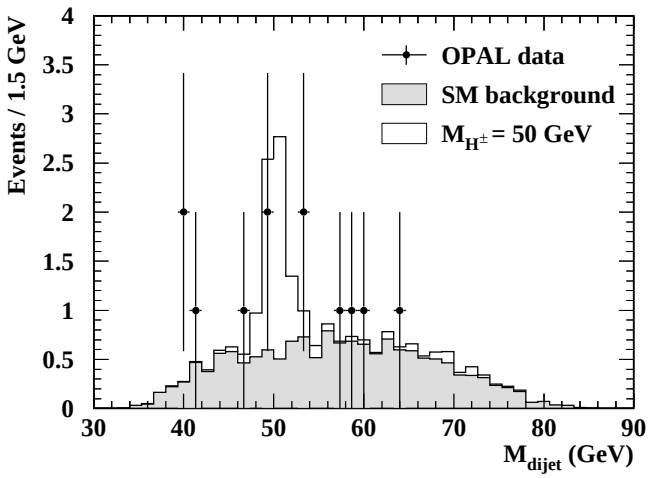

Figure 4.9: H^+H^- *search, hadronic channel at* $\sqrt{s} = 130 - 172$ *GeV: Invariant mass distribution using a five-constraint kinematic fit. Selected data events are shown as dots with error bars, the SM background estimate as a shaded histogram and a simulated signal of 50 GeV mass as an open histogram on top of the background. All Monte Carlo samples are normalized to the integrated luminosity of data. For the signal* $\mathrm{BR}(H^+ \to q\bar{q}') = 1$ *is assumed.*

pair combinations.

(H2) The C event shape parameter must be larger than 0.45.

The χ^2 probabilities of the kinematic fits is shown in Figure 4.10, comparing data and Standard Model background.

In the likelihood selection three event classes are defined: SM two-fermion, four-fermion and $H^+H^- \to q\bar{q}'q''\overline{q}''$. The signal reference histograms are produced adding charged Higgs boson samples with masses of $50 - 70$ GeV at $\sqrt{s} = 183$ GeV and $55 - 75$ GeV at $\sqrt{s} = 189$ GeV. The likelihood output is computed combining the following five variables:

- the cosine of the smallest jet-jet angle, $\cos\alpha_{\mathrm{min}}$;
- the difference between the largest and smallest jet energy, $E_{\mathrm{max}} - E_{\mathrm{min}}$, after the four-constraint kinematic fit;

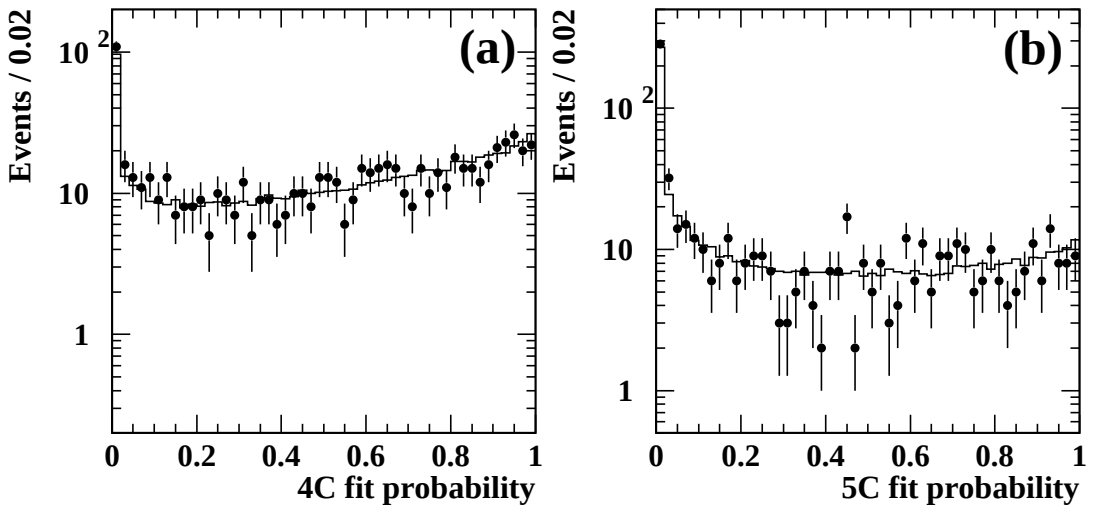

Figure 4.10: H^+H^- *search, hadronic channel at* $\sqrt{s} = 183$ *GeV:* χ^2 *probability distributions of the (a) four- and (b) five-constraint kinematic fits. Selected data events are shown as dots with error bars and the SM background estimates as solid histograms. All Monte Carlo samples are normalized to the integrated luminosity of the data.*

- the cosine of the polar angle of the thrust axis, $\cos\theta_{\text{thrust}}$;
- the cosine of the dijet production angle, $\cos\theta_{\text{dijet}}$, multiplied by the dijet charge[2], Q_{dijet}, for the combination with the highest probability given by the five-constraint kinematic fit;
- the smallest dijet mass difference, ΔM_{min}, after the four-constraint fit.

(H3) As a final selection, events are selected if their likelihood output is greater than 0.6.

The distributions of the input variables to the likelihood selection are shown in Figure 4.11 while the resulting likelihood distribution is shown in Figure 4.12. Table 4.8 shows

[2]If there is more than one charged track in a jet, the jet-charge is calculated as $\Sigma q^{(i)} p_{\text{L}}^{(i)0.5} / \Sigma p_{\text{L}}^{(i)0.5}$, where the sum goes over each track within the jet, $q^{(i)}$ is the charge of the track and $p_{\text{L}}^{(i)}$ is its momentum parallel to the jet direction. A charge of +1 is assigned to the dijet system with the larger sum of the two individual jet charges, and a charge of −1 to the other.

183 GeV						
Cut	Data	Background	$f\bar{f}(\gamma)$	4f	$\gamma\gamma$	Efficiency (%)
(P1)	6333	6405	5304	987	114	100.
(P2)	1939	1980	1457	519	4.3	97.0
(P3)	707	703	280	422	1.3	89.0
(H1)	534	542	183	358	0.4	78.0
(H2)	454	445	104	341	0.3	76.6
(H3)	50	48.8±0.9	9.0±0.3	39.8±0.7	0.0±0.6	42.8±2.2
189 GeV						
Cut	Data	Total bkg.	$f\bar{f}(\gamma)$	4f	$\gamma\gamma$	Efficiency (%)
(P1)	19499	19133.	15350.	3335.	448.	99.9
(P2)	5960	5973.	4210.	1750.	12.7	96.2
(P3)	2026	1934.	576.	1356.	2.1	81.9
(H1)	1656	1603.	390.	1211.	1.7	75.1
(H2)	1491	1427.	255.	1171.	1.3	73.7
(H3)	156	153.8±3.0	20.4±0.8	133.4±2.2	0.0±1.9	35.3±0.9

Table 4.8: H^+H^- *search, hadronic channel at* $\sqrt{s} = 183 - 189$ *GeV: Numbers of selected data and expected background events together with the selection efficiencies for simulated signals of 60 and 65 GeV masses at* $\sqrt{s} = 183$ *and 189 GeV, respectively, after each cut. The contributions to the SM expectation from two-fermion, four-fermion and two-photon processes are also given separately. Errors are statistical only.*

the number of selected data events, the estimated background and the fraction of signal events with $m_{H^\pm} = 60$ and 65 GeV at $\sqrt{s} = 183$ and 189 GeV, respectively, retained after each cut. In total, 206 events are selected in the data, while 202.6 ± 3.1 (statistical error) events are expected from SM processes. The four-fermion processes account for 82% and 87% of the expected background at $\sqrt{s} = 183$ and 189 GeV, respectively, and result in a large peak centred at the $W^\pm$ mass. The signal selection efficiencies are given in Table 4.9 for various Higgs boson masses.

For the selected events, the jet pair association giving the highest χ^2 probability in

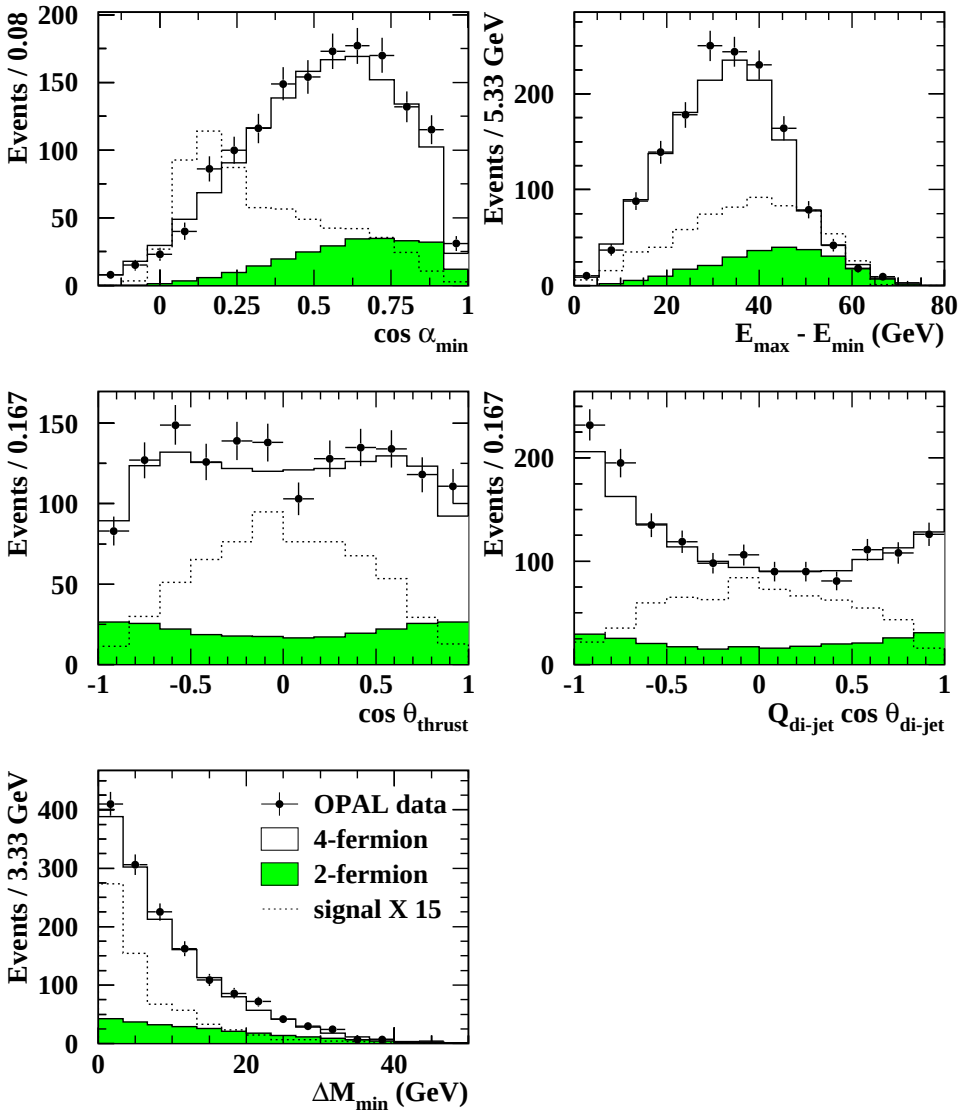

Figure 4.11: H^+H^- *search, hadronic channel at* $\sqrt{s} = 189$ *GeV: Distributions of likelihood input variables (see text for explanation). Selected data events are shown as dots with error bars, the SM two- and four-fermion background estimates as shaded and open histograms, respectively, and a simulated signal of 65 GeV mass as dotted histograms. All Monte Carlo samples are normalized to the integrated luminosity of the data. For the signal* $BR(H^+ \to q\bar{q}') = 1$ *is assumed and the distributions are scaled up by a factor of 15 for better visibility.*

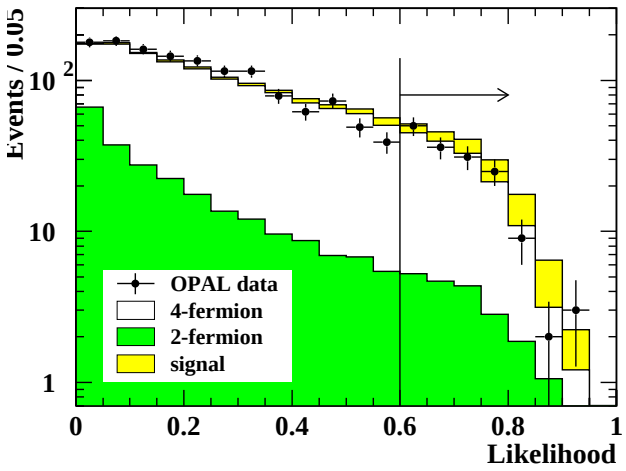

Figure 4.12: H^+H^- *search, hadronic channel at* $\sqrt{s} = 189$ *GeV: Likelihood output distribution. Selected data events are shown as dots with error bars, the SM two- and four-fermion background estimates as dark grey and open histograms, respectively, and a simulated signal of 65 GeV mass as a light grey histogram on top of the background. All Monte Carlo samples are normalized to the integrated luminosity of the data. For the signal* $\mathrm{BR}(H^+ \to q\bar{q}') = 1$ *is assumed. The arrow indicates the cut position.*

$\sqrt{s}$	Signal selection efficiencies (%) for $m_{H^\pm}$								
(GeV)	50 GeV	55 GeV	60 GeV	65 GeV	70 GeV	75 GeV	80 GeV	85 GeV	90 GeV
183	36.8±2.2	42.0±2.2	42.8±2.2	33.0±2.1	26.0±2.0	16.4±1.7	12.4±1.5	12.2±1.5	11.6±1.4
189	19.6±1.8	30.8±2.1	33.0±2.1	35.3±0.9	24.6±1.9	20.2±0.7	15.4±1.6	11.0±1.4	8.6±1.3

Table 4.9: H^+H^- *search, hadronic channel at* $\sqrt{s} = 183 - 189$ *GeV: Signal selection efficiencies for various charged Higgs boson masses. Errors are statistical only.*

the five-constraint fit is retained. The resulting mass resolution ranges from 0.7 GeV to 1.4 GeV. The invariant mass distributions, used when setting limits on the production cross-section, are shown in Figure 4.13.

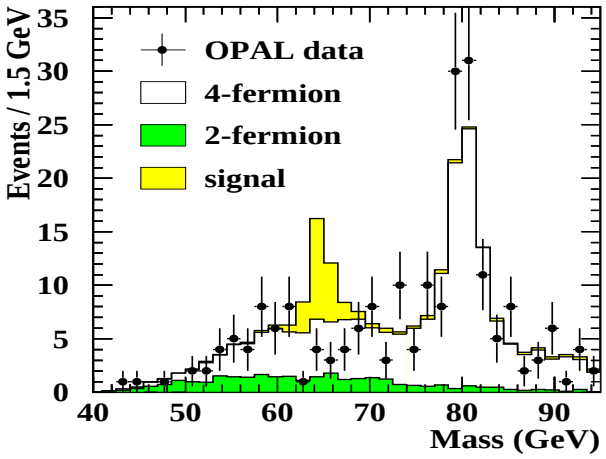

Figure 4.13: H^+H^- *search, hadronic channel at* $\sqrt{s} = 183 - 189$ *GeV: Invariant mass distribution using a five-constraint kinematic fit. Selected data events are shown as dots with error bars, the SM two- and four-fermion background estimates as grey and open histograms, respectively, and a simulated signal of 65 GeV mass as a light grey histogram on top of the background. All Monte Carlo samples are normalized to the integrated luminosity of the data. For the signal* $\mathrm{BR}(H^+ \to q\bar{q}') = 1$ *is assumed.*

4.4.3 Systematic Effects

The determination of the systematic uncertainties follows the methods described in Section 4.3.3.

The signal selection efficiencies in addition to the statistical error, typically 6%, due to the limited number of Monte Carlo events, are affected by the following:

- imperfect modelling of the selection variables, 5.0% at $\sqrt{s} = 136 - 172$ GeV, 3.0% at $\sqrt{s} = 183$ GeV and 3.1% at $\sqrt{s} = 189$ GeV;
- uncertainties of the jet resolutions and energy scales in the kinematic fits, 2.0%;

- dependence on the final state quark flavour, 2.4% at $\sqrt{s} = 130 - 172$ GeV and 4.0% at $\sqrt{s} = 183 - 189$ GeV.

The effects of a possible flavour dependence are estimated by comparing signal MC samples with $c\bar{s}\bar{c}s$, $c\bar{s}\bar{c}b$ and $c\bar{b}\bar{c}b$ final states. At $\sqrt{s} = 130 - 172$ GeV the observed difference is within the statistical error of the samples, but conservatively it is taken into account separately.

The background estimate is subject to the following effects:

- uncertainties in modelling the hadronization process and the four-fermion final states, 7% at $\sqrt{s} = 136 - 172$ GeV, 2.0% at $\sqrt{s} = 183$ GeV and 1.6% at $\sqrt{s} = 189$ GeV;
- imperfect modelling of the selection variables, 6.0% at $\sqrt{s} = 136 - 172$ GeV, 4.9% at $\sqrt{s} = 183$ GeV and 2.5% at $\sqrt{s} = 189$ GeV;
- uncertainties of the jet resolutions and energy scales in the kinematic fits, 4.0%.

The additional statistical error ranges between 2 and 14% depending on the centre-of-mass energy.

The error due to the kinematic fits is determined by varying the centre-of-mass energy by ± 300 MeV, the jet momenta by $\pm 1\%$ and the error on the jet momenta and jet angles by $\pm 10\%$.

At $\sqrt{s} = 136 - 172$ GeV, where the $q\bar{q}(\gamma)$ background plays an important role, the theoretical uncertainty on the prediction of the QCD four-jet rate, conservatively, is estimated by its experimental error of 15% dominated by statistics, giving an 8% error on the background expectation after taking account the relative weight of the QCD background.

The error on the integrated luminosity measured by the Silicon Tungsten luminometer is 1.4% at $\sqrt{s} = 130 - 136$ GeV, 0.6% at $\sqrt{s} = 161 - 172$ GeV, 0.5% at $\sqrt{s} = 183$ GeV and 0.3% at $\sqrt{s} = 189$ GeV.

The total systematic error varies in the range $5.4 - 6.1\%$ for the signal rate and $5.0 - 12.9\%$ for the background expectation. The significant decrease of the uncertainty on the background estimate with increasing centre-of-mass energy is due to the smaller weight of QCD processes.

4.5 Results and Interpretation

None of the searches presented here revealed any significant excess over the expectation from SM processes. All energies combined, 81 events are observed in the semi-leptonic final state with a SM expectation of 78.1 ± 2.5 (stat) ±6.9 (syst) events, and 218 events are seen in the hadronic channel for a SM background of 217.9 ± 3.2 (stat) ± 8.5 (syst) events.

The result is used to derive limits at the 95% CL on the production cross-section using the method described in the second part of Section 3.2.9, and in combination with searches in the leptonic final state [78] on the charged Higgs boson mass.

The expected background is reduced by its systematic error in each channel, and accounted for by considering the selected events as *signal plus background*. The systematic error on the integrated luminosity measurement and the error on the signal selection efficiency is taken into account using Equation 3.18.

Upper limits scaled to $\sqrt{s} = 189$ GeV on the production cross-section times branching fraction of the decay into a given final state are presented in Figure 4.14(a). The results from various centre-of-mass energies are combined assuming the s-dependence of the charged Higgs boson production cross-section within the framework of 2HDMs including initial state radiation as predicted by PYTHIA.

Lower bounds on the mass of the charged Higgs bosons are presented in Figure 4.14(b) as a function of the branching ratio BR($H^+ \to \tau^+\nu_\tau$), assuming BR($H^+ \to \tau^+\nu_\tau$) + BR($H^+ \to q\bar{q}$) = 1. The expected mass limit from simulated background experiments, assuming no signal, is also shown. Charged Higgs bosons are excluded up to a mass of 68.7 GeV at the 95% CL, independent of the branching ratio BR($H^+ \to \tau^+\nu_\tau$). The difference between the observed and expected limits for BR($H^+ \to \tau^+\nu_\tau$) $\approx 0.2 - 0.8$ is mainly due to three candidate events observed at 183 GeV in the semi-leptonic channel between 66 and 68 GeV. All three events are consistent with W^+W^- production.

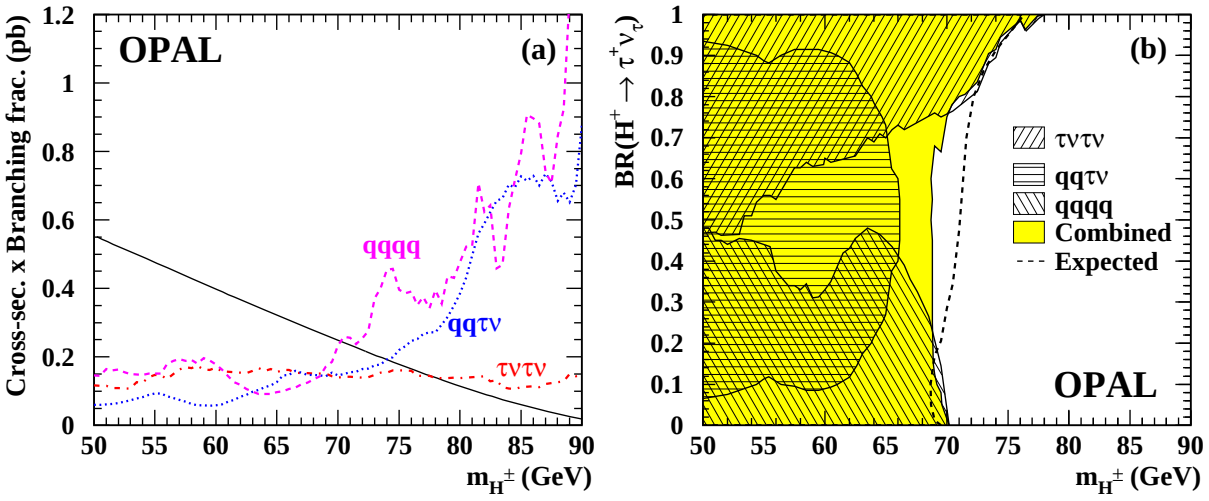

Figure 4.14: *Charged Higgs boson search: (a) Upper limits at the 95% CL, scaled to* $\sqrt{s}$ *= 189 GeV, on the production cross-section times branching fraction of the final states considered. Results from the hadronic, semi-leptonic and leptonic channels are shown as dashed, dotted and dash-dotted lines, respectively, and the predicted charged Higgs boson production cross-section in the framework of 2HDMs as a solid line. Note that the maximum branching fraction for the semi-leptonic final state is 0.5. (b) Excluded regions at the 95% CL in the* $[m_{\mathrm{H}^\pm}, \mathrm{BR}(\mathrm{H}^+ \to \tau^+\nu_\tau)]$ *plane. The results from each of the channels are shown separately as different hatched areas, the combined exclusion as a shaded area and the expected limit from simulated background experiments as a dashed line.*

4.6 Conclusions

The searches for charged Higgs bosons presented here and based on data collected by the OPAL detector at $\sqrt{s} = 130 - 189$ GeV centre-of-mass energy have not revealed any significant excess over the expected backgrounds. Cross-section upper limits are derived for the studied final states and in combination with previous search results using LEP1 data new limits on the mass of the charged Higgs bosons are set at the 95% CL. Charged Higgs bosons are excluded for masses below 68.7 GeV, assuming $\mathrm{BR}(\mathrm{H}^+ \to \mathrm{q}\bar{\mathrm{q}}') + \mathrm{BR}(\mathrm{H}^+ \to \tau^+\nu_\tau) = 1$, independent of the branching ratio $\mathrm{BR}(\mathrm{H}^+ \to \tau^+\nu_\tau)$.

Chapter 5

Search for an Excess in the Four-Jet Final State

5.1 Motivation

In a run of LEP in 1995 at centre-of-mass energies of $\sqrt{s} = 130$ and 136 GeV, the ALEPH Collaboration observed [79] an excess of events with four distinct jets compared with the SM expectation. Such an excess could be due to the production of new particles X and Y, each decaying into two hadronic jets in the process $e^+e^- \rightarrow XY \rightarrow$ four jets. The two particles could have equal or unequal masses. Grouping the jets into pairs, calculating their pair invariant masses M_{ij} and M_{kl}, and selecting the combination yielding the smallest mass difference $\Delta M = |M_{ij} - M_{kl}|$, ALEPH observed a clustering of nine events in a mass window of 6.3 GeV, centred around $M = M_{ij} + M_{kl} \approx 105$ GeV, with a SM expectation of 0.8 events in the same window. The choice of the combination with the minimum ΔM would tend to favour the selection of particles of equal mass or with a small mass difference.

The ALEPH analysis was originally designed to search for the process $e^+e^- \rightarrow h^0A^0$; however, the observed cross-section and the general properties of the observed events disfavour this hypothesis. In particular, the excess events show no enrichment in b-flavour.

The ALEPH Collaboration also reported a slight excess of events around the same dijet

invariant mass sum at the higher centre-of-mass energies of 161 and 172 GeV [80]. When summarizing the results obtained between 130 and 172 GeV, ALEPH has quoted 18 events clustering close to 105 GeV in M for a SM background prediction of 3.1 events.

In response to these observations, all LEP Collaborations have performed a dedicated search for anomalous four-jet production [81, 82, 83, 84]. The results of the individual searches have also been combined within a working group formed by the four experiments [85]. In 1997, LEP made short runs at $\sqrt{s} = 130$ and 136 GeV with an integrated luminosity similar to that of 1995 at these centre-of-mass energies for a repeated test of the signal hypothesis.

There was a great deal of theoretical speculation on the cause of this excess [86, 87, 88] despite the lack of confirmation from the other LEP experiments.

An analysis [89] of the data collected by the OPAL Collaboration is presented here that intends to look for pair-produced heavy particles with a mass difference up to 30 GeV in the four-jet final state with no constraint on the flavour of the quarks. This broader search is motivated by the fact that an analysis performed by the ALEPH Collaboration that constrains the masses of the two dijet systems to be equal [65] indicates that the excess events are not consistent with the hypothesis of the production of equal mass particles. The lack of excess events in our analysis is used to set cross-section limits as a function of the dijet mass sum for mass differences up to 30 GeV.

5.2 Data and Monte Carlo Simulation

The data used in this search are collected by the OPAL detector between 1995 and 1997 at centre-of-mass energies of $130 - 183$ GeV, as summarized in Table 5.1.

The main background for the selection of anomalous four-jet events comes from quark pair events with hard gluon emission with or without initial state photon radiation and from four-fermion production processes, predominantly $\mathrm{W^+W^-}$ production. We have used the SM Monte Carlo samples as described in Section 3.1.

The signal selection efficiencies are estimated using the HZHA generator to simulate

$\sqrt{s}$ (GeV)	Year	$\int \mathcal{L}$ pb^{-1}
130.3	1995	2.7
136.2	1995	2.6
161.3	1996	10.0
172.1	1996	10.3
130.0	1997	2.6
136.0	1997	3.4
182.7	1997	57.1

Table 5.1: *Search for anomalous production of four-jet events: Summary of data samples. Luminosity weighted centre-of-mass energies, years of collection and integrated luminosities.*[1]

the production of supersymmetric Higgs bosons $e^+e^- \to h^0A^0 \to b\bar{b}b\bar{b}$ as a model for the signal process $e^+e^- \to XY \to 4$ jets. Events for fixed values of m_{A^0} and m_{h^0} in the range 100 GeV $\leq m_{A^0} + m_{h^0} \leq$ 140 GeV with $|m_{A^0} - m_{h^0}| \leq 30$ GeV are generated. Samples with h^0A^0 decays into other final states, namely $s\bar{s}s\bar{s}$, $c\bar{c}c\bar{c}$ and gggg, at a mass of $m_{A^0} = m_{h^0} = 55$ GeV and H^+H^- decays into four quarks, as described in Section 4.2, are used to check for flavour dependence.

5.3 Analysis

The main features of the signal process are four well-defined, energetic, hadronic jets and total visible energy of the event close to the centre-of-mass energy. The SM background expectation changes considerably in size and composition between $\sqrt{s}$ =130 GeV and 183 GeV. At 130 – 136 GeV, the main background comes from quark pair production both with or without initial state radiation and accompanied by hard gluon emission. Above the threshold for $e^+e^- \to W^+W^-$ at $\sqrt{s} = 161$ GeV, the background from SM

[1]The integrated luminosities slightly differ from the ones given in 4.1, because different detectors are required to be fully operational.

four-fermion processes is important and becomes larger with increasing $\sqrt{s}$. A procedure to reject $W^+W^- \to q\overline{q}'q''\overline{q}'''$ is implemented for centre-of-mass energies of $161 - 183$ GeV. Two-photon processes have a large total cross-section at all energies, but the selection requirement of the presence of four energetic hadronic jets reduces them to a negligible level.

The analysis has been optimized for detecting a possible signal for the process $e^+e^- \to XY$ in the form of an excess of events with similar mass sums $M = M_X + M_Y$ in the four-jet topology. It follows similar philosophy like the selection presented in Section 4.4.1, but has been designed to retain sensitivity even when the mass difference $\Delta M = |M_X - M_Y|$ is as large as 30 GeV. Efficiencies and backgrounds are estimated for different values of M and ΔM.

The event selection described below is developed to be as insensitive as possible to the flavours of the final state quarks. Although the methods employed at each of the centre-of-mass energies are similar, the optimal cut values in most cases depend on $\sqrt{s}$.

(1) The events must pass the off-line multihadron selection described in Section 3.2.1.

(2) The effective centre-of-mass energy after initial state radiation, $\sqrt{s'}$, has to be at least $0.87\sqrt{s}$.

The measured visible mass, $M_{\rm vis}$, is required to be between $\sqrt{s} - 40$ GeV and $\sqrt{s} + 30$ GeV at $130 - 136$ GeV, between 100 and 200 GeV at $\sqrt{s} = 161$ GeV, between 110 and 210 GeV at $\sqrt{s} = 172$ GeV and between 120 and 220 GeV at $\sqrt{s} = 183$ GeV.

(3) The charged particles and calorimeter clusters are grouped into four jets using the Durham algorithm. To discriminate against poorly reconstructed events, a kinematic fit imposing energy and momentum conservation is required to yield a χ^2 probability larger than 0.01.

The jet resolution parameter, y_{34}, at which the number of jets changes from three to four, is required to be larger than 0.007 at $\sqrt{s} = 130 - 136$ GeV and larger than 0.005 at $\sqrt{s} = 161 - 183$ GeV.

Each of the four jets is required to contain at least two tracks at $\sqrt{s} = 130 - 136$ GeV

and at least one track at higher energies.

(4) In the case of the $\sqrt{s} = 161 - 183$ GeV data, the background from radiative quark pair events is further reduced by eliminating events where one of the four jets is compatible with a radiative photon, namely that it has exactly one electromagnetic cluster, not more than two tracks (possibly from a photon conversion), and energy between 45 and 65 GeV at $\sqrt{s} = 161$ GeV, between 52 and 72 GeV at $\sqrt{s} = 172$ GeV and between 60 and 80 GeV at $\sqrt{s} = 183$ GeV.

(5) The polar angle of the thrust axis is required to satisfy $|\cos\theta_{\rm thr}| < 0.9$ at $\sqrt{s} = 130 - 136$ GeV and $|\cos\theta_{\rm thr}| < 0.8$ at $\sqrt{s} = 161 - 183$ GeV.

(6) To reduce background from $\rm q\bar{q}$ events, the event shape parameter C is required to be larger than 0.7 at $\sqrt{s} = 130 - 136$ GeV and larger than 0.6 at higher energies.

(7) To ensure well-separated jets for better kinematic fits, the angle between any two jets is required to exceed 0.8 radians for $\sqrt{s} = 161 - 183$ GeV data.

(8) Explicit vetoes against the process $\rm e^+e^- \to W^+W^-$ are applied above 161 GeV, the $\rm W^+W^-$ threshold.

At $\sqrt{s} = 161$ GeV, the two $\rm W^\pm$ bosons are produced almost at rest. The two jets having the largest opening angle are assigned to one of the $\rm W^\pm$ bosons and the two remaining jets to the other. An event is rejected if both jet pairs have an invariant mass between 75 GeV and 90 GeV.

At $\sqrt{s} = 172$ and 183 GeV, a more sophisticated veto is applied. The four jets are combined into pairs, and for all three combinations the event is refitted constraining the total energy to $\sqrt{s}$ and the total momentum to zero, and also constraining the masses of the two jet pairs to be equal (five constraints). From the three combinations, the one yielding the largest χ^2 fit probability is considered. If the jet pair mass from the fit exceeds 75 GeV and the fit probability is at least 0.01, the event is rejected.

The four jets can be associated into pairs in three ways, yielding either the smallest, the largest or an intermediate value of the dijet mass difference ΔM. For $M_{\rm X} \approx M_{\rm Y}$, the signal occurs as a pronounced peak in the distribution of the dijet mass sum M for the

association with the smallest ΔM, with only a small accumulation in the distribution of M corresponding to the intermediate value of ΔM. For $M_{\mathrm{X}} \neq M_{\mathrm{Y}}$, the jet associations with the smallest and intermediate ΔM tend to share more evenly the probability of being the correct one. This behaviour is illustrated in Figure 5.1.

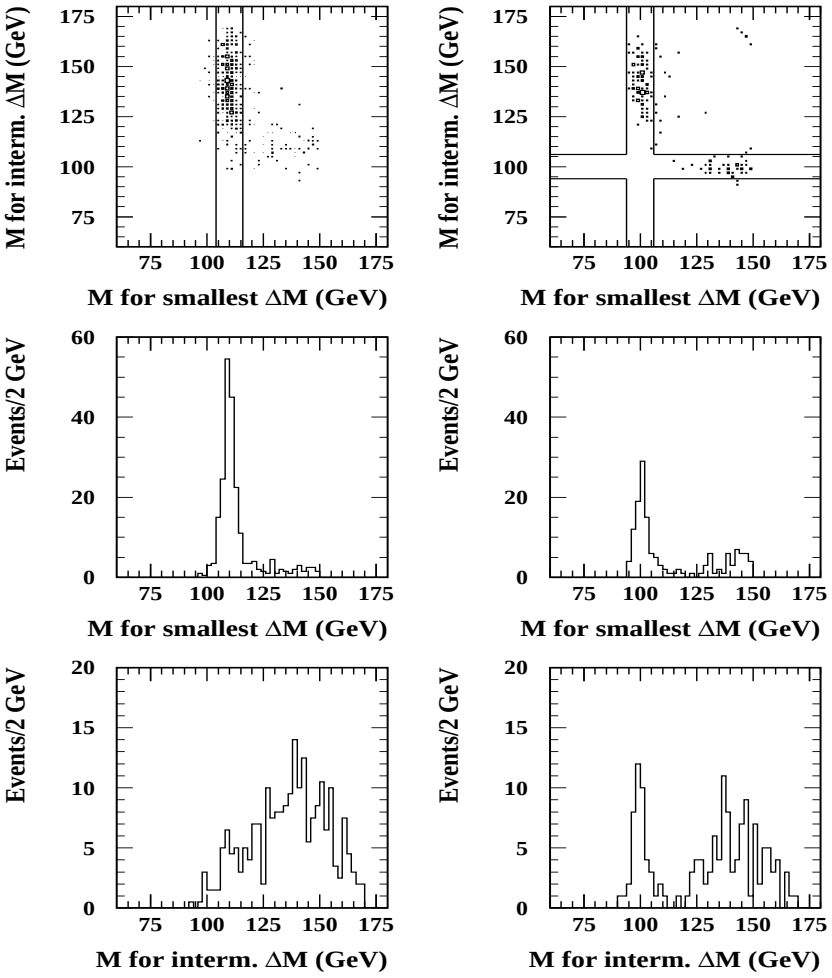

Figure 5.1: *Search for anomalous production of four-jet events at $\sqrt{s}$ = 172 GeV: Two dimensional distributions (top) and projections of the dijet mass sums for the jet combinations with the smallest (abscissa, projection in the middle) and intermediate (ordinate, projection at the bottom) dijet mass difference for a simulated signal of $M_{\mathrm{X}} = M_{\mathrm{Y}} = 55$ GeV (left) and $M_{\mathrm{X}} = 40$ GeV and $M_{\mathrm{Y}} = 60$ GeV (right). Both samples contain 500 events before selection.*

	Without W^+W^- Veto		With W^+W^- Veto		After Mass Selection	
Data Sample	Observed	Expected	Observed	Expected	Observed	Expected
130 − 136 GeV	18	17.0 ± 0.6	18	17.0 ± 0.6	4	3.1 ± 0.3
161 GeV	11	15.8 ± 0.3	8	13.6 ± 0.3	2	2.7 ± 0.1
172 GeV	36	33.8 ± 0.3	21	16.2 ± 0.2	4	2.9 ± 0.1
183 GeV	190	210.1 ± 1.2	70	81.6 ± 0.8	6	8.9 ± 0.3
Total	255	276.7 ± 1.4	117	128.4 ± 1.1	16	17.6 ± 0.4

Table 5.2: *Search for anomalous production of four-jet events: Numbers of selected data and expected background events before and after the* W^+W^- *veto (cut 8) and after the mass selection (cut 9) corresponding to a dijet mass sum of 105 GeV for the jet combination with the smallest dijet mass difference. Errors are statistical only. No* W^+W^- *veto has been applied to the 130 − 136 GeV data.*

To achieve good sensitivity for all ΔM less than 30 GeV, we use two separate mass selections, one relevant for unequal masses and one for equal masses. In both selections, when searching for a signal with a hypothetical sum of masses, M_0, the range $M_0 \pm 2\sigma_M$ is used, where σ_M is 2.0 GeV at $\sqrt{s}$ =130 − 136 GeV and 3.0 GeV for higher energies. The resolution σ_M varies only slowly with M and ΔM.

(9) For unequal masses ($\Delta M > 5$ GeV), the event is selected if either the jet association with the smallest mass difference or the one with the intermediate mass difference has a mass sum M in the range $M_0 \pm 2\sigma_M$.

For nearly equal masses ($\Delta M < 5$ GeV), better sensitivity is obtained when considering only the jet association with the smallest mass difference.

Table 5.2 presents the number of observed events and the SM expectations before and after the W^+W^- veto. The number of observed events is consistent with the SM expectation at all centre-of-mass energies both before and after the mass selection.

Table 5.3 shows the signal efficiencies for various combinations of (M_X,M_Y) together with the predicted background and the number of observed events after all cuts.

Figure 5.2 shows the distribution of M for the jet association with the smallest ΔM

(M_X, M_Y)	130 − 136 GeV			161 GeV		
(GeV)	Efficiency (%)	Background	Data	Efficiency (%)	Background	Data
(50,50)	30.6 ± 1.5	3.2 ± 0.3	3	38.0 ± 2.2	2.4 ± 0.1	3
(40,60)	29.6 ± 2.0	5.6 ± 0.4	6	35.8 ± 2.1	4.2 ± 0.2	3
(55,55)	29.0 ± 2.0	3.1 ± 0.3	4	37.4 ± 1.0	3.0 ± 0.1	1
(50,60)	38.4 ± 1.5	5.6 ± 0.4	7	42.0 ± 2.2	5.0 ± 0.2	1
(40,70)	23.0 ± 1.9	5.6 ± 0.4	7	34.8 ± 2.1	5.0 ± 0.2	1
(60,60)	26.2 ± 1.4	3.2 ± 0.3	3	39.0 ± 2.2	2.8 ± 0.1	0
(50,70)	30.2 ± 2.1	5.6 ± 0.4	4	41.2 ± 2.2	4.8 ± 0.2	1
(60,70)	24.2 ± 1.9	2.2 ± 0.2	4	34.2 ± 2.1	4.7 ± 0.2	2
(50,80)	13.1 ± 1.1	2.2 ± 0.2	4	32.8 ± 2.1	4.7 ± 0.2	2
(70,70)	—	—	—	26.6 ± 2.0	2.0 ± 0.1	2
(60,80)	—	—	—	33.8 ± 2.1	4.4 ± 0.2	3
(M_X, M_Y)	172 GeV			183 GeV		
(GeV)	Efficiency (%)	Background	Data	Efficiency (%)	Background	Data
(50,50)	31.0 ± 1.5	2.5 ± 0.1	4	19.4 ± 1.8	4.8 ± 0.2	4
(40,60)	24.6 ± 1.9	3.2 ± 0.1	5	16.3 ± 1.6	5.6 ± 0.2	6
(55,55)	34.4 ± 1.0	3.6 ± 0.2	5	31.6 ± 2.1	12.4 ± 0.3	9
(50,60)	32.6 ± 1.5	5.1 ± 0.2	6	22.2 ± 1.9	16.2 ± 0.3	12
(40,70)	23.0 ± 1.3	5.1 ± 0.2	6	18.0 ± 1.7	16.2 ± 0.3	12
(60,60)	33.0 ± 1.5	3.7 ± 0.2	9	32.6 ± 2.1	17.1 ± 0.4	20
(50,70)	34.4 ± 2.1	5.5 ± 0.2	11	23.9 ± 1.9	23.5 ± 0.4	30
(60,70)	33.6 ± 1.5	5.5 ± 0.2	6	32.2 ± 2.1	28.2 ± 0.4	24
(50,80)	28.8 ± 1.4	5.5 ± 0.2	6	23.2 ± 1.9	28.2 ± 0.4	24
(70,70)	29.9 ± 1.4	3.3 ± 0.1	1	31.2 ± 2.1	20.7 ± 0.4	20
(60,80)	31.0 ± 2.1	6.0 ± 0.2	4	27.7 ± 2.0	32.3 ± 0.5	28

Table 5.3: *Search for anomalous production of four-jet events: Signal selection efficiencies, numbers of expected background and selected data events for various mass combinations after the mass selection (cut 9). Errors are statistical only. Dashes indicate kinematically forbidden mass combinations.*

and for the combined distribution (two entries per event) corresponding to the smallest and intermediate ΔM, summed over all centre-of-mass energies. Globally, the distributions show consistency between the data and the SM background prediction. In particular, there is no excess in the vicinity of $M \approx 105$ GeV.

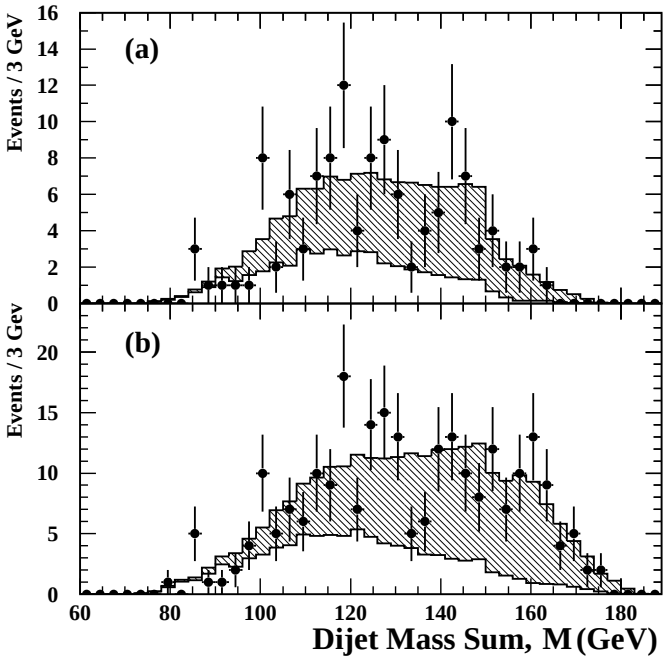

Figure 5.2: *Search for anomalous production of four-jet events at $\sqrt{s} = 130 - 183$ GeV: Dijet mass sum distributions for the jet combinations with the (a) smallest and (b) smallest and intermediate dijet mass difference. Selected data events are shown as dots with error bars, the SM two- and four-fermion background estimates as open and hatched histograms, respectively. All Monte Carlo samples are normalized to the integrated luminosity of the data.*

5.3.1 Systematic Effects

The signal selection efficiencies are subject to a total systematic error of 9%, which includes an allowance for the final state to contain any composition of quark flavours and uncertainties in modelling heavy hadron decays, 4%; the uncertainty on the simulation of

the decay with regards to fragmentation and hadronization, 0.3%; the modelling of the cut variables, 5%; and the limited Monte Carlo statistics, typically 6%.

The total relative uncertainty on the residual background is 13%. This error includes the uncertainty on the modelling of the hadronization process, 4%, estimated by comparing the predictions of different MC generators; on the prediction of the four-jet rate and the $W^{\pm}$ production cross-section, 5%; and on the modelling of the cut variables, 10%. The error due to the limited Monte Carlo statistics is added in quadrature to this uncertainty. The systematic errors on the luminosity measurements range from 0.5% to 1.4%, depending on the centre-of-mass energy.

The uncertainty due to the imperfect modelling of the selection variables is estimated by shifting each cut value by an amount corresponding to the difference between the data and the SM Monte Carlo distributions. In case of two-sided distributions the difference of the mean values of the two distributions is used, while in case of single-sided distributions, the RMS ratio of the two distributions is used to scale the cut position.

5.4 Cross-Section Upper Limits

This analysis is used to obtain upper limits for the cross-section of a possible signal process $e^+e^- \to XY \to$ four jets, in the presence of background from SM processes, using Poisson statistics and incorporating systematic uncertainties as described in the first part of Section 3.2.9 using the method of [62]. The process $e^+e^- \to h^0A^0$ is used to model the signal selection efficiencies.

To obtain upper limits at the 95% CL on the production cross-section a mass window of $M \pm 2\sigma_M$ is scanned across the distribution of the dijet mass sum in small steps. To account for a possible discrepancy between the mass scale of the data and the Monte Carlo in a conservative manner, the mass window is displaced by ± 0.5 GeV at each scan point. The largest data count in any of the three windows including the nominal one and the smallest background estimation in any of the three windows are used to compute the limit. The result of this *sliding mass window scan* is shown in Figure 5.3 for the jet combination with the smallest ΔM.

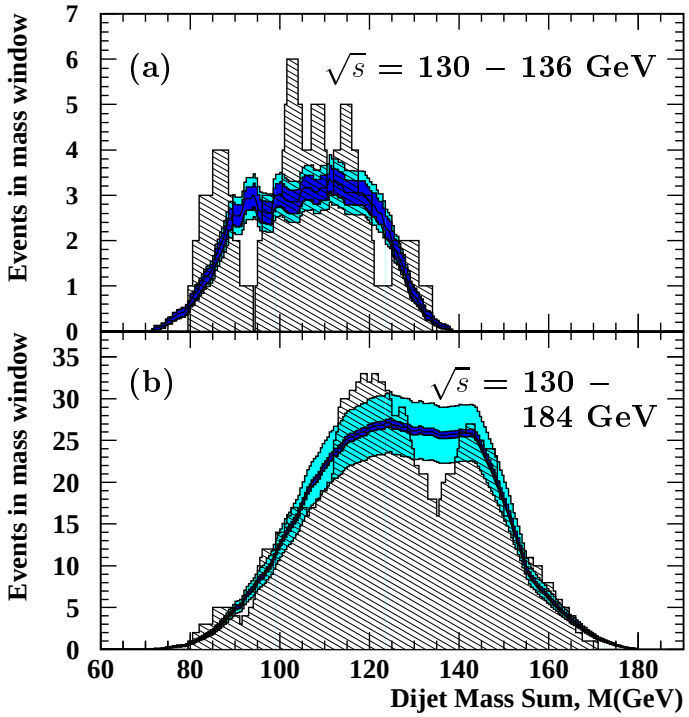

Figure 5.3: *Search for anomalous production of four-jet events: Results of the sliding mass window scan using a step size of 0.5 GeV and a mass window of $\pm 2\sigma_M$ after the W^+W^- veto for the jet combination with the smallest dijet mass difference at (a) $\sqrt{s} = 130 - 136$ GeV and (b) $\sqrt{s} = 130 - 183$ GeV combined. The observed event counts for the given mass hypothesis are shown as hatched histograms and the SM background estimates as solid histograms with error bands. The dark and light grey bands indicate the statistical and systematical errors, respectively. Note that values in neighbouring bins are strongly correlated.*

When results at different centre-of-mass energies are combined, the hypothetical production cross-section is assumed to vary as β^3/s. The cross-section limits are presented separately using the data collected at $\sqrt{s} = 130 - 136$ GeV and using all data, $\sqrt{s} = 130 - 184$ GeV, combined. Limits on the cross-section from the combined data sample are computed both at $\sqrt{s} = 133$ GeV and at $\sqrt{s} = 183$ GeV. The resulting upper limits at the 95% CL, are shown in Figure 5.4, as function of the mass sum $M(\equiv M_X + M_Y)$, for $\Delta M = 0$ and $\Delta M \leq 30$ GeV. These limits are independent of the flavour of the quarks from

the decay of the hypothesized particles and are valid for X and Y being scalars produced predominantly in an s-channel process.

ALEPH has quoted a cross-section of 3.1±1.7 pb [79] corresponding to their total number of excess events. From our searches, at the dijet mass sum of 105 GeV for dijet mass diferences between 0 and 30 GeV, the cross-section upper limit at the 95% CL, scaled to 133 GeV, is $2-3$ pb using only the data collected at $\sqrt{s} = 130-136$ GeV and $0.35-0.55$ pb using all data, in a clear disagreement with the ALEPH observation.

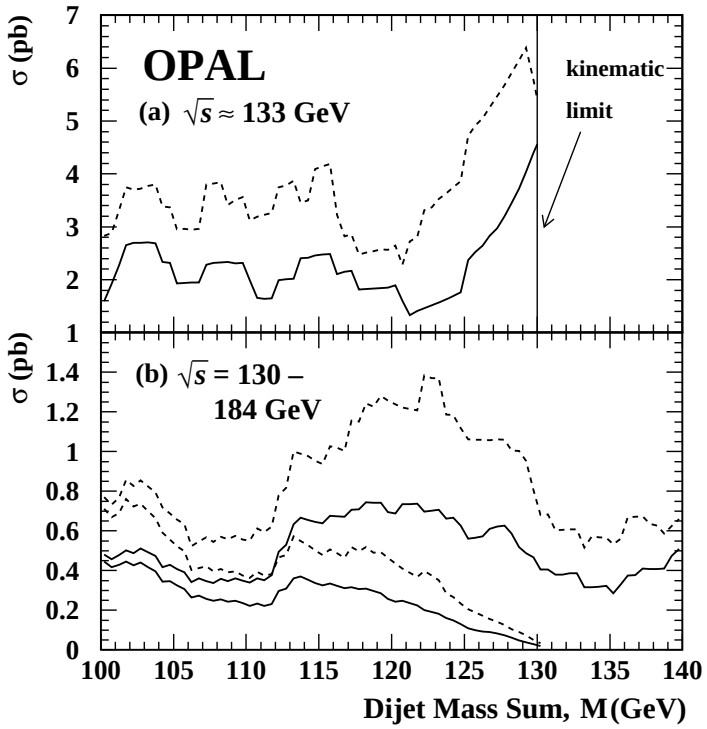

Figure 5.4: *Search for anomalous production of four-jet events: Upper limits at the 95% CL on the production cross-section of a possible signal as a function of the dijet mass sum, M, computed using the data collected at (a) $\sqrt{s} = 130-136$ GeV and (b) $\sqrt{s} = 130-184$ GeV combined. Limits for dijet mass differences of $\Delta M = 0$ and $\Delta M \leq 30$ GeV are shown as solid and dashed lines, respectively. For the combination of the data collected at $\sqrt{s} = 130-184$ GeV, a cross-section that varies as β^3/s is assumed and the results are scaled to $\sqrt{s} = 133$ GeV (lines that end near $M = 130$ GeV) and $\sqrt{s} = 183$ GeV (lines that extend to larger M).*

5.5 Conclusions

Following the ALEPH observation of a large excess of four-jet events with dijet mass sum around 105 GeV at $\sqrt{s}$ =130 − 136 GeV, an analysis has been performed using OPAL data collected in e^+e^- collisions at centre-of-mass energies of 130 − 184 GeV. The process $e^+e^- \to h^0A^0$ is used to estimate the signal selection efficiencies. No significant excess of four-jet events with dijet mass sum close to 105 GeV, or any other value between 60 and 160 GeV, has been observed in any of the data samples separately or combined. Our observations are consistent with the SM predictions. Limits for the cross-section of a hypothetical process $e^+e^- \to XY \to$ four jets are given as a function of the dijet mass sum M and the dijet mass difference ΔM. The upper limits obtained for dijet mass sums near 105 GeV are much below the excess reported in 1995 by ALEPH.

ALEPH has also analysed the new data at centre-of-mass energies between 130 and 184 GeV collected in 1997 and did not confirm the previously reported excess [90].

Chapter 6

Search for Supersymmetric Particles in *R*-parity Violating Decays

6.1 Introduction

Most of the theoretical and experimental studies of MSSM are performed assuming R-parity conservation. Recalling that R-parity is $R_p = +1$ for ordinary particles and $R_p = -1$ for their supersymmetric partners, its conservation implies that supersymmetric particles, also called sparticles, are always produced in pairs and decay through cascade processes to Standard Model particles and to the lightest supersymmetric particle (LSP), which is regarded to be stable. If the LSP is neutral and weakly interacting, it escapes detection resulting in sizable missing energy. This is often the characteristic signature of the supersymmetric R-parity conserving decays, since in most of the parameter space the lightest neutralino or one of the sneutrinos is the LSP.

In this work, the possible manifestations of R-parity violation (RPV) in supersymmetric particle decays are studied. This is of major interest, since there is no theoretical or experimental argument excluding RPV and the branching ratios of some R-parity violating decay modes of sparticles can be comparable or even larger than the R-parity conserving ones.

Let us recall from Section 1.2.1 that R-parity violating interactions with the MSSM particle content are described, with the assumption that the $\mu'_i L_i H_2$ term becomes zero by a rotation of the lepton field, by the gauge invariant superpotential including the following Yukawa coupling terms:

$$w_{RPV} = \lambda_{ijk} L_i L_j E^c_k + \lambda'_{ijk} L_i Q_j D^c_k + \lambda''_{ijk} U^c_i D^c_j D^c_k, \tag{6.1}$$

where i, j, k are the generation indices of the superfields L, Q, E, D and U. L and Q are lepton and quark left-handed doublets, and E^c, D^c and U^c are right-handed singlet charge-conjugate superfields for the charged leptons, down- and up-type quarks, respectively. μ'_i is a bilinear coupling and H_2 is the up-type Higgs field. The λ_{ijk} couplings are antisymmetric in i and j and non-vanishing for $i < j$, while the λ''_{ijk} couplings are antisymmetric in j and k and non-vanishing for $j < k$, therefore at least two different generations are coupled in the purely leptonic or purely hadronic vertices. These symmetries make a total of 9 + 27 + 9 = 45 parameters in addition to those of the R-parity conserving MSSM.

There are several experimental upper bounds[1] on the R-parity violating Yukawa couplings, λ, $\lambda'$and λ''. Most of the upper limits on the couplings are of $\mathcal{O}(10^{-2})$, but there are some more stringent limits of $\mathcal{O}(10^{-6})$ on some individual couplings [91]. The simultaneous presence of the λ' (L-violating) and λ'' (B-violating) couplings are forbidden, since the experimental non-observation of proton decay places a strong bound on $\lambda'_{11k} \times \lambda''_{11k} < 10^{-22}$ for $k = 1, 2$ [92], or a more general limit gives $\lambda'_{ijk} \times \lambda''_{lmn} < 10^{-10}$ [93].

As a consequence of RPV sparticles can be singly produced, for which limits are given by the OPAL Collaboration in [94]. For couplings smaller than $\mathcal{O}(10^{-5})$ the supersymmetric particles have sufficiently long lifetime not to decay in the detector. These topologies are treated by OPAL in [95]. For larger couplings the LSP promptly decays within the detector, yielding different experimental signatures compared to R-parity conservation. Results for pair-produced sparticles decaying via R-parity violating couplings are reported by the ALEPH and L3 Collaborations [96, 97], and a search [98, 99] using the OPAL detector is presented here.

[1] All quoted limits are given for a sparticle mass of 100 GeV.

6.1.1 Production and Decay

In this search only the pair production of supersymmetric particles is considered involving s-channel γ and Z^0 exchange and, in the case of gauginos[2] and first generation sfermions, also t-channel exchange processes as shown in Figure 6.1. The interference between s- and t-channel processes is taken into account.

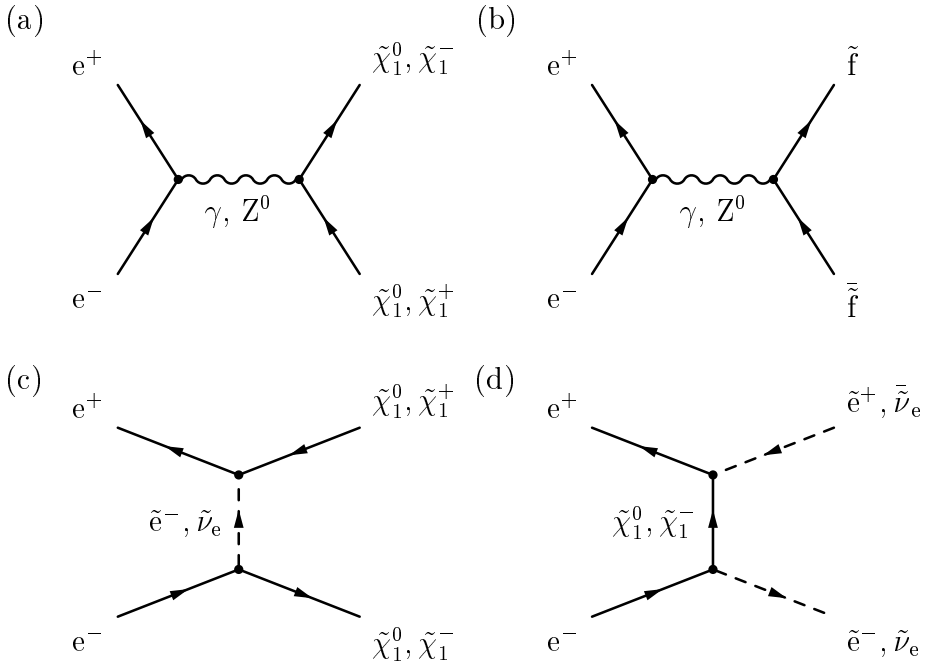

Figure 6.1: *Feynman diagrams for pair-production of supersymmetric particles.*

It is always assumed in this work that only one R-parity violating coupling is non-zero. Among the sparticle decay modes considered, we can distinguish two scenarios called direct and indirect decays. The direct decay of gauginos results in a fermion and a virtual sfermion which decays in turn via R-parity violating transition, Figure 6.2(a). The indirect decay mode of charginos we consider starts with the production of a neutralino and a virtual $W^{\pm}$ resulting in five fermions, Figure 6.2(b).

In the direct decay of sfermions into SM particles, Figure 6.3(a), the sfermion is con-

[2]In the following we refer to the gaugino-higgsino mixture mass eigenstates, called charginos and neutralinos, as gauginos.

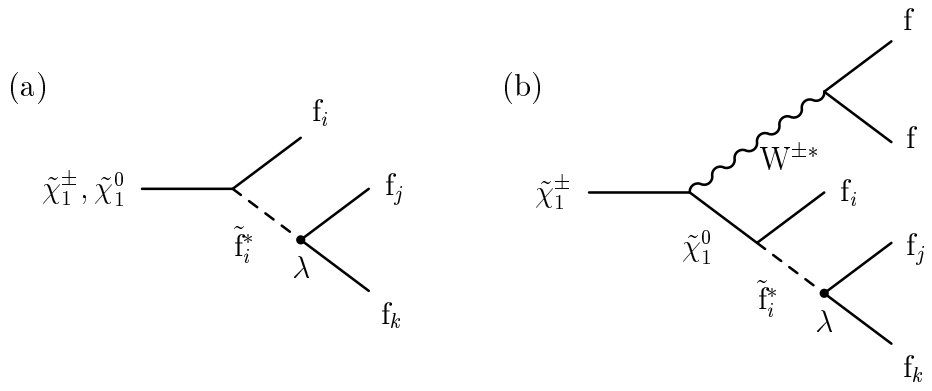

Figure 6.2: *Feynman diagrams for (a) direct and (b) indirect decays of gauginos involving R-parity violating transitions.* λ *stands for* λ_{ijk}, $\lambda^{'}{}_{ijk}$ *or* $\lambda^{''}{}_{ijk}$.

sidered to be the LSP, so no R-parity conserving modes contribute. In the indirect decay of sfermions through $\tilde{\chi}_1^0$, Figure 6.3(b), the lightest neutralino is treated as the LSP and is assumed to decay via an R-parity violating coupling.

Cascade decays through other particles than the lightest neutralino are not investigated.

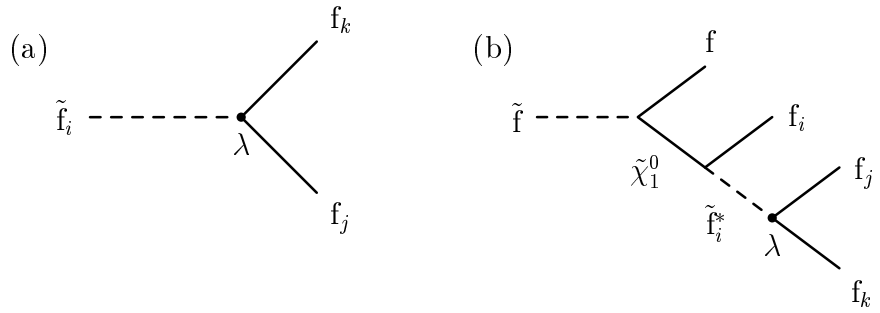

Figure 6.3: *Feynman diagrams for (a) direct and (b) indirect decays of sfermions involving R-parity violating transitions.* λ *stands for* λ_{ijk}, $\lambda^{'}{}_{ijk}$ *or* $\lambda^{''}{}_{ijk}$.

We present searches using fully hadronic final states with or without missing energy, resulting from pair production of sparticles followed by decays through the $\lambda'_{ijk} L_i Q_j D^c_k$ and $\lambda''_{ijk} U^c_i D^c_j D^c_k$ operators. The decay modes involved are the following:

charginos: $\tilde{\chi}^+ \to \nu_i u_j \bar{d}_k$ and $\tilde{\chi}^+ \to \bar{\nu}_i \bar{d}_j u_k$,

neutralinos: $\tilde{\chi}^0 \to \nu_i d_j \bar{d}_k$ and $\tilde{\chi}^0 \to \bar{\nu}_i \bar{d}_j d_k$,

charged sleptons: $\tilde{\ell}^{-}_{iL} \to \bar{u}_j d_k$,

sneutrinos: $\tilde{\nu}_{iL} \to \bar{d}_j d_k$ and $\tilde{\nu} \to \tilde{\chi}^0 \nu$ followed by $\tilde{\chi}^0 \to \nu_i d_j \bar{d}_k$ or $\tilde{\chi}^0 \to \bar{\nu}_i \bar{d}_j d_k$,

squarks: $\tilde{u}_{iR} \to \bar{d}_j \bar{d}_k$, $\tilde{d}_{jR} \to \bar{u}_i \bar{d}_k$ and $\tilde{d}_{kR} \to \bar{u}_i \bar{d}_j$.

Note that only left-handed sleptons and right-handed squarks can decay directly into two quarks.

In the next sections four analyses are described, which are then combined with other searches to place limits on the sparticle masses and constrain the parameter space of the MSSM:

(A) Final states without missing energy originate from

- direct decays of charged sleptons $\tilde{\ell}^{+}\tilde{\ell}^{-} \to$ qqqq and sneutrinos $\tilde{\nu}\bar{\tilde{\nu}} \to$ qqqq through $\lambda^{'}$ couplings;
- direct decays of squarks $\tilde{\mathrm{q}}\bar{\tilde{\mathrm{q}}} \to$ qqqq through $\lambda^{''}$ couplings.

(B) Final states with missing energy originate from

- direct decays of charginos $\tilde{\chi}^{+}\tilde{\chi}^{-} \to \nu$qq$\nu$qq and neutralinos $\tilde{\chi}^0\tilde{\chi}^0 \to \nu$qq$\nu$qq through $\lambda^{'}$ couplings;
- indirect decays of sneutrinos $\tilde{\nu}\bar{\tilde{\nu}} \to \nu\tilde{\chi}^0\bar{\nu}\tilde{\chi}^0 \to \nu\nu$qq$\nu\nu$qq through $\lambda^{'}$ couplings.

In all searches the sparticles are assumed to decay promptly, which implies that the analyses are sensitive to couplings larger than $\mathcal{O}(10^{-5})$, estimated using the decay width of the sparticles as given in [100].

6.2 Data and Monte Carlo Simulation

In this work data collected by the OPAL detector between 1995 and 1997 at centre-of-mass energies of $130 - 183$ GeV are used to search in the four-jet final state and data collected in 1997 at $\sqrt{s} = 183$ GeV are used to search in the four-jet final state with missing energy, with the same luminosities as listed in Table 4.1.

The main background for all selections comes from quark pair events with or without

initial state photon radiation and from four-fermion production processes, predominantly W^+W^- production. We have used the SM Monte Carlo samples described in Section 3.1.

6.2.1 Signal Samples for the Four-Jet Final State

The SUSYGEN Monte Carlo generator is used to simulate pair production of sfermions followed by decays leading to four-jet final states as described in Section 6.1.1.

At $\sqrt{s} = 172$ GeV electron-sneutrino, smuon and first generation squark samples are generated. Sneutrino events at masses of 50, 70 and 85 GeV with λ'_{111} coupling and at a mass of 70 GeV with λ'_{133} coupling are produced. Smuon samples are generated at masses of 45, 55 and 70 GeV with λ'_{211} coupling. First generation up-type squark events are produced at a mass of 70 GeV with λ'_{112} coupling.

At $\sqrt{s} = 183$ GeV first generation squark, selectron and electron-sneutrino samples are generated at masses of 45, 60, 75, 80 and 90 GeV, smuon samples at masses of 60 and 75 GeV and muon-sneutrino samples at masses of 60 and 75 GeV or 45 and 80 GeV depending on the λ' coupling. The Yukawa couplings of λ''_{112}, λ''_{123}, λ'_{x21} and λ'_{x23} are tested, where the $x = 1, 2$ index corresponds to the slepton flavour. This choice of couplings allows to test the dependence on the final state quark flavours.

Furthermore, Monte Carlo samples of charged Higgs boson pair-production followed by a decay into four-jet final state, as described in Section 4.2, are also used to estimate selection efficiencies, to prevent the need for generating a large number of Monte Carlo samples. Studies to check for systematic effects are done, as explained later, in each case where these samples are considered.

6.2.2 Signal Samples for the Four-Jet Final State with Missing Energy

Signal selection efficiencies at $\sqrt{s} = 183$ GeV are estimated using the SUSYGEN generator to simulate pair production of charginos, neutralinos and sneutrinos followed by decays leading to four-jet final states with missing energy as described in Section 6.1.1.

Gaugino samples are produced at masses of 45, 70 and 90 GeV with the common scalar mass $m_0 = 1$ TeV, and for systematic checks at a mass of 70 GeV with $m_0 = 48.4$ GeV, which is the smallest value still allowed from the limits on sneutrino mass [101] and OPAL limits on slepton masses [102] in R-parity conserving modes. Neutralino samples at a mass of 30 GeV are also generated, as no direct mass limit exists from LEP1.

Only first generation sneutrino samples are generated, since the theoretical production cross-section is expected to be very small for the other flavours due to the absence of t-channel production. Events are produced at masses of 45, 70 and 90 GeV with $\Delta m = m_{\tilde{\nu}} - m_{\tilde{\chi}_1^0} = \frac{1}{2} m_{\tilde{\nu}}$ and for systematic checks at a mass of 90 GeV with $\Delta m = 5$ GeV.

In all cases, the Yukawa couplings of λ'_{121} and λ'_{123} are probed. The first index corresponds to the flavour of the unmeasured neutrino, and the last two to the quark generations allowing to study the dependence on the final state quark flavours.

6.3 Four-Jet Final State

The pair production of sleptons in the process $e^+e^- \to \tilde{\ell}\bar{\tilde{\ell}} \to qqqq$ leads to four well-separated hadronic jets with large visible energy. The pair production of squarks, strictly speaking, results in a final state with six jets, since they are coloured objects and expected to hadronize. However from the six jets the two spectator jets have small energy, at least for heavy squarks, and therefore it is still possible to reconstruct squark pair events into four jets.

For sfermion searches in R-parity violating decays into quarks we have reused the analyses developed to search for pair-produced charged Higgs bosons in the four-jet topology.

6.3.1 Analysis of Data Collected at $\sqrt{s} = 130 - 172$ GeV

Sfermions and charged Higgs bosons are both scalar objects with different electroweak couplings but similar angular distributions. Studying their production leading to a given final state topology in the same experimental environment using the same event selection

Physics		Signal selection efficiencies (%) for various scalar particle masses								
Process		40 GeV	45 GeV	50 GeV	55 GeV	60 GeV	65 GeV	70 GeV	75 GeV	85 GeV
H^+H^-		24.6±1.9	40.4±2.2	42.2±2.2	39.6±2.2	39.0±2.0	29.4±2.0	31.2±2.1	20.0±1.8	—
$\tilde{\mu}^+\tilde{\mu}^-$	λ'_{211}	—	41.1±1.6	—	39.4±1.5	—	—	32.8±1.5	—	—
$\tilde{\nu}_e\bar{\tilde{\nu}}_e$	λ'_{111}	—	—	41.8±1.6	—	—	—	28.2±1.4	—	6.2±0.8
	λ'_{133}	—	—	—	—	—	—	29.9±1.5	—	—
$\tilde{u}\bar{\tilde{u}}$	λ'_{112}	—	—	—	—	—	—	36.2±1.5	—	—

Table 6.1: *Sfermion search at $\sqrt{s}$ = 172 GeV: Comparison of signal selection efficiencies for charged Higgs boson, smuon, selectron and first generation squark pair-production for various masses. The Yukawa coupling involved in the sfermion decay is given. Errors are statistical only. Dashes indicate masses which are not simulated.*

one expects very similar signal selection efficiencies, and in the absence of discovery may use the same search results to set limits on their production cross-section.

However, there are two main physics points which may result in significant differences:

- First generation sleptons can be produced in t-channel exchange processes and therefore may have different angular distributions.
- Squarks are coloured objects and expected to hadronize. Jets originating from their decays may have different properties than the ones coming from SM sources [103]. Studying different event generators we have found that jets from squark decays tend to be narrower.

To check the hypothesis of similar search sensitivity, signal selection efficiencies using Monte Carlo samples of charged Higgs boson, smuon, electron-sneutrino and first generation squark events are compared. They are given in Table 6.1 using the selection described in Section 4.4.1 at $\sqrt{s}$ = 172 GeV for various scalar masses. All efficiencies agree within the available statistics except the one for the squark sample which is about two standard deviation higher than the corresponding charged Higgs boson efficiency.

This result can be understood by considering that

- the analysis do not rely heavily on angular distributions which could hurt the efficiency for electron-sneutrino (and selectron) production;
- the narrower jets of squark pair production result in a gain of efficiency when selecting four jet events by y_{34} and give somewhat more accurately measured jet angles leading to better kinematic fit performance.

After this check one can use the efficiencies calculated for the charged Higgs boson samples to establish limits on sfermion pair production.

A final selection on mass is applied, since the statistical method used in supersymmetric particle searches within OPAL [106] does not handle the experimental mass distributions. Recalling that the mass of the scalar particle can be reconstructed with a resolution of 0.6 $-$ 1.2 GeV using a kinematic fit, a mass window of $\pm$2 GeV at $\sqrt{s} = 130 - 136$ GeV and $\pm$2.4 GeV at $\sqrt{s} = 161 - 172$ GeV is opened around the mass considered. The resulting numbers of selected data and expected SM background events together with the signal selection efficiencies are given in Table 6.2 for various scalar particle masses.

6.3.2 Slepton Search at $\sqrt{s} = 183$ GeV

Using the same philosophy as at lower energies, the analysis developed for charged Higgs boson searches described in Section 4.4.2 is reused to search for slepton pair production followed by R-parity violating decay into quarks. However, in the likelihood selection we take advantage of the difference in angular distributions between the signal and the severe W^+W^- background. Since first generation sleptons can be produced in t-channel exchange processes, the signal reference histograms are produced separately for selectron and electron-sneutrino searches using dedicated Monte Carlo samples. For non-first generation sleptons, the charged Higgs boson reference histograms and results are used and the possible systematic differences in signal selection efficiency are tested using dedicated Monte Carlo samples.

The likelihood (LH) cut is placed at 0.5, 0.55 and 0.6 for selectrons, electron-sneutrinos and non-first generation sleptons, respectively. The number of observed data events together with the SM expectation is given in Table 6.3. In Figure 6.4 the likelihood and the

$\sqrt{s}$	Scalar particle mass							
(GeV)	40 GeV	45 GeV	50 GeV	55 GeV	60 GeV	65 GeV	70 GeV	75 GeV
Number of selected data events								
130	1	0	0	0	0	—	—	—
136	1	0	1	0	0	—	—	—
161	1	1	1	0	0	0	0	—
172	0	0	0	3	2	0	0	0
Number of events expected from SM processes								
130	0.17±0.07	0.22±0.07	0.13±0.05	0.22±0.07	0.17±0.07	—	—	—
136	0.16±0.06	0.16±0.06	0.22±0.08	0.29±0.08	0.41±0.10	—	—	—
161	0.55±0.06	0.67±0.06	0.69±0.06	0.84±0.07	0.84±0.07	0.76±0.06	0.56±0.05	—
172	0.23±0.03	1.06±0.06	1.01±0.06	1.11±0.06	1.08±0.06	1.17±0.06	1.14±0.06	0.94±0.05
Signal selection efficiency (%)								
130	21.4±1.8	24.6±1.9	24.2±1.9	19.8±1.8	14.2±1.6	—	—	—
136	20.8±1.8	26.4±2.0	24.6±1.9	17.0±1.7	16.6±1.7	—	—	—
161	27.6±1.8	32.4±2.1	35.4±2.1	32.0±2.1	27.4±2.0	22.0±1.9	19.4±1.8	—
172	19.0±1.8	32.2±2.1	34.0±2.1	30.6±2.1	30.6±2.1	21.8±1.8	22.2±1.9	10.8±1.4

Table 6.2: *Sfermion search at $\sqrt{s} = 130 - 172$ GeV: Numbers of selected data and expected background events together with the signal selection efficiencies for various masses after the mass selection. Errors are statistical only. Dashes indicate masses which are not simulated.*

	Data	Background	4f contribution
Before LH selection	454	445.4±2.3	76.6%
Selectron (LH>0.5)	55	55.4±0.8	87.1%
Electron-sneutrino (LH>0.55)	41	49.1±0.7	86.0%
Other sleptons (LH>0.6)	50	48.8±0.7	81.5%

Table 6.3: *Slepton search at $\sqrt{s} = 183$ GeV: Numbers of selected data and expected background events together with the contribution of four-fermion processes before and after the likelihood selection. Errors are statistical only. Note that different signal reference histograms are used in the three selections.*

Physics		Scalar particle mass									
Process		45 GeV	50 GeV	55 GeV	60 GeV	65 GeV	70 GeV	75 GeV	80 GeV	85 GeV	90 GeV
Number of selected data events											
H^+H^-		2	1	5	7	1	5	8	17	2	1
$\tilde{e}^+\tilde{e}^-$		1	—	—	4	—	—	9	25	—	2
$\tilde{\nu}_e\bar{\tilde{\nu}}_e$		0	—	—	5	—	—	8	12	—	2
Number of events expected fom SM processes											
H^+H^-		1.00±0.11	2.77±0.18	4.29±0.22	5.59±0.25	5.52±0.25	4.48±0.23	4.47±0.22	14.21±0.40	2.39±0.16	1.26±0.12
$\tilde{e}^+\tilde{e}^-$		1.05±0.11	—	—	6.25±0.27	—	—	6.55±0.27	16.46±0.43	—	1.38±0.12
$\tilde{\nu}_e\bar{\tilde{\nu}}_e$		0.68±0.09	—	—	7.28±0.29	—	—	8.53±0.31	20.98±0.49	—	0.91±0.10
Signal selection efficiency (%)											
H^+H^-		—	27.8±2.2	28.6±2.2	31.2±2.2	23.4±2.2	17.8±2.1	11.4±1.9	7.2±1.6	7.8±1.6	6.2±1.5
$\tilde{\mu}^+\tilde{\mu}^-$	λ'_{212}	—	—	—	29.9±1.4	—	—	12.0±1.0	—	—	—
	λ'_{223}	—	—	—	28.7±1.4	—	—	9.4±0.9	—	—	—
$\tilde{\nu}_\mu\bar{\tilde{\nu}}_\mu$	λ'_{212}	—	—	—	28.6±1.4	—	—	11.2±1.0	—	—	—
	λ'_{223}	11.4±1.0	—	—	—	—	—	—	6.4±0.8	—	—
$\tilde{e}^+\tilde{e}^-$	λ'_{112}	4.8±0.7	—	—	31.2±1.5	—	—	11.7±1.0	7.5±0.8	—	8.2±0.9
	λ'_{123}	5.5±0.7	—	—	34.3±1.5	—	—	11.3±1.0	7.4±0.8	—	7.3±0.8
$\tilde{\nu}_e\bar{\tilde{\nu}}_e$	λ'_{112}	19.0±1.2	—	—	27.0±1.4	—	—	11.8±1.0	9.7±0.9	—	9.0±0.9
	λ'_{123}	17.5±1.2	—	—	27.7±1.4	—	—	13.3±1.1	9.4±0.9	—	7.7±0.8

Table 6.4: *Slepton search at $\sqrt{s}$ = 183 GeV: Numbers of selected data and expected background events together with the signal selection efficiencies after the mass selection for the three different sets of likelihood reference histograms for various signal processes and scalar particle masses. The Yukawa coupling involved in the slepton decay is given. Errors are statistical only. Dashes indicate masses that are not simulated.*

mass distributions are shown in the three different selections.

As a final selection a mass window of $\pm 2\sigma_m$ is opened around the slepton mass considered, where σ_m is the mass resolution varying between 0.6 and 1.6 GeV depending on the sparticle species and mass. The resulting numbers of selected data and expected background events together with the signal selection efficiencies are given in Table 6.4 for various signal processes and scalar particle masses.

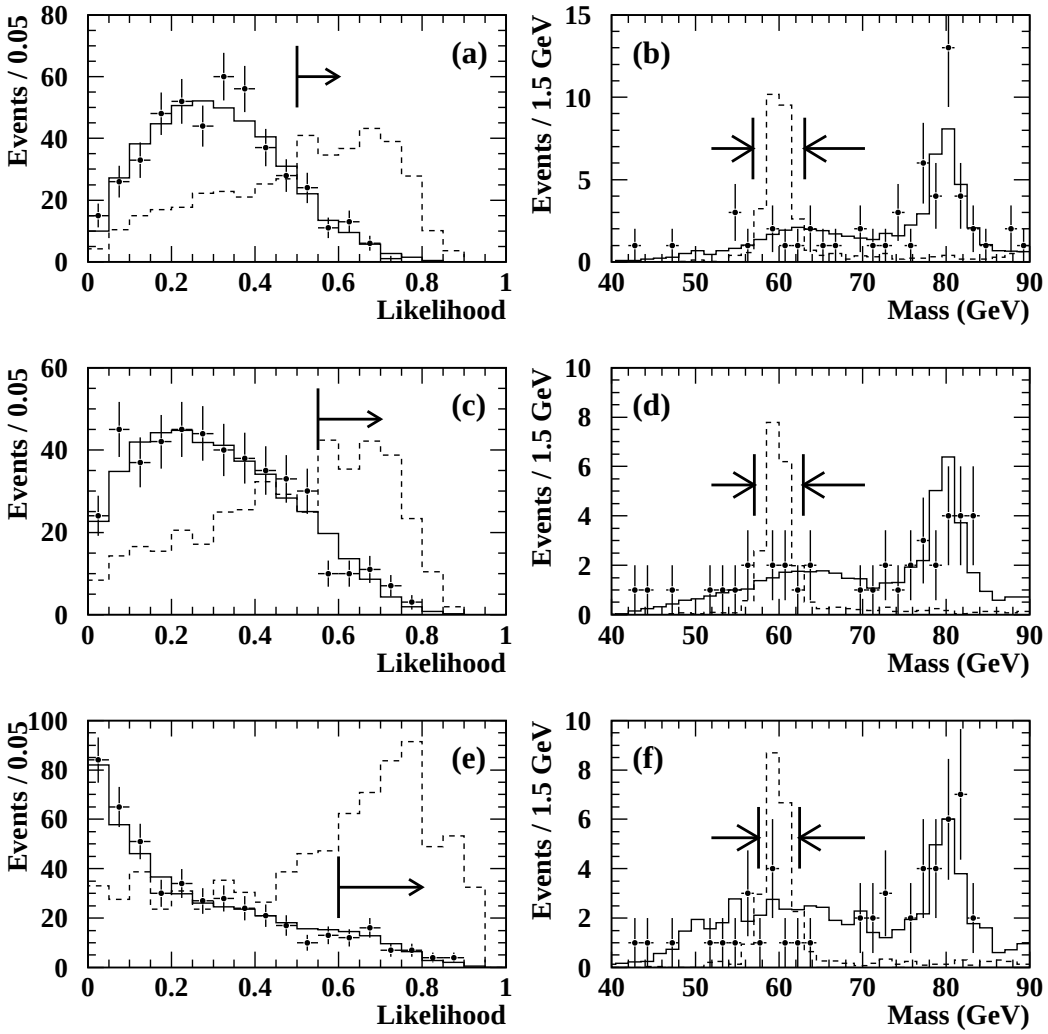

Figure 6.4: *Slepton search at $\sqrt{s} = 183$ GeV: Distributions of likelihood outputs (left) and invariant masses using a five-constraint kinematic fit (right) in the selectron (a,b), electron-sneutrino (c,d) and non-first generation slepton (e,f) searches. Selected data events are shown as dots with error bars, the SM background estimates as solid histograms and simulated signals of 60 GeV mass as dashed histograms. Background samples are normalized to the integrated luminosity of the data, while the signal normalization is arbitrary. The arrows indicate the positions of the likelihood cuts and the mass windows for 60 GeV sparticles.*

6.3.3 Squark Search at $\sqrt{s} = 183$ GeV

To search for squark pair production we have adapted the analysis of Section 4.4.2. The signal reference histograms are generated using dedicated squark samples and to take advantage of the fact that jets originating from squark decays are expected to be narrower than the ones coming from SM sources, in addition to the five input variables used in the charged Higgs boson and slepton searches, two new variables are introduced in the likelihood selection:

- the highest jet mass;
- the smallest jet thrust.

In Figure 6.5 the new likelihood variables are shown together with the likelihood output, which is required to be greater than 0.95. After this selection 7 events are selected in the data sample, while 8.8 ± 0.3 (statistical error) is expected from SM processes. Like in the slepton searches the background is dominated by four-fermion processes, accounting for 93.3% of the total background.

The dijet mass resolution σ_m using a five-constraint kinematic fit is $0.45 - 1.2$ GeV depending on the squark mass and the λ'' coupling. A systematic shift of the reconstructed mass (up to +2.2 GeV for squark masses of 45 GeV) is observed, which is taken into account when applying the $\pm 2\sigma_m$ mass window. The invariant mass distribution of the selected events is shown in in Figure 6.5(d). The numbers of selected data and expected background events together with the signal selection efficiencies within the mass windows are given in Table 6.5.

6.3.4 Systematic Effects

No excess of events is observed in the data over the SM background expectation, and the results are used to set limits on the sfermion production cross-section. The systematic effects are studied in the same manner as described in Section 4.3.3 and 4.4.3.

At $\sqrt{s} = 130 - 172$ GeV for all the sfermion searches and at $\sqrt{s} = 183$ GeV for the slepton searches the systematic effects given in Section 4.4.3 on the expected background

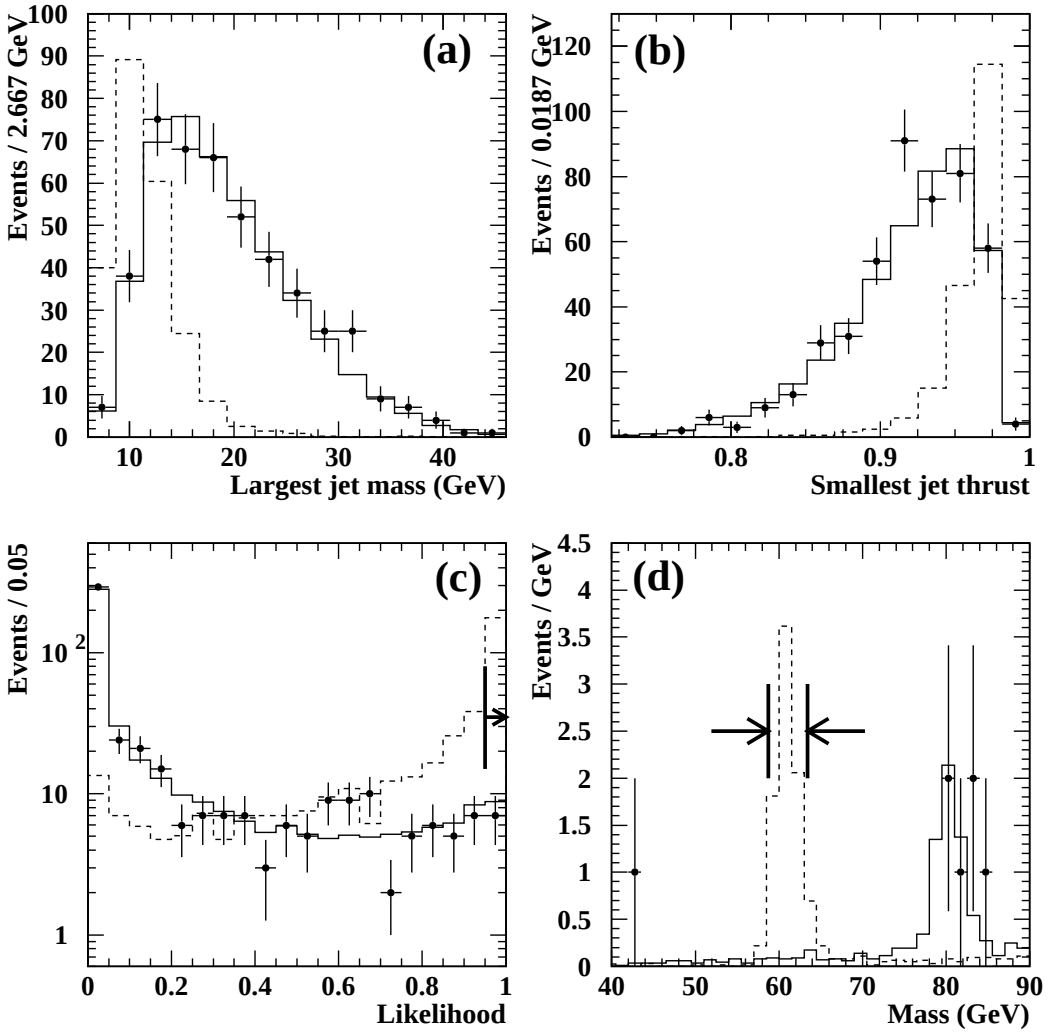

Figure 6.5: *Squark search at $\sqrt{s}$ = 183 GeV: Distributions of (a) the largest jet mass, (b) the smallest jet thrust, (c) the likelihood output and (d) the invariant mass using a five-constraint kinematic fit. Selected data events are shown as dots with error bars, the SM background estimates as solid histograms and a simulated signal of 60 GeV mass as dotted histograms. Background samples are normalized to the integrated luminosity of the data, while the signal normalization is arbitrary. The arrows indicate the position of the likelihood cut and the mass window for a 60 GeV squark.*

Physics		Squark mass				
Process		45 GeV	60 GeV	75 GeV	80 GeV	90 GeV
Number of selected data events						
		1	0	0	3	2
Number of events expected from SM processes						
		0.16±0.04	0.29±0.06	0.59±0.08	4.25±0.22	0.34±0.06
Signal selection efficiency (%)						
$\bar{u}\bar{u}$	λ''_{112}	23.1±1.3	29.5±1.4	29.8±1.4	26.5±1.4	26.9±1.4
	λ''_{123}	14.0±1.1	19.7±1.3	19.0±1.2	21.1±1.3	22.1±1.3

Table 6.5: *Squark search at $\sqrt{s}$ = 183 GeV: Numbers of selected data and expected background events together with the signal selection efficiencies after the mass selection for various squark masses. The Yukawa couplings involved in the squark decays are given. Errors are statistical only.*

and on the signal selection efficiencies are used.

An additional source of uncertainty comes from the reutilization of charged Higgs boson Monte Carlo samples to estimate the efficiency for certain sfermion processes. This effect, ranging between $0 - 12\%$, is taken into account as an inefficiency by which the signal selection efficiency is conservatively decreased.

After the mass selection the statistical error due to the limited number of MC events is $4.4 - 24\%$ on the signal selection efficiency and $2.3 - 43.7\%$ on the background estimate, depending on the centre-of-mass energy and the mass hypothesis.

At $\sqrt{s} = 183$ GeV in the squark searches in addition to the statistical error, ranging from 5 to 8%, the signal selection efficiency is subject to the following systematic effects:

- imperfect modelling of the selection variables, 13.2%;
- uncertainties of the jet resolutions and energy scales in the kinematic fits, 2.0%.

The effect of different fragmentation and hadronization models in squark decays is tested comparing samples generated by SUSYGEN and a special scalar top (stop) gener-

ator [103, 104] used in OPAL stop searches [105]. It is found that SUSYGEN produces wider jets, and our efficiency would be significantly higher for events generated by the stop generator, so it is conservative to use SUSYGEN samples.

The background estimate is affected by the following:

- imperfect modelling of the hadronization process and the four-fermion final states, 20.4%;
- imperfect modelling of the selection variables, 23.8%;
- uncertainties of the jet resolutions and energy scales in the kinematic fits, 4.0%.

The additional statistical error varies between 5.2% and 25% depending on the mass hypothesis.

The error on the integrated luminosity measured by the Silicon Tungsten luminometer is 0.5%.

The total systematic error is 13.4% on the signal rate and 31.6% on the background expectation.

6.4 Four-Jet Final State with Missing Energy

Direct decays of charginos $\tilde{\chi}^+\tilde{\chi}^- \to \nu\mathrm{qq}\nu\mathrm{qq}$ and neutralinos $\tilde{\chi}^0\tilde{\chi}^0 \to \nu\mathrm{qq}\nu\mathrm{qq}$ or indirect decays of sneutrinos $\tilde{\nu}\bar{\tilde{\nu}} \to \nu\tilde{\chi}^0\bar{\nu}\tilde{\chi}^0 \to \nu\nu\mathrm{qq}\nu\nu\mathrm{qq}$ via λ' coupling can lead to final states with four jets and sizable missing energy due to the undetected neutrinos. The dominant backgrounds come from four-fermion processes, dominantly $\mathrm{W}^+\mathrm{W}^- \to \mathrm{q\bar{q}}\ell\nu$, and radiative or mismeasured two-fermion events.

The analyses start with the selection of four-jet events with missing energy and missing momentum transverse to the beam direction, and then a set of variables are combined using the likelihood technique to reject the remaining background.

6.4.1 Gaugino Search

(1) The event has to pass the off-line multihadron selection described in Section 3.2.1.

(2) To account for the two unmeasured neutrinos, the visible energy of the event is required to be less than $0.85\sqrt{s}$.

To reject two-photon and radiative two-fermion events the following criteria are prescribed:

(3) The transverse momentum should be larger than 10 GeV.

The total energy measured in the forward calorimeter, gamma-catcher and silicon tungsten calorimeter should be less than 20 GeV.

The missing momentum should not point to the beam direction, $|\cos\theta_{\mathrm{miss}}| < 0.96$.

(4) The event is forced into four jets using the Durham jet-finding algorithm and rejected if the jet resolution parameter y_{34} is less than 0.001.

(5) An additional cut is applied against semi-leptonic four-fermion background, vetoing events with isolated leptons. Leptons are recognized by the ANN tau identification routine described in Section 3.2.5, which is also efficient in recognizing electrons and muons. An event is rejected if it has a lepton candidate with ANN output larger than 0.97.

A likelihood technique is employed to classify the remaining events as two-fermion, four-fermion or $\tilde{\chi}\tilde{\chi} \to \mathrm{qqqq}\nu\nu$ processes. The information of the following variables enters the selection:

- the effective centre-of-mass energy of the event;
- the transverse momentum of the event;
- the cosine of the polar angle of the missing momentum vector;
- the D parameter of the event;
- the logarithm of the y_{34} parameter;
- the minimum number of charged tracks in a jet;
- the minimum number of electromagnetic clusters in a jet;
- the highest track momentum;
- the highest electromagnetic cluster energy;
- the number of leptons in the event, using a loose selection of the lepton candidates requiring the ANN output to be larger than 0.5;

- the mass of the event excluding the best lepton candidate (if any) after a one-constrained kinematic fit using the $W^+W^- \to qq\ell\nu$ hypothesis as described in Section 4.3.2;
- the cosine of the smallest jet opening angle, defined by the half-angle of the smallest cone containing 68% of the jet energy;

(6) As a final selection an event is rejected if its likelihood output is less than 0.95.

Figure 6.6 shows five likelihood variables and the resulting likelihood output for the data, the estimated background and simulated signal events. The shapes of the distributions are well-described by the Monte Carlo simulation, even if some excess of events is observed after the cut on the visible energy due to a shift of the distribution toward lower values in the data. The same behaviour is observed in other searches for final states with missing energy, see for example Figure 4.4(a). The observed and expected number of events together with the relative weight of the four-fermion processes is given in Table 6.6 before and after the likelihood selection. At the end of the selection there are no more events observed than predicted by the SM. The excess events seen before the likelihood selection are sitting in the first bin close to zero in the likelihood output distribution.

	Data	Background	4f contribution
Before LH selection	280	241.8±1.7	48.3%
After LH selection	8	9.47±0.33	72.0%

Table 6.6: *Gaugino search at $\sqrt{s}$ = 183 GeV: Numbers of selected data and expected background events together with the contribution of four-fermion processes before and after the likelihood selection. Errors are statistical only.*

The signal selection efficiencies are listed in Table 6.7 for the simulated masses and λ' couplings. The small efficiency for light gaugino masses is explained by the presence of initial state radiation and the larger boost of the jets.

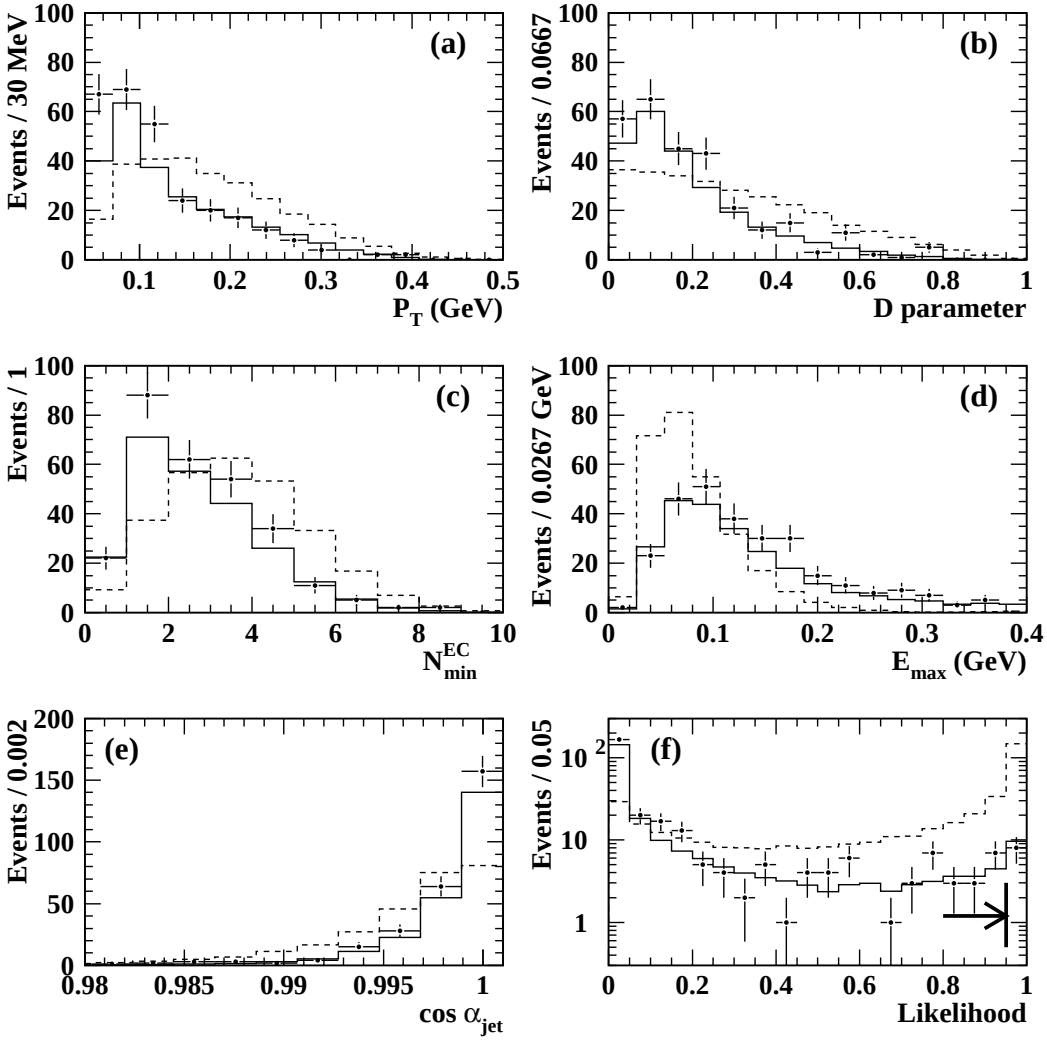

Figure 6.6: *Gaugino search at $\sqrt{s}$ = 183 GeV: Distributions of likelihood input variables and the resulting likelihood output: (a) momentum transverse to the beam direction, p_{T}; (b) D event shape variable; (c) smallest number of electromagnetic clusters per jet, $N^{\mathrm{EC}}_{\mathrm{min}}$; (d) highest electromagnetic cluster energy, E_{max}; (e) cosine of the smallest jet opening angle containing 68% of the jet energy, $\cos\alpha_{\mathrm{jet}}$ and (f) likelihood output. Selected data events are shown as dots with error bars, the SM background estimates as solid histograms and a simulated signal as dashed histograms. Background samples are normalized to the integrated luminosity of the data, while the signal normalization is arbitrary. The arrow indicates the position of the likelihood cut.*

Gaugino	Yukawa	m_0	Efficiency (%) for gaugino mass			
Production	Coupling	(GeV)	30 GeV	45 GeV	70 GeV	90 GeV
$\tilde{\chi}_1^0\tilde{\chi}_1^0$	λ'_{121}	1000	0.6±0.2	5.2±0.5	22.5±0.9	41.1±1.1
		48.4	—	—	23.4±0.9	—
	λ'_{123}	1000	1.6±0.3	10.1±0.7	35.3±1.1	53.4±1.1
		48.4	—	—	34.0±1.1	—
$\tilde{\chi}_1^+\tilde{\chi}_1^+$	λ'_{121}	1000	—	6.5±0.8	34.0±1.5	50.8±1.6
		48.4	—	—	33.9±1.5	—
	λ'_{123}	1000	—	8.5±0.9	44.3±1.4	59.5±1.6
		48.4	—	—	42.0±1.6	—

Table 6.7: *Gaugino search at $\sqrt{s} = 183$ GeV: Signal selection efficiencies for various masses. The Yukawa coupling involved in the gaugino decay and the assumed common scalar mass m_0 are given. Errors are statistical only. Dashes indicate masses which are not simulated.*

6.4.2 Sneutrino Search

The main difference between final states originating from gaugino and sneutrino pair production is the amount of missing energy taken away by the neutrinos. In the case of indirect decays of pair-produced sneutrinos through an R-parity violating λ' coupling, the first step of the cascade decay is $\tilde{\nu} \to \nu\tilde{\chi}^0$ leading usually to an energetic neutrino and a neutralino with energy significantly smaller than the beam energy, at least for not very small mass differences, $\Delta m = m_{\tilde{\nu}} - m_{\tilde{\chi}_1^0}$. The next step is the decay of the neutralino $\tilde{\chi}^0 \to \nu$qq which results in an additional neutrino. Therefore we will have more invisible energy and momentum and less energetic jets compared to the direct gaugino decays.

The selection developed to search for gaugino pair-production is modified in the following way to be applicable for sneutrino searches:

- The cut on the visible energy of the event is moved to $0.75\sqrt{s}$.
- The selection on the jet resolution parameter y_{34} is loosened, requiring it to be larger than 0.0008.

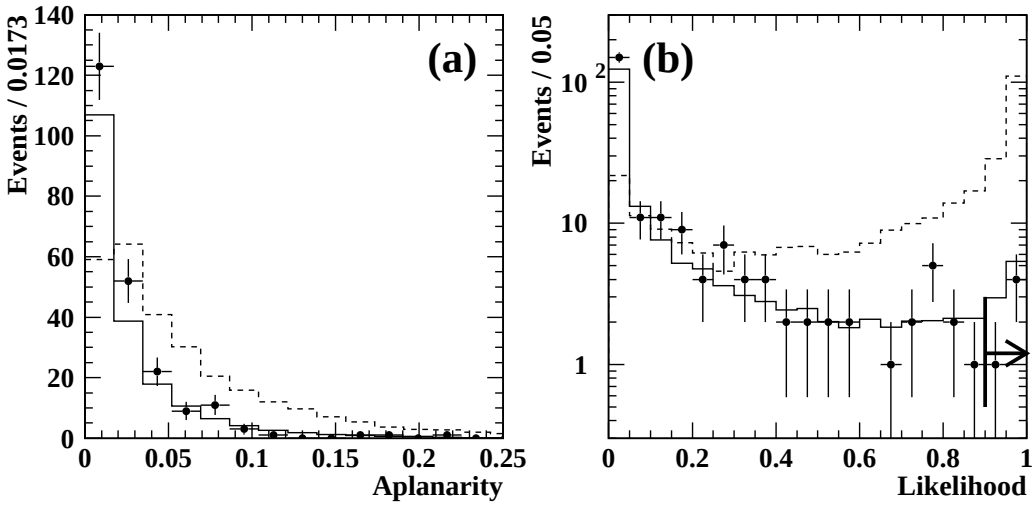

Figure 6.7: *Sneutrino search at $\sqrt{s} = 183$ GeV: Aplanarity (a) and likelihood output (b) distributions. Selected data events are shown as dots with error bars, the SM background estimates as solid histograms and a simulated signal as dashed histograms. Background samples are normalized to the integrated luminosity of the data, while the signal normalization is arbitrary. The arrow indicates the position of the likelihood cut.*

- Among the likelihood selection variables

  $\rightarrow$ the smallest number of charged tracks in a jet and

  $\rightarrow$ the smallest number of electromagnetic clusters in a jet

  are replaced by

  $\rightarrow$ the aplanarity of the event,

  and the cut on the likelihood output is placed at 0.9.

The distribution of the new likelihood variable and the resulting likelihood output is shown in Figure 6.7.

The number of selected data and expected background events are shown in Table 6.8. No excess of events over the SM background is observed after all cuts.

The signal selection efficiencies are listed in Table 6.9. Their small value for $\Delta m = \frac{1}{2} m_{\tilde{\nu}}$

	Data	Background	4f contribution
Before LH selection	224	193.6±1.5	48.9%
After LH selection	5	8.17±0.31	74.9%

Table 6.8: *Sneutrino search at $\sqrt{s}$ = 183 GeV: Numbers of selected data and expected background events together with the contribution of four-fermion processes before and after the likelihood selection. Errors are statistical only.*

Sneutrino	Yukawa	Δm	Efficiency (%) for sneutrino mass		
Production	Coupling		45 GeV	70 GeV	90 GeV
$\tilde{\nu}_e\bar{\tilde{\nu}}_e$	λ'_{121}	$\frac{1}{2}m_{\tilde{\nu}}$	7.5±0.8	20.7±1.3	30.6±1.5
		5 GeV	—	—	47.7±1.6
	λ'_{123}	$\frac{1}{2}m_{\tilde{\nu}}$	4.9±0.7	18.1±1.2	28.5±1.4
		5 GeV	—	—	40.3±1.6

Table 6.9: *Sneutrino search at $\sqrt{s}$ = 183 GeV: Signal selection efficiencies for $\tilde{\nu}_e\bar{\tilde{\nu}}_e$ production at various masses. The Yukawa coupling involved in the decay and the assumed mass difference Δm are given. Errors are statistical only. Dashes indicate masses which are not simulated.*

is due to the requirement that the events should pass the off-line multihadron selection. This off-line classification has an efficiency of $49 - 58\%$ for these samples, whereas for small mass differences, when the events are energetically more balanced, an efficiency well above 90% is reached. Another effect which hurts the efficiency for light sneutrino masses is the initial state radiation.

6.4.3 Systematic Effects

The signal selection efficiencies, in addition to the statistical error due to the limited number of MC events, varying between 2 and 14% for masses above 45 GeV, are affected by the following systematics:

- uncertainty on the lepton veto, 1%;
- imperfect modelling of the selection variables used in the analysis, 6% in the gaugino and 6.7% in the sneutrino search.

In the derivation of the cross-section limits for gaugino production an inefficiency of $0 - 5\%$ due to the variation of m_0 is taken into account.

The background expectation is subject to the following systematic effects:

- uncertainty on the lepton veto, 1%;
- imperfect modelling of the hadronization and four-fermion production processes, 3.3% in the gaugino and 5.3% in the sneutrino search;
- imperfect modelling of the selection variables used in the analysis (dominated by the error on the visible energy), 21% in the gaugino and 14.9% in the sneutrino search;

The additional statistical error is 3.5% in the gaugino and 3.8% in the sneutrino search.

The uncertainty on the luminosity measurement is 0.5%.

The total systematic error is 6.1% and 6.8% on the signal rate and 21.3% and 15.8% on the background estimate in the gaugino and sneutrino searches, respectively.

The inefficiency due to the forward energy veto is 1.8%, by which both the signal rate and the expected background is decreased.

6.5 Results and Interpretation

As each search is in agreement with the SM expectation, there is no claim for a signal, and cross-section limits at the 95% CL are established. The cross-section limits are interpreted within the framework of the Constrained MSSM[3] (CMSSM) to calculate lower limits on the sparticle masses. The limits in the CMSSM depend on the following parameters: the common scalar mass at the GUT scale, m_0; the SU(2) gaugino mass parameter at electroweak scale, M_2; the mixing parameter of the two Higgs doublets, μ; and the ratio of the vacuum expectation values for the two Higgs doublets, $\tan\beta = v_2/v_1$.

[3]CMSSM is a *gravity-inspired* SUSY model with features described in Section 1.2.3.

When combining several decay channels a likelihood ratio method [106] is used to determine an upper limit on the cross-section. This method combines the individual analyses looking for the different final states possible for one given λ-like coupling and assigns greater weight to those with a higher expected sensitivity, taking into account the expected number of background events. The systematic and the statistical errors are added in quadrature and subtracted when using the number of background events.

6.5.1 Gaugino Search

Cross-section upper limits at the 95% CL are calculated for the final state topologies expected from R-parity violating decays of charginos and neutralinos. Figure 6.8 shows the upper limits on the production cross-section of the four-jet final state with missing energy using the results of the selection described in Sections 6.4.1. The limits shown are independent on the first index of the coupling λ'_{ijk}, corresponding to the neutrino flavour.

In order to present cross-section limits for chargino and neutralino production, the different search channels corresponding to the same Yukawa coupling are combined, separately for direct and indirect decays and independent of the decay mode. These limits are valid for couplings larger than 10^{-5} assuming a prompt decay at the interaction vertex. It is also required that the mass difference $\Delta m_{\tilde{\chi}} = m_{\tilde{\chi}_1^\pm} - m_{\tilde{\chi}_0^\pm}$ is larger than 5 GeV and that only one Yukawa coupling is different from zero. For indirect decays of charginos, it is assumed that they decay through a $W^{\pm *}$, and the results are combined using the hadronic and leptonic branching ratios of the $W^\pm$ boson. The branching ratios into the direct and indirect decays depend on the MSSM parameters. Therefore, when calculating mode independent limits their branching ratios are varied simultaneously between 0 and 1. The efficiency for the process when one chargino decays via the direct and the other via the indirect mode is set to zero. For each mass the worst cross-section limit is taken as the decay mode independent upper limit. As an example, the mode independent cross-section upper limit is given for charginos decaying via λ' coupling in Figure 6.9.

Another way to interpret our results is to exclude regions in the MSSM parameter space

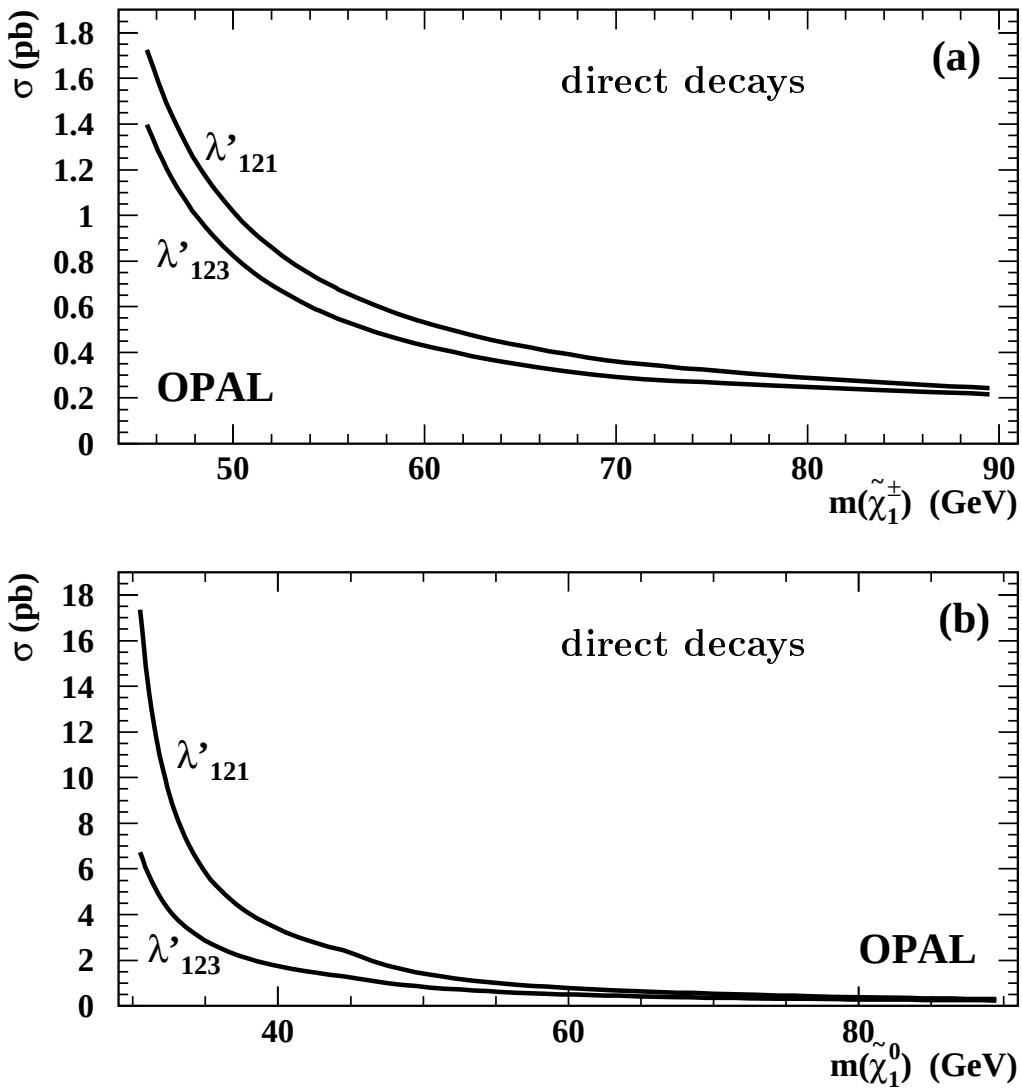

Figure 6.8: *Direct gaugino decays via $\lambda^{'}$ coupling: Upper limits at the 95% CL on the production cross-section of the four-jet final state with missing energy resulting from (a) chargino and (b) neutralino pair-productions. For each curve the $\lambda^{'}$ coupling that is assumed to be different from zero is given.*

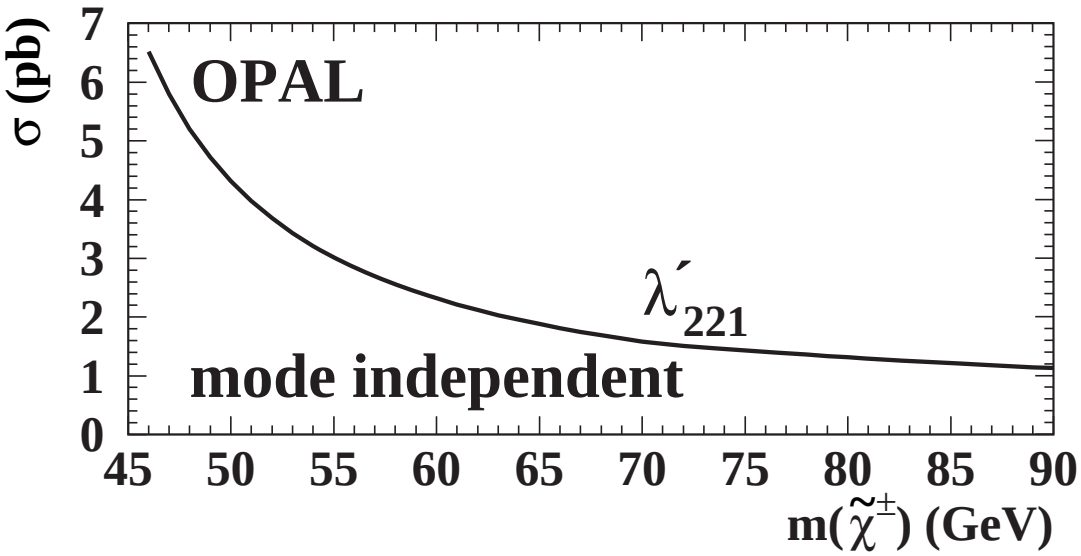

Figure 6.9: *Chargino decays via λ' coupling: Upper limits at the 95% CL on the pair-production cross-section independent of the decay mode. The limit corresponds to λ'_{221} and is valid for any couplings λ'_{ijk} with $i = 1, 2$.*

using the topological cross-section upper limits. These exclusion limits are computed by combining the excluded cross-sections with the measurement of the excess Z^0 width [107] obtained by comparing the measured and the predicted width. Since each point in the MSSM parameter space corresponds to a chargino and a neutralino mass pair, from the excluded regions one can place bounds on the allowed mass domain of these particles. The lower limit on the mass of the lightest chargino and neutralino for $m_0 = 500$ GeV, independent of which R-parity violating Yukawa coupling is assumed to be different from zero, is shown in Figure 6.10 as a function of $\tan\beta$. A lower mass limit of 76 GeV is established for the lightest chargino for $\tan\beta > 1$ and 29 GeV for the lightest neutralino for $\tan\beta > 1.2$.

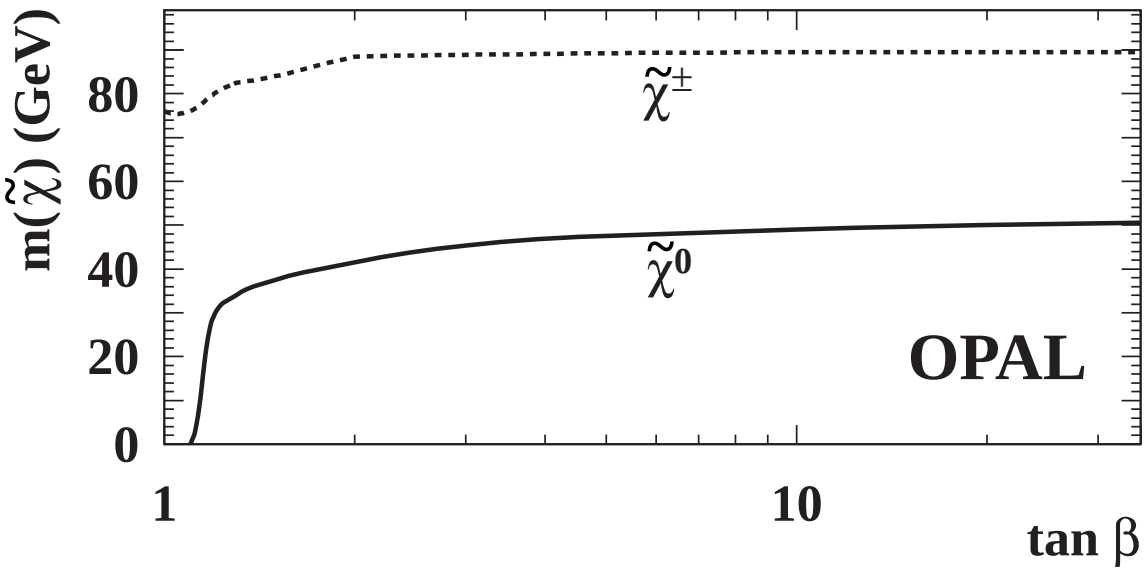

Figure 6.10: *Gaugino search: Lower limits at the 95% CL on gaugino masses as a function of* $\tan\beta$ *for* $m_0 = 500$ *GeV for any coupling* λ, λ' *or* λ''. *Results for* $\tilde{\chi}_1^0$ *and* $\tilde{\chi}_1^{\pm}$ *are shown as solid and dashed lines, respectively. The exclusion limit for* $\tilde{\chi}_1^0$ *does not result from direct searches for* $\tilde{\chi}_1^0$ *decays but from the excluded CMSSM parameter space from* $\tilde{\chi}_1^{\pm}$ *searches.*

6.5.2 Slepton Search

Two approaches are used to present sfermion production limits, similarly to the interpretation of gaugino search results. Upper limits on production cross-sections as functions of the sfermion masses are calculated with minimal model assumptions. These upper limits are based on the assumptions that the sparticles are pair-produced, decay promptly in the interaction vertices and that only one λ-like coupling at a time is nonzero. Limits on the sfermion masses are calculated in the framework of the CMSSM.

For the indirect sfermion decays, we have used the branching ratios for the decay $\tilde{f} \to f\tilde{\chi}_1^0$ predicted by the MSSM, and assumed no experimental sensitivity to any other decay mode. The branching ratio for direct decay is always treated as equal to unity. The MSSM

mass exclusion plots presented here are computed for $\tan\beta = 1.5$ and $\mu = -200$ GeV. This choice of parameters is rather conservative as sfermion production cross-sections generally increase for larger values of $\tan\beta$ or $|\mu|$.

In the indirect decay of a sfermion, $\tilde{f} \to f\tilde{\chi}_1^0$, via λ' coupling, the neutralino can decay into two quarks and a charged lepton or into two quarks and a neutrino. The relative branching ratios of these decays depend on the MSSM parameters. In order to present results independent of the MSSM parameters the branching ratios of the neutralino decays leading to two jets and a charged or neutral lepton are varied simultaneously between 0 and 1, and the lowest cross-section limit is retained.

For the direct decays, the final states are fully determined by the indices of the coupling considered.

In the following cross-section limits are shown for the direct and indirect decays leading to four-jet topology with or without missing energy studied in Section 6.3 and 6.4.2. In all cross-section plots for direct sfermion decays only the curve corresponding to the worst cross-section limit is shown amongst all possible cross-section limits resulting from the couplings considered.

Excluded regions are shown in the MSSM framework. For this our results are combined with the results of other searches for pair-production of sfermions followed by R-parity violating decays. The excluded regions for the indirect decays are valid for $\Delta m = m_{\tilde{\ell}} - m_{\tilde{\chi}_1^0} \geq 5$ GeV except for the indirect decays of staus via λ' which are valid for $\Delta m = m_{\tilde{\tau}} - m_{\tilde{\chi}_1^0} \geq 22.5$ GeV. In this particular case there is not enough sensitivity to place limits in the small Δm region. The excluded regions for the direct decays are independent of Δm.

When interpreting the results, a conservative approach is adopted by always choosing the lowest efficiencies, in the limit calculation.

Selectron Limits

Figure 6.11 shows upper limits on the cross-sections of pair-produced selectrons directly decaying via λ' coupling to a four-jet final state. The peak structure visible in the figure at approximately the mass of the $W^{\pm}$ boson comes from the irreducible background due to W^+W^- production.

In the MSSM, the selectron pair-production cross-section is enhanced by the presence of the t-channel process. Figure 6.12 shows exclusion limits at the 95% CL for selectrons decaying via λ' coupling. For indirect decays the exclusion refers to the right-handed selectron giving the smaller excluded region, and for direct decays to the left-handed selectron. A mass smaller than 75.5 GeV is excluded in the case of direct decays.

Smuon and Stau Limits

Figure 6.13 shows the upper limit on the cross-sections of pair produced smuons decaying directly via λ' coupling to a four-jet final state. The same limit is also valid for stau pair-production. In the MSSM, for direct decays, left-handed smuons and staus with a mass smaller than 63.5 GeV are excluded, as shown in Figure 6.14.

Sneutrino Limits

Figure 6.15 shows the cross-section limits for electron-sneutrino pair-production followed by an indirect decay via λ' coupling leading to four-jet final states with missing energy.

Figure 6.16 shows upper limits on the cross-sections of pair-produced $\tilde{\nu}_{\mathrm{e}}$ decaying directly via λ' coupling to a four-jet final state. The searches for $\tilde{\nu}_{\mu}$ and $\tilde{\nu}_{\tau}$ yield identical limits with the search for smuons, shown in Figure 6.13.

In the MSSM, the $\tilde{\nu}_e$ pair-production cross-section is enhanced by the presence of the t-channel diagram. Figure 6.17 shows exclusion limits at the 95% CL for electron-sneutrinos decaying via λ' coupling. For direct decays electron-sneutrinos with mass below 80 GeV are excluded, and for indirect decays, in the case of a low-mass $\tilde{\chi}_1^0$, a mass limit of 86.5 GeV is derived. MSSM exclusion plots for $\tilde{\nu}_{\mu}$ and $\tilde{\nu}_{\tau}$ are not shown because of their very

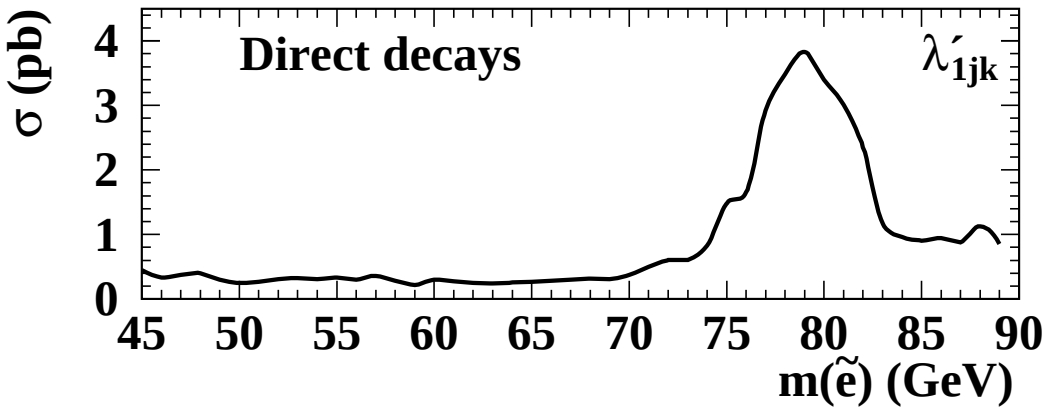

Figure 6.11: *Direct selectron decays via λ' coupling: Upper limits at the 95% CL on the pair-production cross-section.*

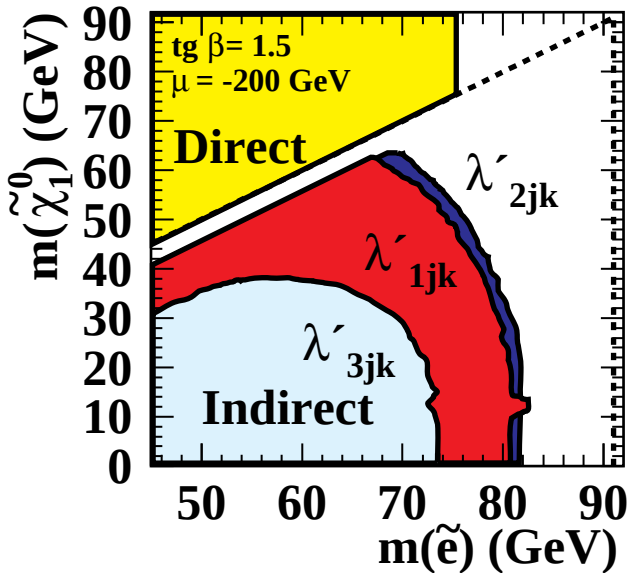

Figure 6.12: *Selectron search: Excluded regions in the framework of CMSSM at the 95% CL for $\tilde{e}^+\tilde{e}^-$ production in the $[m_{\tilde{e}}, m_{\tilde{\chi}_1^0}]$ plane for λ' couplings. For indirect decays the results correspond to right-handed selectrons and for direct decays to left-handed selectrons. The kinematic limit is shown as a dashed line. The gap between the excluded regions for direct and indirect decays corresponds to $\Delta m = m_{\tilde{e}} - m_{\tilde{\chi}_1^0} < 5$ GeV.*

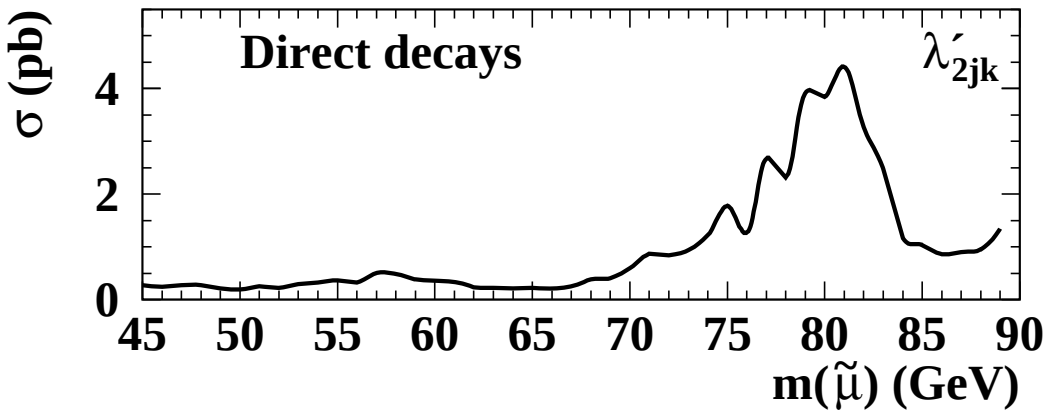

Figure 6.13: *Direct smuon decays via $\lambda^{'}$ coupling: Upper limits at the 95% CL on the pair-production cross-section.*

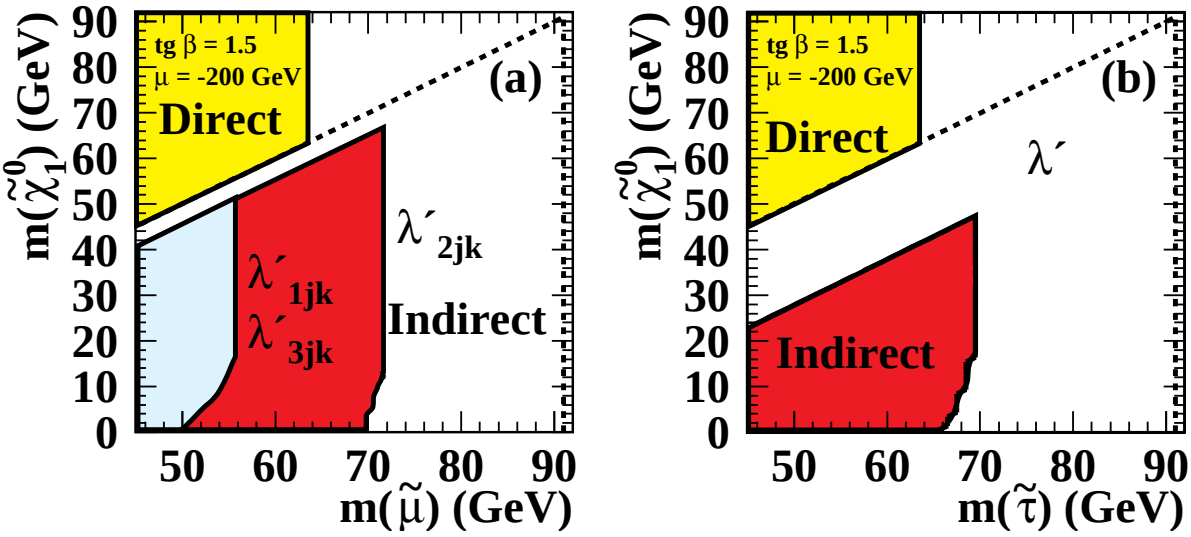

Figure 6.14: *Smuon and stau searches: Excluded regions in the framework of CMSSM at the 95% CL for (a) $\tilde{\mu}^+\tilde{\mu}^-$ and (b) $\tilde{\tau}^+\tilde{\tau}^-$ production in the $[m_{\tilde{\ell}}, m_{\tilde{\chi}_1^0}]$ plane for $\lambda^{'}$ couplings. For indirect decays the results correspond to right-handed sfermions and for direct decays to left-handed sfermions. The kinematic limit is shown as a dashed line. The gaps between the excluded regions for direct and indirect decays correspond to $\Delta m = m_{\tilde{\ell}} - m_{\tilde{\chi}_1^0} < 5$ GeV for smuons and $\Delta m < 22.5$ GeV for staus.*

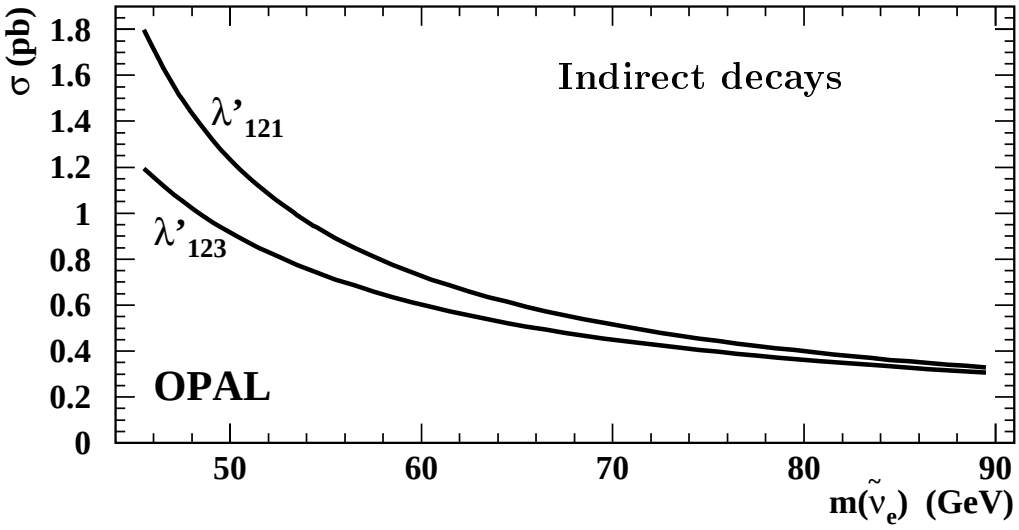

Figure 6.15: *Indirect sneutrino decays via λ' coupling: Upper limits at the 95% CL on the production cross-section of the four-jet final state with missing energy resulting from electron-sneutrino pair-production. For each curve the coupling λ' that was assumed to be different from zero is given.*

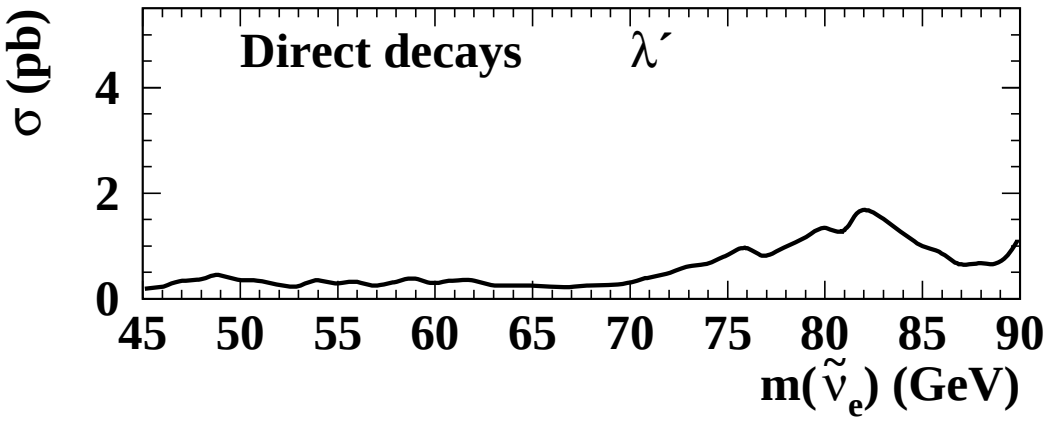

Figure 6.16: *Direct sneutrino decays via λ' coupling: Upper limits at the 95% CL on the pair-production cross-section of electron-sneutrinos.*

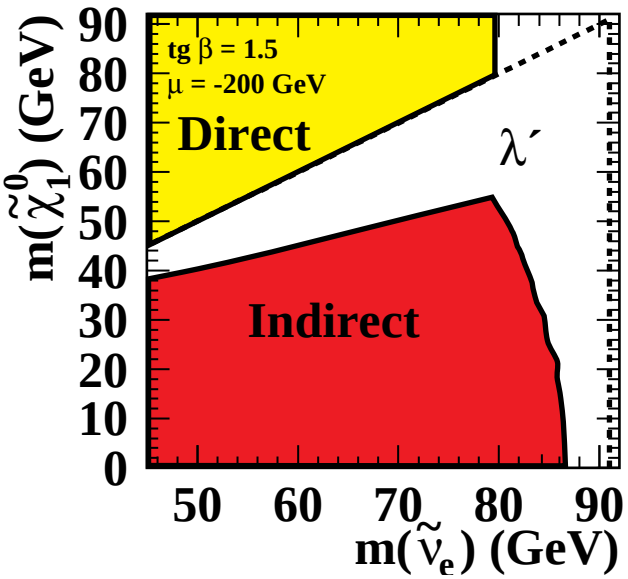

Figure 6.17: *Sneutrino search: Excluded regions in the framework of CMSSM at the 95% CL for $\tilde{\nu}_e\bar{\tilde{\nu}}_e$ production in the $[m_{\tilde{\nu}_e}, m_{\tilde{\chi}_1^0}]$ plane for λ' couplings. The kinematic limit is shown as a dashed line.*

small cross-sections. For direct decays via λ' coupling a lower mass limit of 58 GeV is obtained.

Squark Limits

For squark decays via λ'' couplings a cross-section limit of approximately 0.2 pb was derived for squark masses up to $\approx$ 75 GeV, slightly increasing in the range of the $W^{\pm}$ boson mass, as shown in Fig. 6.18.

Assuming the same experimental sensitivity for scalar top quarks as for first-generation squarks, based on systematic studies, the mass of the scalar top quark can be bounded. A lower mass limit of $76 - 79$ GeV is obtained depending on the mixing angle between left- and right-handed states[4].

[4]The lightest mass eigenstate for scalar top quarks is given by $\tilde{t}_1 = \tilde{t}_L \cos\theta_{\tilde{t}} + \tilde{t}_R \sin\theta_{\tilde{t}}$.

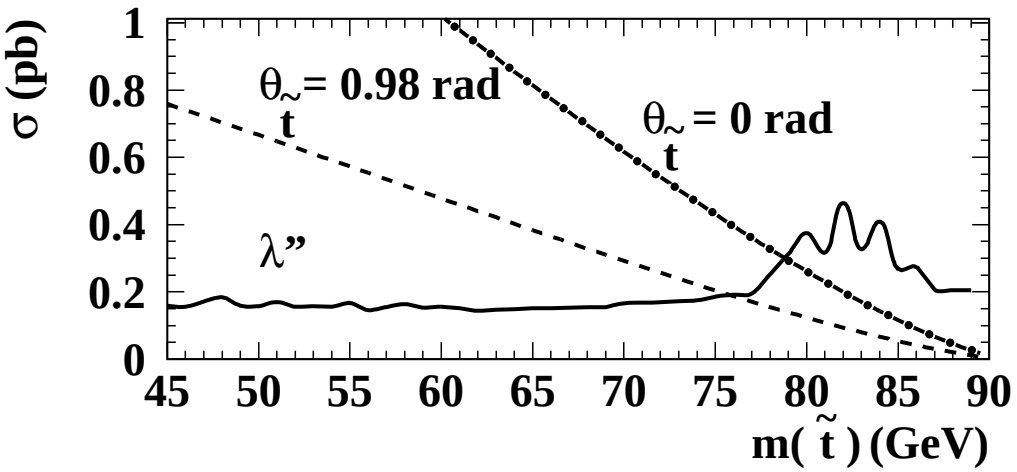

Figure 6.18: *Squark direct decays via λ'' coupling: Upper limits at the 95% CL on the pair-production cross-section. The CMSSM predictions for the minimum and maximum cross-sections of the scalar top quark pair-production are shown as dashed and dash-dotted lines, and correspond to mixing angles between left- and right-handed states of 0.98 rad and 0 rad, respectively.*

6.6 Conclusions

We presented a search for pair-produced supersymmetric particles with R-parity violating decays resulting in final states with four jets with or without missing energy using the data collected by the OPAL detector at $\sqrt{s} = 130 - 183$ GeV. No significant excess of events over the SM expectation is observed in the data. Cross-section upper limits are computed for processes leading to the studied final states and in combination with other searches on the pair-production cross-section of sparticles. The results are interpreted within the framework of the CMSSM, leading to lower limits on the sparticle masses.

Outlook

In this work we presented searches for new particles pair-produced in electron-positron collisions, charged Higgs bosons, hypothetical scalars with similar masses and supersymmetric particles decaying via R-parity violating transitions, whose discovery would point without ambiguity toward physics beyond the Standard Model. Our studies have not revealed any new phenomena, all of our results are in a good agreement with the Standard Model expectations. As a consequence we have placed bounds on possible new physics in the form of upper limits on production cross-sections and lower bounds on the masses of the sought-after particles when interpreting our results in the framework of specific models.

There is a wealth of theoretical models aiming to fill in the gaps in our understanding of the fundamental laws of Nature and only experimental evidence can prove or deny any of them by verifying their predictions. In this spirit will experimental efforts, guided by theoretical considerations, continue to explore the frontiers of our knowledge. I strongly hope that soon we shall make the first observation of a clean, unambiguous experimental signal that demands an explanation beyond the Standard Model, as this will bring about an extremely exciting era, a new revolution of Particle Physics.

Bibliography

[1] S.L. Glashow, J. Iliopoulos and L. Maiani, Phys. Rev. **D2** (1970) 1285;
S. Weinberg, Phys. Rev. Lett. **19** (1967) 1264;
A. Salam, *Elementary Particle Theory*, ed. N. Svartholm Almquist and Wiksells, Stockholm, 1968, p. 367.

[2] Excellent rewiews on many aspects of the Higgs boson physics can be found in:
J.F. Gunion, H.E. Haber, G.L. Kane and S. Dawson, *The Higgs Hunter's Guide*, Addison-Wesley Publishing Company, Reading, MA, 1990;
G.L. Kane, *Perspectives on Higgs Physics*, World Scientific, Singapore, 1993;
G.L. Kane, *Perspectives on Higgs Physics II*, World Scientific, Singapore, 1997.

[3] F. Zwirner, *Beyond the Standard Model*, in *Proceedings of the 1997 European School of High-Energy Physics*, CERN 98-03, p. 293.

[4] P.W. Higgs, Phys. Lett. **12** (1964) 132;
F. Englert and R. Brout, Phys. Rev. Lett. **13** (1964) 321;
G.S. Guralnik, C.R. Hagen and T.W.B. Kibble, Phys. Rev. Lett. **13** (1964) 585.

[5] P.Sikivie, L. Susskind, M. Voloshin and V. Zakharov, Nucl. Phys. **B173** (1980) 189.

[6] See for example: S. Weinberg, *The Quantum Theory of Fields*, Cambridge University Press, 1996, Vol. II., Chapter 22.

[7] K. Wilson as quoted by L. Susskind, Phys. ReV **D20** (1979) 2019;
E. Gildener and S. Weinberg, Phys. ReV **D13** (1976) 3333;

S. Weinberg, Phys. Lett. **B82** (1979) 387;
G. t'Hoft, in *Recent Developments in Gauge Theories*, ed. by G. t'Hoft *et al.*, Plenum Press, New York, NY, 1980, p. 135.

[8] N. Cabibbo, L. Maiani, G. Parisi and R. Petronzio, Nucl. Phys. **B158** (1979) 295.

[9] E. Accomando *et al.*, in *Physics at LEP2*, CERN 96-01, Vol.1, p. 351.

[10] The Particle Data Group, C. Caso *et al.*, *Review of Particle Physics*, Eur. Phys. J. **C3** (1998) p. 347 and references therein.

[11] Y. Gol'fand and E. Likhtam, JETP Lett. **13** (1971) 323;
D. Volkov and V. Akulov, Phys. Lett. **B46** (1973) 109;
J. Wess and B. Zumino, Nucl. Phys. **B70** (1974) 39.

[12] P.C. West, *Supersymmetry: A Decade of Development*, Adam Hilger, Bristol, 1986;
G. Kane, *Perspectives on Supersymmetry*, World Scientific, Singapore, 1998.

[13] H.P. Nilles, Phys. Rep. **110** (1984) 1.

[14] H.E. Haber and G.L. Kane, Phys. Rep. **117** (1985) 75.

[15] P. Fayet, in *Unification of the Fundamental Particle Interactions*, ed. by S. Ferrara, J. Ellis and P. Van Nieuewenhuizen, Plenum Press, New York, NY, 1980, p. 727.

[16] M. Carena, J.R. Espinosa, M. Quirós and C.E.M. Wagner, Phys. Lett. **355B** (1995) 209.

[17] See for example: G.G. Ross, *Grand Unified Theories*, Benjamin-Cummings, Menlo Park, CA, 1984.

[18] S. Dimopoulos and H. Georgi, Nucl. Phys **B193** (1981) 150;
N. Sakai, Z. Phys. **C11** (1982) 153.

[19] L.J. Hall, J. Lykken and S. Weinberg, Phys. Rev. **D27** (1983) 2359.

[20] S.K. Soni and H.A. Weldon, Phys. Lett.**126B** (1983) 215.

[21] P. Nath, R. Arnowitt and A.H. Chamseddine, *Applied N = 1 Supergravity*, World Scientific, Singapore, 1984;
W. de Boer, Prog. in Part. Nucl. Phys. **33** (1994) 201.

[22] M. Dress and S.P. Martin, in *Electroweak Symmetry Breaking and New Physics at the TeV Scale*, ed. by T. Barklow, S. Dawson, H.E. Haber and J. Siegrist, World Scientific, Singapore, 1996, p. 146.

[23] The OPAL Collaboration, K. Ahmet *et al.*, Nucl. Inst. and Meth. **A305** (1991) 275.

[24] S. Anderson *et al.*, Nucl. Inst. and Meth. **A403** (1998) 326.

[25] G. Aguillion *et al.*, Nucl. Inst. and Meth. **A417** (1998) 266.

[26] B.E. Anderson *et al.*, IEEE Transactions on Nuclear Science **41** (1994) 845.

[27] M. Arignon *et al.*, Nucl. Inst. and Meth. **A313** (1992) 103.

[28] M. Arignon *et al.*, Nucl. Inst. and Meth. **A333** (1993) 330.

[29] D.G. Charlton, F. Meijers, T.J. Smith and P.S. Wells, Nucl. Inst. and Meth. **A325** (1993) 129.

[30] E. Accomando *et al.*, in *Physics at LEP2*, CERN 96-01, Vol.1, p. 207.

[31] BHWIDE generator: S. Jadach, W. Płaczek and B.F.L. Ward, in *Physics at LEP2*, CERN 96-01, Vol.2, p. 286; UTHEP-95-1001.

[32] KORALZ 4.0 generator: S. Jadach, B.F.L. Ward and Z. Wąs, Comp. Phys. Comm. **79** (1994) 503.

[33] PYTHIA 5.721 and JETSET 7.408 generators: T. Sjöstrand, Comp. Phys. Comm. **82** (1994) 74; T. Sjöstrand, LU TP 95-20.

[34] HERWIG generator: G. Marchesini *et al.*, Comp. Phys. Comm. **67** (1992) 465.

[35] The OPAL Collaboration, K. Ackerstaff *et al.*, Eur. Phys. J. **C1** (1998) 395;
The OPAL Collaboration, K. Ackerstaff *et al.*, Phys. Lett. **B389** (1996) 416;
The OPAL Collaboration, *W^+W^- Production in e^+e^- collisions at 189 GeV*, OPAL Physics Note 99-378.

[36] `grc4f` 1.1 generator: J. Fujimoto *et al.*, Comp. Phys. Comm. **100** (1997) 128.

[37] EXCALIBUR generator: F.A. Berends, R. Pittau and R. Kleiss, Comp. Phys. Comm. **85** (1995) 437.

[38] PHOJET 1.05 generator: R. Engel and J. Ranft, Phys. Rev. **D54** (1996) 4244.

[39] VERMASEREN generator: J.A.M. Vermaseren, Nucl. Phys. **B229** (1983) 347.

[40] HZHA generator: G. Ganis and P. Janot, in *Physics at LEP2*, CERN 96-01, Vol.2, p. 309.

[41] SUSYGEN generator: S. Katsanevas and P. Morawitz, Comp. Phys. Comm. **112** (1998) 23.

[42] The OPAL Collaboration, G. Alexander *et al.*, Z. Phys **C69** (1996) 543.

[43] B. Andersson, G. Gustafson and B. Söderberg, Z. Phys. **C20** (1983) 317

[44] C. Peterson, D. Schlatter, I. Schmitt and P. Zerwas, Phys. Rev. **D27** (1983) 105

[45] J. Allison *et al.*, Nucl. Inst. and Meth. **A317** (1992) 47.

[46] R. Brun *et al.*, *GEANT3 User's Guide*, CERN DD/EE/84-1 (1984)

[47] The OPAL Collaboration, G. Alexander *et al.*, Z. Phys. **C52** (1991) 175.

[48] The OPAL Collaboration, K. Ackerstaff *et al.*, Eur. Phys. J. **C2** (1998) 441.

[49] S. Mihara and S. Yamashita, *MT 3.00: A New Algorithm to Calculate Energy Flow Based on the MT Package*, OPAL Technical Note 98-575.

[50] H. Lafoux, *Update of the Neural Electron ID*, OPAL Technical Note 95-317;
The OPAL Collaboration, G. Akers *et al.*Phys. Lett. **B52** (1994) 327.

[51] N. Brown and W.J. Stirling, Phys. Lett. **B252** (1990) 657;
S. Bethke, Z. Kunszt, D. Soper and W.J. Stirling, Nucl. Phys. **B370** (1992) 310;
S. Catani *et al.*, Phys. Lett. **B269** (1991) 432;
N. Brown and W.J. Stirling, Z. Phys. **C53** (1992) 629.

[52] The OPAL Collaboration, R. Akers *et al.*, Z. Phys **C63** (1994) 197.

[53] J.E. Huth et al., in *Research Directions for the Decade*, ed. by E.L. Berger, World Scientific, Singapore, 1990, p. 134.

[54] The OPAL Collaboration, G. Alexander *et al.*, Z. Phys. **C70** (1996) 357.

[55] H. Lafoux, *A Neural Conversion Finder*, OPAL Technical Note 95-290.

[56] D. Glenzinski and A. Hocker, *An Artificial Neural Network Algorithm for Tau Identification*, OPAL Technical Note 98-559.

[57] The OPAL Collaboration, G. Abbiendi *et al.*, Eur. Phys. J. **C7** (1999) 407.

[58] A.G. Frodesen, O. Skjeggestad and H. Tøfte, *Probability and Statistics in Particle Physics*, Universitetsforlaget, Bergen, 1979, p. 288 for χ^2 probability and p. 307 for constrained least-squares fit.

[59] K. Ishii and S. Yamashita, *Jet Error Parametrization for MT 3.00*, OPAL Technical Note 98-577.

[60] G. Parisi, Phys. Lett. **B74** (1978) 65;
J.F. Donoghue, F.E. Low and S.Y. Pi, Phys. Rev. **D20** (1979) 2759.

[61] The Particle Data Group, R.M. Barnett *et al.*, Phys. Rev. **D54** (1996) 159.

[62] R.D. Cousins and V.L. Highland, Nucl. Inst. and Meth. **A320** (1992) 331.

[63] P. Bock, *Determination of Exclusion Limits for Particle Production Using Different Decay Channels with Different Efficiencies, Mass Resolutions and Backgrounds*, OPAL Institute Publication 97-059, to be published in Nucl. Inst. and Meth.

[64] The OPAL Collaboration, G. Alexander *et al.*, Phys. Lett. **B370** (1996) 174.

[65] The ALEPH Collaboration, R. Barate *et al.*, Phys. Lett. **B418** (1998) 419.

[66] The ALEPH Collaboration, R. Barate *et al.*, *Search for charged Higgs Bosons in* e^+e^- *Collisions at* $\sqrt{s} = 181 - 184$ *GeV*, CERN-EP/99-011, to be published in Phys. Lett. B.

[67] The DELPHI Collaboration, P. Abreu *et al.*, Phys. Lett. **B420** (1998) 140.

[68] The L3 Collaboration, M. Acciarri *et al.*, Phys. Lett. **B** (1999) 368.

[69] The OPAL Collaboration, K. Ackerstaff *et al.*, *Measurement of the Michel Parameters in Leptonic Tau Decays*, CERN-EP/98-104, to be published in Eur. Phys. J. C.

[70] The ALEPH Collaboration, D. Buskulic *et al.*, Phys. Lett. **B343** (1995) 444.

[71] The CLEO Collaboration, M.S. Alam *et al.*, Phys. Rev. Lett. **74** (1995) 2885.

[72] The CDF Collaboration, F. Abe *et al.*, Phys. Rev. Lett. **79** (1997) 357.

[73] The D0 Collaboration, B. Abbott *et al.*, *Search for charged Higgs Bosons in decays of top quark pairs*, hep-ex/9902028, to be publihed in Phys. Rev. Lett.

[74] A. Djouadi, J. Kalinowski and P.M. Zerwas, Z. Phys. **C57** (1993) 569.

[75] F.M. Borzumati and A. Djouadi, ZU-TH 5/98, PM-98/1

[76] The OPAL Collaboration, K. Ackerstaff *et al.*, Phys. Lett. **B426** (1998) 180.

[77] The OPAL COllaboration, *Search for Charged Higgs Bosons in* e^+e^- *Collisions at* $\sqrt{s} = 189$ *GeV*, OPAL Physics Note 99-373.

[78] The OPAL Collaboration, G. Abbiendi *et al.*, *Search for Acoplanar Lepton Pair Events in* e^+e^- *Collisions at* $\sqrt{s}$ *= 161, 172 and 183 GeV*, CERN-EP/98-122, to be published in Eur. Phys. J. C.

[79] The ALEPH Collaboration, D. Buskulic *et al.*, Z. Phys. **C71** (1996) 179.

[80] B. Pietrzyk, *The ALEPH Four-Jet Story*, in *Proceedings of 33rd Rencontre de Moriond: QCD and High Energy Hadronic Interactions*, Les Arcs, 1997; LAPP-EXP-97.02.

[81] The OPAL Collaboration, G. Alexander *et al.*, Z. Phys. **C73** (1997) 201.

[82] The DELPHI Collaboration, P. Abreu *et al.*, Z. Phys. **C73** (1996) 1.

[83] The L3 Collaboration, M. Acciarri *et al.*, Phys. Lett. **B411** (1997) 330.

[84] The DELPHI Collaboration, P. Abreu *et al.*, Phys. Lett. **B448** (1999) 311.

[85] The LEP Working Group on Four Jets, M.A. Bizouard *et al.*, *Report of the LEP Working Group on Four-Jet Production in* e^+e^- *Collisons at Centre-of-Mass Energies of 130 − 172 GeV*, ALEPH 97-056 PHYSIC 97-050, DELPHI 97-57 PHYS 707, L3 Note 2090, OPAL Technical Note 97-486.

[86] V. Barger, W.-Y. Keung and R.J.N. Phillips, Phys. Lett. **B364** (1995) 27.

[87] D. Choudhury and D.P. Roy, Phys. Rev. **D54** (1996) 6797;
P. Chankowski, D. Choudhury and S. Pokorski, Phys. Lett. **B389** (1996) 677;
D.K. Ghosh and R.M. Godbole, Z. Phys. **C75** (1997) 357;
G.R. Farrar, *Phenomenology of Charginos and Neutralinos in the Light Gaugino Scenario*, RU-96-71, hep-ph/9608387;
G.R. Farrar, Phys. Rev. Lett **76** (1996) 4115;
A.K. Grant, R.D. Peccei, T. Veletto and K. Wang, Phys. Lett. **B379** (1996) 272;
S.F. King, Phys. Lett. **B381** (1996) 291;
H. Dreiner, S. Lola and P. Morawitz, Phys. Lett. **B389** (1996) 62.

[88] N.D. Hari Dass and V. Soni, *An Asymptotically Free Extension of QCD and ALEPH Four-jet Events*, hep-ph/9709391;
M. Carena, G.F. Giudice, S. Lola and C.E.M. Wagner, Phys. Lett. **B395** (1997) 225.

[89] The OPAL Collaboration, K. Ackerstaff *et al.*, Phys. Lett. **B429** (1998) 399.

[90] The ALEPH Collaboration, D. Buskulic *et al.*, Phys. Lett. **B420** (1998) 196.

[91] G. Bhattacharyya, *R-parity Violating Supersymmetric Yukawa Couplings: a mini-Review*, Nucl. Phys. Proc. Suppl. **A52** (1997) 83;
S. Dimopoulus and L.J. Hall, Phys. Lett. **B207** (1987) 210;
V. Barger, G.F. Giudice and T. Han, Phys. Rev. **D40** (1989) 2987;
K. Agashe and M. Graesser, Phys. Rev. **D54** (1996) 4445;
R.M. Godbole, P. Roy and T. Tata, Nucl. Phys. **B401** (1993) 67;
G. Bhattacharyya, J. Ellis and K. Sridhar, Mod. Phys. Lett. **A10** (1995) 1583;
R.N. Mohapatra, Phys. Rev. **D34** (1986) 3457;
M. Hirsh *et al.*, Phys. Rev. Lett. **75** (1995) 17;
J.L. Goity and M. Sher, Phys. Lett. **B346** (1995) 69.

[92] I. Hinchliffe, T. Kaeding, Phys. Rev. **D47** (1993) 279.

[93] A.Y. Smirnow, F. Vissani, Phys. Lett. **B380** (1996) 317.

[94] The OPAL Collaboration, K. Ackerstaff *et al.*, Euro. Phys. J. **C6** (1998) 1.

[95] The OPAL Collaboration, K. Ackerstaff *et al.*, *Search for Chargino and Neutralino Production at* $\sqrt{s}$ *= 181 − 184 GeV at LEP*, CERN-EP/98-136, to be published in Euro. Phys. J. C;
The OPAL Collaboration, K. Ackerstaff *et al.*, Phys. Lett. **B433** (1998) 195.

[96] The ALEPH Collaboration, R. Barate *et al.*, Eur. Phys. J. **C4** (1998) 433;
The ALEPH Collaboration, R. Barate *et al.*, Eur. Phys. J. **C7** (1999) 383.

[97] The L3 Collaboration, M. Acciari *et al.*, *Search for R-parity Violating Chargino and Neutralino Decays in e^+ and e^- Collisions up to $\sqrt{s}$ = 183 GeV*, CERN-EP/99-023, to be published in Phys. Lett. B

[98] The OPAL Collaboration , G. Abbiendi *et al.*, *Searches for R-Parity Violating Decays of Gauginos at 183 GeV at LEP*, CERN-EP/98-203, to be published in Eur. Phys. J. C.

[99] The OPAL Collaboration , G. Abbiendi *et al.*, *Searches for R-Parity Violating Decays of Scalar Fermions at LEP*, CERN-EP/99-xxx, to be published in Eur. Phys. J. C.

[100] S. Dawson, Nucl. Phys. **B261** (1985) 297;
V. Barger, W.-Y. Keung and R.J.N. Phillips, Phys. Lett. **B364** (1995) 27, Erratum-ibid **B377** (1996) 486;
M. Carena *et al.*, Phys. Lett. **B395** (1997) 225.

[101] The Particle Data Group, R.M. Barnett *et al.*, Phys. Rev. **D54** (1996) 694.

[102] The OPAL Collaboration, K. Ackerstaff *et al.*, Euro. Phys. J. **C4** (1998) 47.

[103] E. Accomando *et al.*, in *Physics at LEP2*, CERN 96-02, Vol.2, p. 299.

[104] The OPAL Collaboration, K. Ackerstaff *et al.*, Z. Phys. **C75** (1997) 409.

[105] The OPAL Collaboration, G. Abbiendi *et al.*, *Search for Scalar Top and Scalar Bottom Quarks at E_{CM} = 189 GeV at LEP*, CERN-EP/99-036, to be published in Phys. Lett B.

[106] S.L. Meyer, *Data Analysis for Scientists and Engineers*, John Wiley and Sons, 1975.

[107] The Particle Data Group, R.M. Barnett *et al.*, Phys. Rev. **D54** (1996) 214.